



UNIVERSITÀ  
DEGLI STUDI  
FIRENZE

Doctoral Programme in Industrial  
Engineering  
Dottorato di Ricerca in Ingegneria  
Industriale

XXXII

**Reverse Engineering in Medical  
Applications:  
a new hybrid approach for automatic 3D  
reconstruction of defective neurocrania**

ING/IND-15

**Doctoral Candidate**

Antonio Marzola

**Supervisor**

Prof. Lapo Governi

**External Referees**

Prof. Luca Di Angelo

**Dean of the Doctoral Programme**

Prof. Maurizio De Lucia

Prof. Alessandro Naddeo

Years 2016/2019



© Università degli Studi di Firenze – School of Engineering  
Via di Santa Marta, 3, 50139 Firenze, Italy

Tutti i diritti riservati. Nessuna parte del testo può essere riprodotta o trasmessa in qualsiasi forma o con qualsiasi mezzo, elettronico o meccanico, incluso le fotocopie, la trasmissione fac simile, la registrazione, il riadattamento o l'uso di qualsiasi sistema di immagazzinamento e recupero di informazioni, senza il permesso scritto dell'editore.

All rights reserved. No part of the publication may be reproduced in any form by print, photoprint, microfilm, electronic or any other means without written permission from the publisher.







# Summary

Reverse Engineering (RE) and Additive Manufacturing (AM) are penetrating the healthcare field at an astonishing rate and continue to push the boundaries of cost-efficiency, convenience, and customization in medical applications. Despite their potential, there is still a long way to overcome the technical and ethical difficulties of these emerging technologies so that they can be considered as standard techniques. One of the most important technical issues is the lack of a proper and reliable procedure for the geometric reconstruction of an anatomical region of interest (ROI) from diagnostic images. The anatomical ROI can be processed and reconstructed with advanced RE-based techniques starting from standard diagnostic imaging such as Computed Tomography (CT) and Magnetic Resonance Imaging (MRI). Nowadays, many RE software packages offer several tools, for instance, to fill holes or repair a polygonal model, in case the ROI is partly missing or damaged. Often, however, these tools turn out to be inadequate, mainly when the defect is large or when a defective physical region needs to be retrieved consistently with the surrounding anatomy. Therefore, the reconstruction of the damaged ROI requires time consuming and complicated manual operations to achieve a suitable outcome. These limitations are particularly relevant in those applications where aesthetics represents a critical factor, as in maxillo-facial surgery and neurosurgery.

Namely in cranioplasty surgery (i.e. a neurosurgical technique to repair cranial defects by insertion of a prosthesis), achieving an effective aesthetic shape restoration of the cranial vault is the most important issue to ensure a proper surgical outcome. Cranial defects are typically due to trauma, congenital dysmorphisms, or complications of a previous surgery. A good restoration of the cranial integrity is fundamental for the functionality and protection of the brain, but mainly it is fundamental for aesthetics: an incorrect reconstruction of the cranial shape, as far as it can be considered acceptable in terms of functionality, can lead to significant social and emotional implications on the patient and his relatives that cannot be underestimated, especially in pediatrics. For this reason, the cranial implant must have both an aesthetically coherent shape with respect to the healthy bone and a precise fit with the outer surface of the skull. These aspects are crucial for a successful intervention.

To date, the most advanced approach uses CT/MRI data to reconstruct the 3D anatomy of the defective skull in order to design, in a pre-operative stage, a patient-specific prosthesis. In the last years, several techniques have been proposed to improve the applicability of such approach in the clinical practice. The state-of-the-art analysis, carried out throughout the doctorate, shows three different strategies for the defective skull reconstruction: Template-based, Surface Interpolation-based and Slice-based. The analysis of the related literature, however, also shows that each of these strategies has still open issues, due to the complexities imposed by the surface that needs to be retrieved (i.e. the human anatomy).

With the aim to overcome the state-of-the-art drawbacks, the thesis proposes a new semi-automatic *hybrid* procedure for repairing cranial defects. The presented approach is in fact a *hybrid* one since a surface interpolation is used for filling the hole but, to ensure a consistent reconstruction, the interpolation is driven by a template, able to compensate for the lack of information in the deformed or missing areas. The template ability to encode the knowledge of a consistent cranial shape is exploited to improve the quality and the accuracy of the reconstruction; at the same time, the repeatability is ensured by an automatic reconstruction provided by the surface interpolation.

In this thesis, the template is defined by means of Statistical Shape Analysis, able to provide a pathologically unaffected parametric model of the neurocranium or, when the defect is unilateral, by means of a mirroring technique exploiting the healthy half of the neurocranium.

The procedure, being landmark-independent and avoiding any patch adaptation, represents a valid alternative to the existing approaches also in terms of user's burden, requiring less time consuming and less cumbersome operations.

Several test cases have been addressed to prove the effectiveness and repeatability of the proposed procedure in reconstructing large-size defects of the human neurocranium.

In addition, a new evaluating technique able to measure the symmetry of the restored skull as well as the continuity between the reconstructed patch and healthy bone is proposed to test the procedure performance.



# Table of contents

<b>Summary .....</b>	<b>7</b>
<b>Table of contents.....</b>	<b>9</b>
<b>List of figures .....</b>	<b>11</b>
<b>List of tables.....</b>	<b>15</b>
<b>Acronyms List.....</b>	<b>17</b>
<b>Introduction .....</b>	<b>19</b>
<b>1. Thesis structure and goals.....</b>	<b>23</b>
<b>2. State-of-the-Art analysis.....</b>	<b>25</b>
2.1. Template-Based Techniques .....	26
2.1.1. Mirroring.....	28
2.2. Surface Interpolation-based Techniques .....	29
2.3. Slice-based Techniques .....	30
2.4. Open Issues .....	32
<b>3. The proposed <i>hybrid</i> approach for the reconstruction of a human neurocranium...35</b>	
3.1. Methods and Tools .....	36
3.1.1. Shape.....	36
3.1.2. Data Representation .....	37
3.1.3. Template Definition .....	38
3.2. Algorithm implementation .....	39
3.2.1. Model pre-processing.....	39
3.2.2. Identification of the hole .....	40
3.2.3. <i>Missing Points</i> Definition .....	41

3.2.4. Definition of the Interpolation Centers.....	43
3.2.5. Surface Interpolation .....	45
3.2.6. Transformation of the Data .....	46
3.2.7. Patch Tessellation and Merging with the Defective Cranial Vault.....	46
<b>4. Methods and Tools .....</b>	<b>47</b>
4.1. Statistical Shape Analysis.....	47
4.1.1. <i>Statistical Shape Modelling</i> : a reliable and robust procedure for neurocrania 51	
4.1.2. Posterior Shape Models.....	59
4.1.3. Assessment of the proposed procedure for the SSM construction .....	62
4.2. Unilateral Defects: a robust and automatic method for the best <i>symmetry plane</i> detection of the craniofacial skeletons.....	68
4.2.1. Related work .....	69
4.2.2. The Mirroring and Weighted Approach .....	73
4.2.3. Evaluation of the proposed procedure for the <i>symmetry plane</i> detection.....	76
<b>5. Results .....</b>	<b>83</b>
5.1. New Evaluation criteria .....	83
5.2. Estimate of input parameters .....	85
5.3. Evaluation of the proposed algorithm.....	90
5.3.1. Unilateral Defects.....	91
5.3.2. Non-Unilateral Defects.....	93
5.3.3. Comparison of results with commercial software .....	98
<b>6. Conclusions and final remarks .....</b>	<b>101</b>
<b>Bibliography .....</b>	<b>105</b>

# List of figures

Figure 1.1: Typical Medical Device (MD) CAx Framework .....	20
Figure 1.2: a) CT slice; b) histogram of the grey level in the CT slice; c) segmentation .....	21
Figure 1.3: a) three typical causes for cranial defects. b) the correspondent cranial plate .....	22
Figure 2.1: Anatomical Landmarks used in [20] .....	27
Figure 2.2: An example of the Mirroring approach: (a) the starting defective skull; (b) the reflection of the non-defective side; (c) the reconstructed patch.....	29
Figure 2.3: (a) the defective part reconstructed by surface interpolation can lead to a too flat patch; (b) the comparison between the patch obtained with the surface reconstruction technique and using the mirroring technique (in transparency). .....	30
Figure 2.4: A slice in a TC of a defective skull (a) and the resulting boundary (dotted line) fitted on the bone surface, obtained by ACM starting from a coarse approximation (solid line). .....	32
Figure 3.1: The proposed <i>hybrid</i> procedure .....	36
Figure 3.2: a) the neurocranial 3D model as exported after the segmentation; b) the exocranial surface after the pre-processing.....	40
Figure 3.3: The ray-tracing algorithm to select the external surface (in grey). a) Each ray originates from the centroid $O$ and intersects the surface of the model; b) only the outermost face is selected.....	40
Figure 3.4: Automatic edge detection ( <i>free edges</i> and <i>BPs</i> are reported in green).....	41
Figure 3.5: a) for unilateral defect the healthy half is used as template and b) mirrored onto the defective one .....	42
Figure 3.6: for a non-unilateral defect (a) an external template (b) representing the unaffected ROI is used to match the defective model and retrieve the missing information (c)...	42
Figure 3.7: the <i>MPs</i> and the <i>BPs</i> .....	43
Figure 3.8: The Interpolation centers set: (a) lateral view, (b) frontal view. ....	44
Figure 3.9: a) Surface interpolation; b) Surface delimitation using the boundary loop (in blue); c) the final STL merged model .....	46

Figure 4.1: Example of correspondence failure: the mismatching between external and internal surface of the skull.....	50
Figure 4.2: a – b) The selection of Left Orbital (yellow) and both the Porions (green and red) landmarks; c) The isolated neurocranium; d) The Frankfurt Plane passing through the three landmarks .....	51
Figure 4.3: The flow chart of the proposed procedure to build the SSM.....	52
Figure 4.4: The initial alignment .....	53
Figure 4.5: The coordinate frame of the pre-aligned Training Set. The centroid of each model is superimposed to the origin of the axes. The red dotted line represents the Bounding Box of the sample. The dimension a, b and c are defined as reported.....	53
Figure 4.6: a – c) Three subsequent steps of the non-rigid registration between the Reference (deformable, in blue) and the Target (fixed, in grey); d) color maps of the mesh deviation between the Target and the resulting template.....	54
Figure 4.7: Correspondence checking.....	55
Figure 4.8: The first MoV.....	57
Figure 4.9: The second MoV .....	58
Figure 4.10: The third MoV.....	58
Figure 4.11: The prior model (a) constraints the possible shapes of the posterior model (b) .....	59
Figure 4.12: Deviation (in mm) between the deformed Reference $\Gamma_{R_i}$ and the Target $\Gamma_i$ ....	63
Figure 4.13: <i>Generalization ability</i> .....	66
Figure 4.14: <i>Specificity</i> .....	66
Figure 4.15: <i>Compactness</i> .....	66
Figure 4.16: The comparison between the <i>Generalization ability</i> of the ICP-based model (square) and the CPD-based model (circle).....	67
Figure 4.17: The comparison between the <i>Specificity</i> of the ICP-based model (square) and the CPD-based model (circle) .....	67
Figure 4.18: The comparison between the <i>Compactness</i> of the ICP-based model (square) and the CPD-based model (circle).....	67
Figure 4.19: a) Landmarks localization; b) MSP definitions according to methods proposed in [109] and c) [110].....	70
Figure 4.20: a) Landmarks and MSP definitions according to methods proposed in b) [105] .....	72
Figure 4.21: MSP resulting by methods proposed in [114] for (a) complete and (b) defective skull .....	73
Figure 4.22: The flow chart of the <i>MaWR</i> methods as presented in [34].....	74

Figure 4.23: The MPS resulting from: a) the <i>MaWR</i> method as presented in [34]; b) the <i>MaWR</i> improved method .....	76
Figure 4.24: The first 5 test cases. a) TC#1; b) TC#2; c) TC#3; d) TC#4; e) TC#5 .....	78
Figure 4.25: The AV maps for the TC#5 and the four methods here compared.....	79
Figure 4.26: Skull with craniofacial dysmorphism due to hypertelorism combined with a severe form of plagiocephaly. a) MSP resulting from the proposed method; b) MSP resulting from the proposed method applied to the user selected area highlighted in green.....	80
Figure 5.1: Test Case #1_C – a) The defective model; b) The Posterior model; c) Deviation map between a) and b); d) The reconstruction provided by the proposed algorithm; e) Deviation map between d) and a).....	95
Figure 5.2: Test Case #2_C – a) The defective model; b) The Posterior model; c) Deviation map between a) and b); d) The reconstruction provided by the proposed algorithm; e) Deviation map between d) and a).....	96
Figure 5.3.: Test Case #5 – a) The defective model; b) The Posterior model; c) Deviation map between a) and b); d) The reconstruction provided by the proposed algorithm; e) Deviation map between d) and a).....	97
Figure 5.4: TC#1_A – The comparison between the complete symmetric synthetic skull and the reconstructed carried out by (a) the proposed method and (b) the hole-filling tool provided by using Geomagic® Design X.....	99
Figure 5.5: TC#1_B – The comparison between the complete symmetric synthetic skull and the reconstructed carried out by (a) the proposed method and (b) the hole-filling tool provided by using Geomagic® Design X.....	99



## List of tables

Table 2.1: Comparison of advantages and disadvantages of different Skull Virtual Reconstruction strategies.....	33
Table 4.1: Landmarks definition .....	71
Table 4.2: The Asymmetry Value for the twenty test cases and four methods analyzed .....	79
Table 5.1: The combinations of parameters $n$ and $m$ in each of the test case addressed .....	85
Table 5.2: The reconstructed surface by varying the interpolation centers. The outer rim are the n-RNs and the BPs while the inner points are the MPs. a) $n=10$ and $m=10$ ; b) $n=10$ and $m=80$ ; c) $n=10$ and $m=10$ ; d) $n=40$ and $m=10$ .....	86
Table 5.3: The four test cases discussed in detail.....	87
Table 5.4: The resulting $AV$ and $AV_{point}$ for TC#1 .....	88
Table 5.5: The resulting $AV$ and $AV_{point}$ for TC#2 .....	88
Table 5.6: The resulting $AV$ and $AV_{point}$ for TC#3 .....	89
Table 5.7: The resulting $AV$ and $AV_{point}$ for TC#4 .....	89
Table 5.8: Starting models for the discussed test cases .....	90
Table 5.9: Unilateral or quasi-unilateral defects: algorithm outcomes.....	91
Table 5.10: $AV$ values for all the unilateral and quasi-unilateral test cases discussed.....	92
Table 5.11: $AV_{point}$ maps for the unilateral and quasi-unilateral test cases discussed.....	92
Table 5.12: $AV$ values for all the unilateral test cases discussed .....	94
Table 5.13: $AV_{point}$ maps for the non-unilateral test cases discussed.....	98





# Acronyms List

3D	Three Dimensional
ACM	Active Contour Model
AM	Additive Manufacture
ANS	Anterior Nasal Spine (anatomical landmark)
Ba	Basion (anatomical landmark)
BPs	Boundary Points
CAx	Computer-Aided Technologies
CG	Crista Galli (anatomical landmark)
CPD	Coherent Point Drift
CPD	Coherent Drift Points
CT	Computed Tomography
DICOM	Digital Imaging and Communications in Medicine
FNM	Frontonasomaxillare (anatomical landmark)
FOM	Frontorbitomaxillare (anatomical landmark)
FP	Frankfurt Plane
FZS	Frontozygomatic Suture (anatomical landmark)
GPA	Generalized Procrustes Analysis
GPMM	Gaussian Process Morphable Model
ICP	Iterative Closest Point
IF	Incisive Foramen (anatomical landmark)
MAD	Mean Averaged Distance
MD	Medical Device
ML	Maximum Likelihood
MOV	Mode of Variation
MPs	Missing Points
MRI	Magnetic Resonance Imaging
MSP	Mid-Sagittal Plane
N	Nasion (anatomical landmark)

n-RNs	n-Ring Neighbors Points
OPA	Ordinary Procrustes Analysis
PA	Procrustes Analysis
PDM	Point Distribution Model
Pog	Pogonion (anatomical landmark)
PSM	Posterior Shape Model
PSO	Particle Swarm Optimization
RBF	Radial Basis Function
RE	Reverse Engineering
ROI	Region of Interest
S	Sella (anatomical landmark)
SM	Symmetric Mean
SoA	State-of-the-Art
SOF	Supraorbital Foramen (anatomical landmark)
SSA	Statistical Shape Analysis
SSM	Statistical Shape Model
STL	Standard Triangulation Language
TPS	Thin Plate Spline
TS	Training Set

# Introduction

In the last few years, the astonishing evolution of Computer-Aided Technologies (CAx) has made possible to process and analyze complex geometries, even if they cannot be represented by mathematical functions. The straightforward strategy to digitalize such complex geometries is to extract the shape information directly from physical object without using drawings or documentation but exploiting a set of proper measurements taken on the object to be reproduced. The process of digital duplicating an existing part and the subsequent post-processing to provide a model suitable for use with CAx software is known as Reverse Engineering (RE). The RE approaches are widespread in engineering for many applications, but notwithstanding the concept of RE was primarily developed for manufacturing industry applications, its applicability has been extending in non-traditional fields, as biology and anatomy. Especially in the field of medicine, the increasing ability to face with non-mathematical surfaces is representing a breakthrough for clinical practice, both in terms of effectiveness and costs [1 – 4\_ADM], enabling a new highly customized approach in surgery in those applications where commercial devices are not suitable. By exploiting typical RE techniques, it is possible to digitalize and process the three-dimensional (3D) anatomical region of interest (ROI) directly from the patient's own diagnostic images obtained by Computerized Tomography (CT) or Magnetic Resonance Imaging (MRI).

Figure 1.1 describes the typical workflow followed to obtain a customized Medical Device (MD) from the diagnostic images. CT and MRI enable the in-vivo extraction of high-resolution patient-specific anatomic information provided as a series of stacked two-dimensional (2D) cross-sectional images (named “slices”) of an anatomical region. The extracted information is delivered in a standard file format named DICOM (Digital Imaging and Communications in Medicine). By means of a digital post-processing, DICOM data can be used to generate a three-dimensional (3D) model of the anatomical Region of Interest (ROI) both for soft and hard tissues.

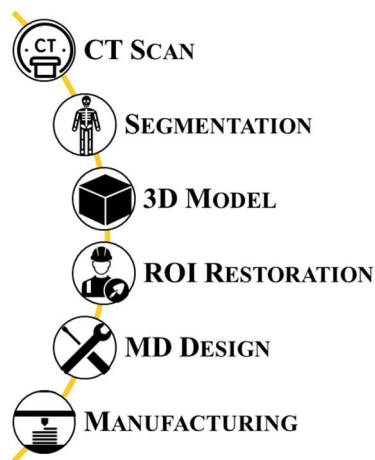
In the application presented in this thesis, the ROI is represented by the defective or deformed neurocranium. Dealing with hard tissues, the CT images are particularly suitable because bones appear with a well-identifiable greyscale intensity window. So, a simply gray-value thresholding with an easily recognizable lower and upper bound can be applied to filtering out the surrounding tissues from the ROI by generating a binary mask partitioning the images into the meaningful segment and the background (Figure 1.2).

To date, many commercial software packages (e.g. Materialise Mimics® or 3DSlicer®) provide internal tools for such a segmentation as well as for the subsequent creation of the correspondent 3D discrete scalar field, known as *voxel*-based model. In order to provide a more easily manipulatable 3D model, the software enables to export this *voxel*-based model in a

Standard Triangulation Language (STL) format. The STL format is supported by many software packages and is widely used in Reverse Engineering applications and in Additive Manufacturing (AM).

CAX software packages provide advanced tools to properly handle the so obtained 3D model allowing more effective pre-operative simulation, complex-surgery planning, quantitative evaluation of asymmetry or dysmorphism and the design of the patient-specific devices or instrumentations.

This highly customized approach has proved to be really effective in the clinical practice, especially considering the possibility of manufacturing any complex geometry directly from the designed digital model by means of AM technologies [5]. Advances in AM technologies enable the direct production of implants without the constraints of shape and size, but ensuring the proper mechanical properties: consequently, AM technologies make the fabrication of the actual implants that conform to the physical and mechanical requirements possible, but they can be also used to build the 3D physical reproductions of the ROI to obtain further diagnostic insights or to simulate surgery. Furthermore, the physical reproductions of the ROI are finding great applicability in the education of young surgeons and to improve communication between surgeons and patients.



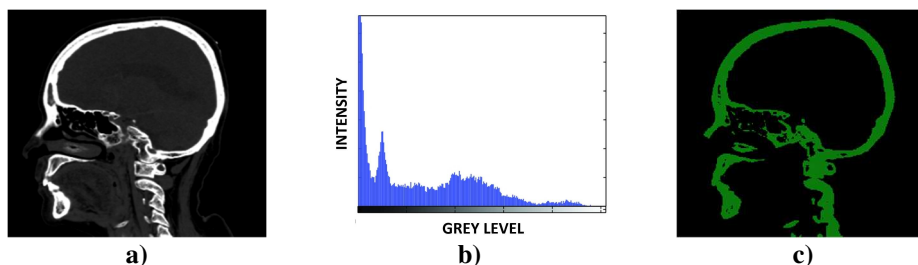
**Figure 1.1: Typical Medical Device (MD) CAX Framework**

Considering the typical workflow depicted in Figure 1.1, the interest of this thesis principally lies in the study of ROI restoration step in the specific case of a defective or deformed neurocranium.

Cranial defects are typically due to trauma, tumors resections, congenital dysmorphisms, or complications of a previous surgery (Figure 1.3(a)). The defects are normally corrected by the insertion of a prosthesis capable of restoring a consistent shape to the resulting skull (Figure 1.3(b)). The prosthesis can be an original skull piece or a custom contoured graft. The surgical technique to restore the cranium by using a prosthesis is named Cranioplasty. A Cranioplasty might be performed to protect the brain, to restore normal neurological function and for aesthetics since a noticeable skull defect can affect patient's appearance and confidence. Face is the most important mean of communication and social interaction [6] and an incorrect reconstruction of the cranial shape can lead to potential

significant social and emotional implications on the patients and their relatives that cannot be underestimated, especially in pediatrics [7 – 9].

For these reasons and to ensure a more satisfactory outcome, the xenograft or autograft implants usually molded at the time of surgery by the surgeon, are being replaced by devices built pre-operatively on the patient-specific (virtual or physical) anatomical reproduction [10] exploiting RE techniques as explained above. This approach has brought to less intra-operative implant's adaptation need, with many advantages regarding the reduction of surgical time and the improvement of the clinical outcomes [8, 11, 12].



**Figure 1.2:** a) CT slice; b) histogram of the grey level in the CT slice; c) segmentation

It is worth to note that, since a cranial implant does not usually perform a critical structural function other than protecting the brain, the success of the operation resides in a reconstruction of the anatomy, aimed at restoring a satisfactory aesthetics. As a consequence, the ROI reconstruction results to be the most influencing for the achievement of a satisfying surgical outcome. At the same time, this task is undoubtedly the most complex, cumbersome and time-consuming for the user: the ROI often have malformations or missing parts, and there is no information available to guide an adequate restoration, mainly due to the wide variability and high complexity of the human anatomy. The need to obtain an accurate reconstruction and the complexity of the task have led to an extensive literature published in this regard. A thorough analysis of the SOA has in fact revealed a wide range of alternatives proposed to achieve a cranial vault reconstruction which is consistent and, at the same time, as fast and simple as possible [13]. Such techniques can be grouped in three different reconstructive approaches, depending on the strategy used for reconstruction: (i) the *Template-based* approach uses prior knowledge provided by a template which contains information on the expected shape for a data-guided reconstruction of the cranial bone to be restored, (ii) the *Surface-based* approach uses a mathematical surface that interpolates the edge of the defect and (iii) *Slice-based* approach which deform a mathematical curve to wrap the contour of the healthy bone slice-by-slice. To ensure a consistent result, all the studies proposed in literature deal with (i) how to find the missing information to achieve a resulting skull as symmetrical as possible and (ii) how to ensure the continuity between the reconstructed patch and the surrounding healthy bone. Furthermore, there is now a great interest in automating the whole framework presented in Figure 1.1, with the aim of (i) speeding it up, because time between the diagnosis and the surgical intervention could be critical in some applications (as in oncology), (ii) making the instruments available also to less experienced CAx users or directly to surgeons, and (iii) eliminating all time-consuming, repetitive and cumbersome user operations. Moreover, by using an automatic procedure, it is possible to maximize the repeatability of the reconstruction.

A comprehensive description of the most representative existing approaches with their strengths and limitations is presented in Chapter 2. The SoA analysis has shown that, up to date, a convincing solution has not been yet proposed: all the proposed approaches share weaknesses and limits that mainly are represented either by a high user interaction request or the lack of data within the hole that could compromise an aesthetically acceptable reconstruction. In order to overcome these drawbacks, a new *hybrid* procedure is proposed in this thesis. The aim of the procedure is the semi-automatic restoration of the outer surface for a defective or deformed neurocranium, able to ensure an adequate symmetry of the resulting skull and the continuity between the bone and the reconstructive patch. The presented approach is *hybrid* since a *Surface Interpolation-based* approach is used for filling the hole but, to ensure a consistent reconstruction, the interpolation is driven by a template able to compensate for the lack of information in the deformed or missing areas. This way, the template ability in encoding the knowledge of a consistent cranial shape is exploited in addition of the repeatability ensured by an automatic reconstruction provided by the surface interpolation to improve the quality and the accuracy of the reconstruction.

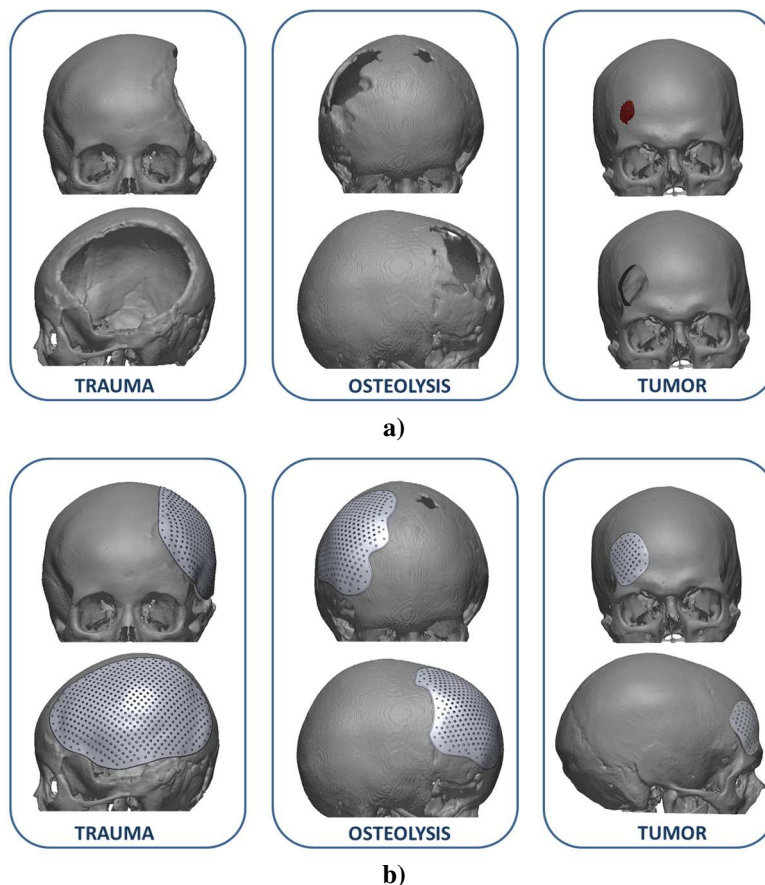


Figure 1.3: a) three typical causes for cranial defects. b) the correspondent cranial plate

# 1. Thesis structure and goals

The Thesis intends to investigate the new personalized approach to healthcare, which is representing a breakthrough in the medical and surgical field; in particular, the aim is the development of new automatic tools based on Reverse Engineering techniques to improve the applicability of patient-specific (PS) treatments and devices. The specific goal of this study is to propose a new procedure for the reconstruction of a defective or deformed anatomy, specifically tailored for human neurocrania. Since in Cranioplasty the surgical outcome is mainly related to aesthetics, the possibility to preoperatively build a cranial prosthesis able to restore the missing region in a consistent way represents a step forward with respect to a xenograft or autograft implants molded at the time of surgery by the surgeon.

The greatest challenge for the preoperative design is represented by the lack of knowledge able to guide the reconstruction towards a consistent shape, due to the high complexity of the geometry and the wide interpersonal variability. Namely for the neurocranium, several techniques have been proposed in literature to retrieve the necessary information for a proper reconstruction. Despite of that, there is still no robust procedure capable of ensuring a result that is consistent in terms of both symmetry of the resulting skull and continuity between the reconstructed patch and the surrounding healthy bone. This thesis starts from the strengths and the limitations of the SoA approaches to devise a new *hybrid* procedure for the reconstruction of a defective or deformed cranial vault. The proposed procedure is defined *hybrid* because it has basically a *Surface Interpolation-based* approach, but it exploits the knowledge encoded in a template to enable a data-driven reconstruction within the defect. This *hybrid* approach allows for continuity at the boundary of the defect with an easily automatable procedure, ensured by applying a surface interpolation, but, at the same time, it allows to ensure the consistency of the reconstructed shape by adding the information encoded in the template.

The thesis also aims to define a new method for evaluating the results of the reconstruction task. In the related literature, the main criterion for evaluating a reconstructive patch is how closely it matches the original surface. For this purpose, usually the test cases addressed are represented by a complete skull with artificial holes [14] since the original surface of a real defective skull is rarely known. Notwithstanding, in the author's view such comparison does not represent a good criterion for assessing the reconstruction outcome. At first analysis, it is not applicable in the normal clinical practice as the original surface is commonly unknown. More importantly, it does not consider the actual aesthetical outcome, which is the most relevant aspect in the cranial vault shape restoration [8, 9, 15].

The thesis is organized as follows: Chapter 2 reports the SoA of the existing approaches for the virtual reconstruction of a defective cranial vault. The strengths and the limitations of each existing strategy are discussed in this section.

Chapter 3 presents a comprehensive description of the new proposed *hybrid* methodology.

Chapter 4 provides an exhaustive description of methods and tools used for the implementation of the presented methodology.

Chapter 5 analyses the results obtained applying the reconstruction tool to multiple case studies; to this purpose, both synthetic and real neurocrania have been considered. The new evaluating methodology is presented in this chapter.

Chapter 6 presents some concluding considerations and possible improvements that may be addressed in the future.



## 2. State-of-the-Art analysis

The ability to achieve a consistent reconstruction of a missing or deformed anatomical area is a fundamental step for defining a customized implant, especially in the maxillofacial and cranial reconstruction where the aesthetical side are essential for an adequate surgery outcome. At the same time, this task is undoubtedly the most complex, cumbersome and time-consuming across the whole reconstruction procedure, mainly because of the great geometric complexity and the lack of certain references due to the wide interindividual anatomical variability.

Namely for the neurocranium, a wide range of alternatives has been proposed in scientific literature to effectively face the reconstruction problem. All of the approaches aim to propose a robust procedure able to *(i)* provide a reliable reconstruction considering both functional and aesthetical aims, *(ii)* make tools available also to less experienced CAx users or directly to surgeons, and *(iii)* eliminate all time-consuming, repetitive and cumbersome user operations.

Alternative approaches differ for the data sources used and for the tools exploited to perform the reconstruction; despite that, they could however be framed in the typical workflow followed for the computer-aided design of any customized medical device (Figure 1.1). Typically, the input data is the patient's own diagnostic images to obtain a digital anatomic model on which actually design the customized device.

This chapter provides a brief description of the most representative approaches identified during the SoA analysis performed with reference to the virtual reconstruction of a defective or deformed neurocranium. The selected approaches have been grouped into the following three main categories, depending on the adopted reconstruction strategy:

- *Template-based* Techniques: they adopt an a-priori generated three-dimensional template encoding knowledge of the undefective shape of the missing region to be reconstructed. A widely used *Template-based* technique in restoring unilateral defect (i.e. defects that do not cross the sagittal plane) is the *Mirroring* technique, which uses the healthy half of the cranial vault mirrored onto the defective one as a template.
- *Surface Interpolation-based* Techniques: they pursue the reconstruction of the missing area by fitting a mathematical function which smoothly interpolates across the hole.
- *Slice-based* Techniques: they use 2D diagnostic CT/MRI images to fit a mathematical closed curve to the bone contour in a slice-by-slice approach.

In order to present an organized description of the state of the art, the following sections adhere to this categorization.

It is important to note that most of the presented methods, due to the highly complex structure of human skull, are only meant to be used for the reconstruction of the cranium vault.

## 2.1. Template-Based Techniques

This class of methods makes use of an a-priori generated 3D template of the human skull to model the missing cranial area. Typically, the template is extracted from a database of 3D skull models using statistical tools (e.g. Statistical Shape Analysis [16, 17, 18]), cephalometric analysis [19] or by reflecting the non-defective side of the skull onto the defective one (in case of unilateral defects); the goal is to retrieve a reference shape for the missing area to be used to guide the reconstruction on the region of interest. The adaptation of the template upon the defective skull is typically guided by suitable landmarks, which map the two models. Several strategies, which differ in the algorithms and mathematical tools used for the adaptation as well as in the level of user interaction required, can be identified.

Marreiros et al. [20] propose an approach based on geometric morphometrics to guide a surface interpolation that is performed using RBFs. For unilateral defects, the healthy symmetrical surface can be used as a template. Alternatively, a database-extracted template is required. Their approach is specifically tailored for the reconstruction of large defects (i.e.  $>100 \text{ cm}^2$ ). The process starts with a manual segmentation of the original CT data, performed to isolate the cranial bone as well as to remove artifacts and small bone regions. Subsequently, anatomical landmarks need to be placed upon the defective skull. Seventeen standard landmarks (see Figure 2.1) are manually identified; starting from this initial set, additional landmarks are mapped on the cranial surface using a ray-casting approach [21]. Symmetry and/or template geometries are used for the generation of landmarks in the defective region, by means of a Thin-Plate Spline (TPS) relaxation process. Obtained landmarks are interpolated by 2D RBFs, allowing “the construction of a depth map centered at the (manually selected) missing landmarks of the defective skull”. The generated surface is then used to create a mesh that closely fits the defect boundary.

The method presents two principal limitations: the defect area needs to be properly covered by an appropriate number of landmarks, and it needs to be described by a well-defined perimeter in order to avoid leaking effects. Moreover, the deformation process proves to be computationally expensive.

A similar approach is presented by Dean et al. in [22, 23]; the authors make use of a TPS-warp algorithm to map a template skull surface image upon the defective one. The process starts with a semi-automatic identification, based on manually selected landmarks, of the defect margins. A set of globally located skull landmarks, identified on both the defective skull and the template, are used to guide a first-pass warp operation that adapts the template onto the defective cranium. An additional set of landmarks, located in the defect area, is automatically generated via ray-casting and used to guide a second warp operation, thereby improving the result. In order to avoid the flattening of the patch, additional landmarks, extracted from the template, are added inside the defect area.

An alternative approach, with respect to TPS-based ones, is presented by Wu et al. in [24]. The authors propose an anatomical-constrained deformation process based on radial scaling. Both mirroring and a 3D retrieval approach, performed using a database of skull models, are considered as possible sources for the reference template model used to guide the reconstruction. The paired point matching method is then used to guide the binding of

corresponding landmarks between the defective and reference models. Alternatively, a user-guided approach could be adopted. The actual deformation is performed adaptively at each point: using known radial distances of corresponding landmarks, the authors compute local scaling factors. Finally, scaling factors of the defect area points are estimated via interpolation and used to compute the missing surface.

A significant attempt towards the automatization of the reconstruction process is proposed by Fuessinger et al. in [14]. In particular, a Statistical Shape Model (SSM), able to minimize the manual interaction required by a surgeon for the creation of cranial implants, is proposed. The method is based on a manual approach to attain the identification of the defective area and to place anatomical landmarks on the patient skull. These are used to map the skull to a database of 131 CT scans of healthy crania. Using the anatomical landmarks (i.e. landmarks located in salient anatomical feature points) correspondences, the target surface is aligned to the mean shape of the SSM; an iterative closest point (ICP) algorithm is used to refine the alignment. A new SSM, evaluated on a subset of skull shapes characterized by minimal deviation w.r.t. the patient skull, is then generated. The SSM is subsequently refined using an elastic ICP based on smoothed displacement fields. The final model is obtained by fitting the SSM to the target model using a TPS deformation guided by additional landmarks not necessarily located at salient feature points.

Overall, the studies presented in this section provide evidence that template-based approaches are the most suitable for the reconstruction of large holes in the skull and represent a valid strategy to tackle all kinds of defects. By adopting this strategy, a possible notable lack of information in the patient CT data is well-compensated by external sources. On the other hand, the performances of this approach are strictly related on the quality of the template and, specifically, by its similarity to the patient skull. Albeit significant efforts have been spent to improve the automatization of template-based processes, the human interaction remains essential. For instance, all the presented processes rely on a manual selection of landmarks. Moreover, given the lack of objective techniques for the placement of reference points, this step is prone to introduce alignment errors.

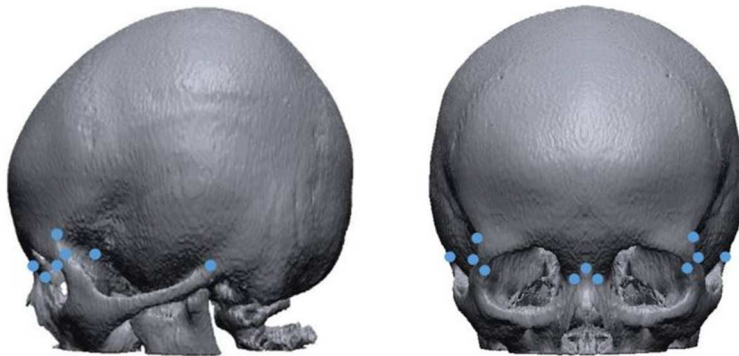


Figure 2.1: Anatomical Landmarks used in [20]

A particular class of *Template-based* approach is based on the *Mirroring* method. In this dissertation, this method is considered as a *Template-based* since it incorporates, in the reconstruction of unilateral defect, the knowledge encoded in the healthy half of the cranial vault used as a template. Being however the most commonly used method for its effectiveness

and simplicity in the correction of unilateral defects, the state-of-the-art of the Mirroring method will be dealt with in the following dedicated subsection.

### 2.1.1. Mirroring

Historically, research investigating the reconstruction of skull defects has first focused on the exploitation of the skull symmetry, w.r.t. the sagittal plane, to retrieve missing geometry. This approach, called *Mirroring*, proposes the reflection of the non-defective side of the skull onto the defective one to reconstruct the missing surface (Figure 2.2). The first systematic mirroring approach was presented in literature in the early '90s [25]; the authors describe several medical applications for 3D anatomical digitized data and assess the potential advantages attainable by applying the mirroring technique in cranioplasty, for the generation of titanium implants.

More recently, interesting case studies are presented in [12] and [26]. Both the papers present the results obtained applying state-of-the-art RE software tools to: *i*) process the original STL data, *ii*) identify and mirror defective parts of the skull and *iii*) wrap the healthy surface upon the defect to produce the final result. Boolean operations are used in [12] to isolate the set of points required to reconstruct the defective area.

The usefulness of the *mirroring-based* approach, regardless of its simplicity, is proved by the wide number of works leveraging this method [27 – 33]. Unfortunately, the typical implementation of the method requires several manual operations that are *i*) the computation of the symmetry plane, *ii*) the isolation of the healthy region corresponding to the defect, and *iii*) the adjustment of the reconstructed patch on the defective side of the skull. These operations are not trivial since the human skull is never perfectly symmetrical. In this context, most recent research is oriented towards the development of advanced strategies for the automatic identification of the symmetry plane in highly asymmetrical anatomies [34], and for the adaptation of the reconstructed patch upon the defective area. With this respect, an effective smoothing strategy has been recently presented in [35], where a Laplacian smoothing, combined with a Delaunay triangulation, is used to retrieve the patch of the missing part.

It is important to note that some elements severely limit the efficacy of the *mirroring-based* approach: firstly, it can be applied only with reference to the treatment of unilateral skull damages. Whenever the defect crosses the sagittal plane, no useful geometry information can be extracted from the original data.

Moreover, the procedure relies on manual and time-consuming operations which cannot be easily automatized due to the wide interpersonal variability of the skull anatomy as well as the difficulty in defining an effective plane around which perform the mirroring.

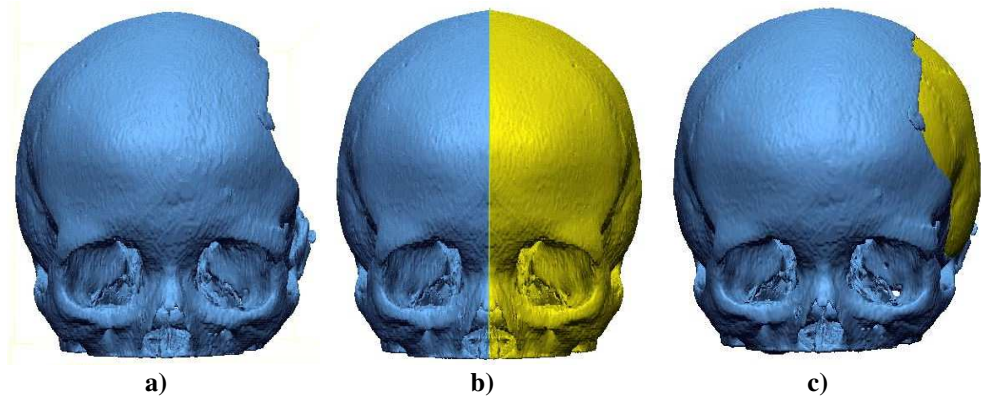


Figure 2.2: An example of the Mirroring approach: (a) the starting defective skull; (b) the reflection of the non-defective side; (c) the reconstructed patch.

## 2.2. Surface Interpolation-based Techniques

*Surface interpolation-based* approaches pursue the generation of a smooth approximation of the skull shape across the defect region. The result is a mathematical surface characterized by a certain degree of continuity w.r.t. the defect edge.

For the specific geometry of the skull and the defect boundaries, the interpolating function must be able to work even when the interpolation centers do not form a regular grid. Furthermore, for ensuring a coherent reconstruction, the surface must provide at least a  $C^1$  continuity in order to avoid creases. For these reasons, Carr et al. [36] and Zhou et al. [37] indicate the Radial Basis Functions (RBFs) as an appropriate choice due to the few restrictions imposed on the geometry of the interpolation centers and its capacity to guarantee a  $C^1$  continuity. In [36], RBFs are fitted to depth maps of the skull's surface, obtained from CT data using ray-tracing techniques. In particular, the surface interpolation uses the vertices of the defect's boundary region as the centers of the RBFs. Carr identifies in the Thin Plate Spline (TPS) the best choice among the RBFs alternatives, since it "is the smoothest  $C^1$  interpolant in the sense that it minimizes the energy functional".

As an alternative, other authors propose different approximation methods for the skull reconstruction.

Chong et al. propose in [38] a semi-automatic hole repairing algorithm using quartic Bézier surface approximation starting from an initial triangulation obtained with a Genetic algorithm. The method starts with the hole identification, by simply checking for connected boundary edges that form a closed loop. Then, the triangulation of the defected area, using a Genetic algorithm, is performed to obtain a guide for the subsequent approximated Bézier Gregory patch. At the end, triangular meshes are created using a customized advancing front method and projected onto the Bézier surfaces.

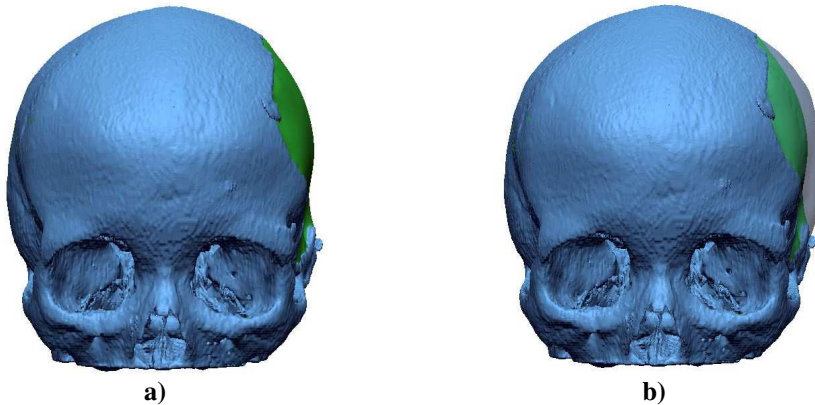
These approaches guarantee the main advantage of ensuring the continuity at the boundary. Furthermore, the resulting surface is mathematically defined, so it could be evaluated at any desired resolution. Despite these advantages, a significant limitation for interpolation approaches is the lack of constraints inside the defect region. For this reason, [36] and [38] highlight that the surface near to the defect margin has less reconstruction errors with respect to the center. Usually, the larger is the hole, the greater is the internal error. To partially overcome this drawback for large holes, [36] suggests the partitioning of the defect.

Alternatively, the use of a template to provide information on the curvature inside the defect is suggested in [38]. Even using these strategies, however, the *surface interpolation-based* methods are not straightforward to properly reconstruct large defect areas.

The same issue is described in [39]: the paper highlights that, dealing with large holes, it is usually impossible to control the shape only with the boundary points. As a result, the reconstructed surface results flat (see the example of Figure 2.3). Therefore, they use the points around the hole to get the shape of the adjacent area and generate the surface, and then adjust the insertion points on this surface to generate the new points. Finally, they repeat the two steps to adjust the shape and repair the holes. They also adopt a template matching method to repair part with complex shape (e.g. nose shape).

A different surface interpolation approach based on NURBS is presented in [40]. The authors start with an initial mesh of the patch surface defined over the skull defect area. The mesh points might be obtained either from points mirrored on the opposite side of the skull or from points sketched by doctors. By interpolating such mesh points with NURBS surfaces, a NURBS-format patch is obtained. Accordingly, the patch reconstruction requires a strong user interaction.

Several commercial reverse engineering software offer holes-filling tools based on the surface interpolation methods [41], but the problems faced are the same of those discussed above: the wider the hole, the flatter the reconstructed patch is.



**Figure 2.3:** (a) the defective part reconstructed by surface interpolation can lead to a too flat patch; (b) the comparison between the patch obtained with the surface reconstruction technique and using the mirroring technique (in transparency).

### 2.3. Slice-based Techniques

The last class of methods adopts a slice-by-slice approach for reconstructing the skull defect. The original 2D diagnostic CT slices are used to extract the bone contour. The idea is to push a mathematical curve to fit the bone contour by minimizing the energy of a functional (see Figure 2.4 for an example). Since in the single slice the geometry of the skull is almost elliptical [42], the curve in each image can be modeled starting from an oval shape.

As widely recognized, the Active Contour Models (ACM), also known as *Snakes*, are evolving curves driven by a minimization of the internal and external energies. The characteristics of ACM enable the generated curve to closely match the skull border. Liao et

al. in [43] and [44] successfully applied ACM for medical application, but the authors mainly use *Snakes* in image segmentation and noise elimination rather than directly for skull modeling. The actual surface reconstruction is based on a multiresolution image registration between the defective skull and a previously acquired CT image of the intact patient one. Evidently, this approach can be applied only whenever a CT scan of the healthy skull of the patient is available.

To the best of authors' knowledge, the only works that use *Snakes* for the skull modeling are [45] and [46]. After filtering out the inner and outer skull borders, in each CT slice suitable arcs can be computed using *Snakes*. Finally, all the previously processed CT images are stacked to build the 3D skull model.

An approach based on ellipses that is capable to perform a self-adjustment upon the bone curvature is proposed in [42,47]. These methods propose a Particle Swarm Optimization algorithm [21] and Genetic algorithm [47] adjustment in order to find the best solution for each tomographic slice. Both the papers propose the concept of "super-ellipse" to recover the parameters fitting the skull shape in each CT slice. The arcs describing the missing bone shapes for each slice are recovered from the final configuration of the ellipse. Once the solution is found for each slice, the whole 3D missing information can be virtually rebuilt. An important open issue for this method is that such reconstruction does not ensure the continuity between the reconstructed patch and the surrounding healthy bone, which is a critical request to attain an acceptable aesthetic outcome.

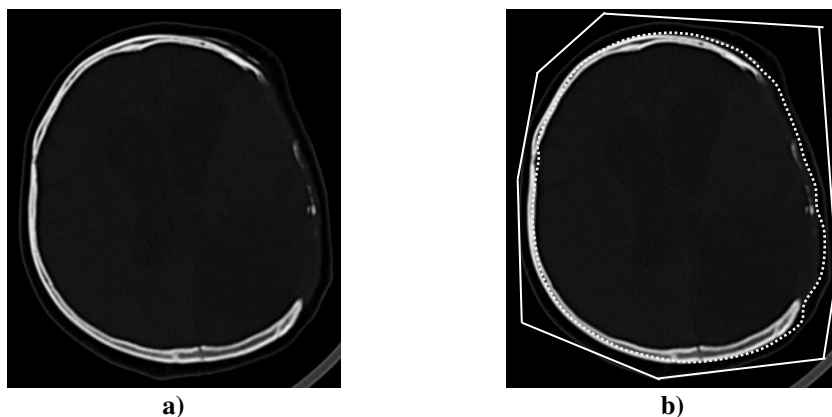
Another approach is proposed by [48], where a new hybrid level set model based on edge and region information (without re-initialization) is proposed. The processed image is segmented using the novel hybrid level set method according to the skull and brain tissue information to obtain the complete inner contour of the skull. The outer contour is obtained starting from the initial curve by means of an offset operation. It needs to be pointed out that, by using the brain tissue profile resulting from the segmentation to determine the skull shape in the defect area, acceptable result could not be achieved. In other words, depending on the patient' condition, the brain shape could not correspond to the desired skull inner contour.

In [49] a procedure to create outer surface meshes of intact bones starting from 2D bone contour is presented. Considering each slice, the bone contour is classified according to three different variants of "loops". The classification is built depending on the distance between the start and endpoint of the loops, the percentage of enclosed polyline points, and the global/local property of the loop with respect to the entire contour area. A "loop removal" procedure to obtain close curves defining the outer shape of the skull bone is subsequently applied; such procedure is tailored for each type of loop identified for each slice. The algorithm automatically detects each defect zone. The defect is reshaped by a closed spline approximating the bone contour (using a periodic least-squares approximation method). A Thin Plate smoothing spline is then evaluated only for the enclosed surface entities. Starting from the spline set, a triangulated surface representation is built.

An alternative approach is defined in [50], where the missing bone is created by a 3D orthogonal neural network. For each CT slice, the inputs are the horizontal coordinate  $x_i$  of the healthy bone and the CT image number, that is transformed as spatial coordinate  $z_i$ . After the neural network has been properly trained, vertical coordinate  $y_i$  of the missing pixels within the defect are derived.

Despite the potentialities of this class of approaches, some of these methods are affected by the same problem discussed for the *Surface interpolation-based* class, that is the lack of information inside the defect area. Consequently, whenever a large-hole reconstruction is

faced, the information available only at the boundary, namely the curvature, is not sufficient for an effective reconstruction of the original shape.



**Figure 2.4:** A slice in a TC of a defective skull (a) and the resulting boundary (dotted line) fitted on the bone surface, obtained by ACM starting from a coarse approximation (solid line).

## 2.4. Open Issues

A comprehensive analysis regarding the SoA of the virtual reconstruction strategies for defective cranial vaults has been presented in the previous sections. Several approaches to address the problem have been identified and discussed. A general classification of these approaches depending on the adopted reconstruction strategy has been proposed: *Template-based*, *Surface Interpolation-based* or *Slice-based*. As can be seen from the previous sections, a strict classification cannot be entirely defined, as some methods [20, 24, 32\_review] exploit tools belonging to more than one strategy. For instance, the *Mirroring* strategies are widely used to extract missing data on the defective area to be used as input in other techniques.

The findings of this analysis suggest that the problem is still open, as proved by the recentness of published works. Indeed, a definitive solution has yet to be found, as the proposed approaches are affected by significant, although different, drawbacks (see Table 2.1): they all share weaknesses and limits that mainly are characterized by a high user interaction (*Template-based* Techniques) or the lack of data within the hole that could affect an aesthetically acceptable reconstruction (*Surface Interpolation-based* Techniques and *Slice-based* Techniques).

A fundamental condition for the application of most methods is that a previous definition of complex geometric reference features is required, i.e. the skull symmetry plane or anatomical landmarks. The high user-dependency of existing strategies for defining such geometric reference feature is another limiting factor. Evidently, the development of automatic techniques for all the tasks described above (e.g. automatic landmarks positioning, as proposed in [51, 52] for other anatomical parts, or automatic segmentation techniques [53]) is not trivial due to the complex surfaces that define the human skull anatomy and the lack of precise references. Despite that, continued efforts are needed to make reconstruction approaches more accessible to the medical staff, automatizing the entire procedure, hence removing the need of a user with advanced CAD skills.



This research contributes to these efforts by implementing an automatic algorithm able to provide a consistent reconstruction methodology for defective or deformed cranial vault; the methodology intends to solve the just discussed limitations of the existing methods. The algorithm has basically a *Surface Interpolation-based* approach, able to mathematically ensure the continuity on the boundary with an easily automatable procedure. To overcome the related drawbacks, represented by the lack of information within the hole, the reconstruction is driven by some significant points added in the missing area by means of a *Template-based* approach.

A comprehensive and exhaustive description of the proposed methodology is presented in the following Chapter.

**Table 2.1: Comparison of advantages and disadvantages of different Skull Virtual Reconstruction strategies**

Neurocranium Virtual Reconstruction Strategy	Strengths	Drawbacks	References
<i>Template-based</i>	<ul style="list-style-type: none"> <li>+ Delivers information within the defect</li> <li>+ Incorporates the knowledge encoded in the template</li> <li>+ Enables to exploit directly the patient data for unilateral defect</li> </ul>	<ul style="list-style-type: none"> <li>– Requires high user interaction</li> <li>– Continuity between the health skull and the reconstructive patch not assured</li> <li>– Reconstruction strictly related to the template</li> </ul>	[1] [6] [8] [9] [13] [14] [19] [20] [24] [25] [27] [29] [30] [34] [35] [36] [43] [44]
<i>Surface Interpolation-based</i>	<ul style="list-style-type: none"> <li>+ Assures continuity between the health skull and the reconstructive patch</li> <li>+ Patch reconstructed with a mathematically defined surface (retrieved data is not discrete)</li> </ul>	<ul style="list-style-type: none"> <li>– The wider the hole, the more difficult it is to reconstruct a correct shape of the cranial vault because of the lack of constraints inside the defect region</li> </ul>	[3] [4] [7] [28] [46]
<i>Slice-based</i>	<ul style="list-style-type: none"> <li>+ Assures continuity between the health skull and the reconstructive patch</li> <li>+ Patch reconstructed with a mathematically defined curve (slice by slice retrieved data is not discrete)</li> </ul>	<ul style="list-style-type: none"> <li>– Lack of information inside the defect area</li> <li>– Need to stack the curves obtained slice by slice (slice by slice retrieved data is discrete)</li> </ul>	[2] [5] [22] [26] [32] [33] [39] [45]



### 3. The proposed *hybrid* approach for the reconstruction of a human neurocranium

The previous section has presented a thorough description of the most representative existing strategies addressing the virtual restoration of a cranial shape. As discussed, despite the large number of alternatives which can be found in literature, a convincing solution has not been yet proposed; in particular, an approach able to ensure an easily automatable procedure with a consistent shape reconstruction has not still available.

Drawing inspiration from the existing approaches, a novel reconstruction method has been devised addressing the issues identified by the SoA analysis: a new *hybrid* procedure is here proposed (see Figure 3.1) in order to overcome the drawbacks reported in Table 2.1. The procedure aims the automatic restoration of the exocranial surface of a defective neurocranium, ensuring both the symmetry of the resulting skull and the continuity between the reconstructive patch and the surrounding bone.

The presented approach is *hybrid* since a surface which interpolates a proper point-set is used to restore the defect (as in a *Surface Interpolation-based* approach), but the lack of information in the missing/deformed regions is compensated by external sources (as in a *Template-based* approach). The idea is to use the strengths of each of these approaches to overcome the drawbacks of the other: the ability of the *Template-based* methods to provide knowledge of the missing or deformed region is exploited to guide a *Surface Interpolation-based* algorithm. Adding meaningful information within the affected region allow a data-driven reconstruction able to ensure a consistent result.

This way, the procedure overcomes the main limitations of *Surface Interpolation-based* techniques representing by the lack of information within the hole which usually leads to non-consistent results, especially if the hole is large [38]. At the same time, maintaining a *Surface Interpolation-based* approach makes the procedure easily automatable, while it is very difficult to automate a purely *Template-based* approach. As explained in Section 2.1, for this kind of approach, a high user's interaction is essential to obtain a good matching between the deformed template and the model to be reconstructed. Furthermore, and also in case of an excellent matching, a post-processing is still required to ensure continuity between the reconstructive patch and the healthy bone. On the contrary, a *Surface Interpolation-based* approach allows to mathematically impose such continuity by considering an adequate amount of points located at the edge of the defect as centers of the interpolation.

As a consequence, in the proposed approach the user interaction is limited to a proper preparation of the starting model and to the selection of a single point on the edge of the hole that needs to be repaired. This results in a less cumbersome and time-consuming procedure

when compared with both *Template-based* and *Slice-based* approaches. Moreover, the presented procedure is landmark-independent. The selection of landmarks is not a trivial task and requires expert users to be accomplished: it is prone to introduce alignment errors given the lack of objective techniques for the robust definition of reference points.

The proposed procedure has been implemented in an original software coded in MATLAB® and several test cases, of both synthetic and real defective skulls, are addressed in order to verify its capability in restoring large defects ( $>100\text{cm}^2$ ) (see Chapter 5).

Additionally, a new metric to evaluate the quality of the reconstruction outcome is proposed.

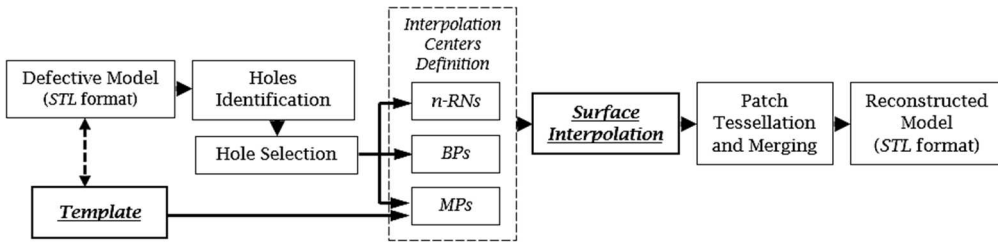


Figure 3.1: The proposed *hybrid* procedure

### 3.1. Methods and Tools

Before presenting the actual implementation of the proposed method, a brief description of some fundamental notions is reported in the following subsections for a better understanding of the whole procedure. For an exhaustive description of the methods and tools used in the development of the algorithm, see Chapter 4.

#### 3.1.1. Shape

Dealing with complex geometries, it may be too complicated – or even impossible – to work with their mathematical description and, more important, it may be not possible to describe them as a composition of basic geometric entities (i.e. planes, cylinders, spheres, etc.): consequently, it is very difficult to compare different objects simply comparing their external boundary or surface. For this reason, for a reliable comparison among different objects it is necessary to refer to their *shape*: the shape of an object is all the geometrical information that is invariant to rigid transformations (i.e. translation and rotation) and uniform scaling [54].

According to this definition, the shape is not usually related to the size and placement in space of the object. However, in some fields and specifically in biology, shape and scale could be correlated: scale variations can be considered in all respects as biological variations. As a consequence, in this thesis the shape is defined as the geometric information that persists once the effects due to position and rotation are eliminated [55]. The scale is instead maintained as information of significative variation of the shape.

Two shapes can be directly compared, and could be defined:

- *Congruent*, when they can be perfectly superimposed by a sequence of rotations, translations and reflections.

- *Similar*, when they can be perfectly superimposed by uniform scaling, together with a sequence of rotations, translations and reflections.
- *Isotopic*, when they can be perfectly superimposed by a sequence of deformations that do not tear the object or put holes in it.
- *Equivalent*, when they can be perfectly superimposed by uniform scaling, together with a sequence of rotations and translations.

So, it is worth to note that an object is not *equivalent* if compared to its mirrored image, even though they are *congruent* or *similar*: in three dimensions, the left hand is *congruent* to the right hand, but they have different shape.

In addition, and to consider non-rigid transformations, the notion of *homeomorphism* has been introduced: two *isotopic* shape are homeomorphic to each other because they can be perfectly superimposed by only stretching and bending operations. As an example, a sphere is homeomorphic to a cube, but not to a torus.

For the shapes under investigation, i.e. human cranial shapes, they can be considered homeomorphic to each other: it enables to perform non-rigid registration to superimpose different cranial shapes.

### 3.1.2. Data Representation

The straightforward but, at the same time, the most generic solution to represent complex shapes is by means of a discrete description based on a set of points distributed across the surface, usually referred to as *landmarks* [56, 57]. The resulting discrete model is called Point Distribution Model (PDM) [58]. In early approaches, *landmarks* refer to salient feature points and are usually manually selected. To date, complex 3D models requires a dense set of points for an adequate representation of the shape addressed. Therefore, they are not located as per the common definition (i.e. they do not indicate only salient feature) but are extracted from the whole volumetric model by proper algorithms (e.g. Marching Cube). In medical applications, the volume data is obtained through the segmentation task performed on the diagnostic images, as described in the Introduction chapter. The coordinates of the extracted points are stored in a vector, henceforward named  $\Gamma$ , that describes the 3D shape as PDM:

$$\Gamma = \{\mathbf{x}_k | \mathbf{x}_k \in \mathbb{R}^3, k = 1, \dots, N\} \quad (3.1)$$

where  $N$  is the number of points used to describe the shape.

$\mathbf{x}_k$  is a 3D vector containing the coordinates of each point of the PDM usually provided in a well-defined Cartesian coordinate frame  $x$ ,  $y$  and  $z$ :

$$\mathbf{x}_k = (x_k, y_k, z_k) \quad (3.2)$$

In addition to the PDM, from the volume data it is possible to retrieve also the connectivity information between the points of the PDM to allow the surface reconstruction and the calculation of the normal vectors. A point set with connectivity list is called a *mesh*, and it is usually saved in STL format. Commercial software systems (e.g. Materialise Mimics® or 3DSlicer®) typically use a Marching Cube Algorithm to obtain the *mesh* from the volumetric data.

Although this representation is discrete, and the information stored in it is of low level, this way it is possible to describe complex geometries including those that usually depict anatomical structures. For this reason, PDM or STL are used extensively for the study of biological shapes [56, 59, 60].

The proposed procedure requires the 3D model of the ROI provided as STL file. As a consequence, all mathematical definitions will be referred to a 3D model delivered as STL, i.e. described by a set of points  $\mathbf{x}_k$  and the related connectivity list.

### 3.1.3. Template Definition

As widely explained in the previous sections, the proposed algorithm has basically a *Surface Interpolation – based* approach, but the reconstruction is guided by some meaningful information provided by a template able both to properly match the defective target model and to approximate the missing/deformed region in a consistent way.

It is worth remembering that, as highlighted in the Introduction section, a consistent reconstruction in cranioplasty means a resulting skull as symmetrical as possible without any visible discontinuity between the prosthesis and the bone.

The proposed algorithm uses two different methods to obtain a reliable template, depending on whether the defect is unilateral (i.e. it does not or slightly crosses the sagittal plane) or non-unilateral (i.e. the defect crosses the sagittal plane or there is not a healthy contralateral part to exploit as a template).

In the former case, the algorithm uses a mirroring technique to superimpose the healthy half of the cranial vault onto the defective one. This approach is the simplest way to provide information of the area to be reconstructed and exploits the patient's own data as a template, but the restoration outcome is strictly related to the definition of the *symmetry plane* around which performs the reflection. Speaking about a *symmetry plane* in human skull is obviously only an abstraction since a perfectly symmetric cranium does not exist; but, at the same time, the definition of a reliable plane to perform the reflection is critical to ensure a precise superimposition between the template and the defective half. In this application, a new method able to locate a good approximation of skull's *symmetry plane* also in case of large defective area (i.e. in case of strong asymmetries) has been developed in collaboration with professors Di Angelo and Di Stefano from University of L'Aquila. A detailed description of the algorithm is provided in 4.2.

The healthy half mirrored around the so-detected plane is then used as a template for the subsequent reconstruction, as reported above.

In the case of non-unilateral defects, the algorithm exploits an external source represented by a properly defined deformable template reproducing a pathologically unaffected neurocranium.

The best way to deliver a suitable deformable template able to consistently reproduce anatomical structures is by means of statistical analysis methods, to gather and interpret information from a collection of samples belonging to the same class of shape (e.g. cranial vaults). A statistical representation of normal shape variations for the considered class makes possible to take into account the high complexity as well as the wide interpersonal variability of the anatomical structures. To date, *Statistical Shape Analysis* (SSA) [16 – 18] represents the most established statistical tool in medical image analysis [14, 56, 61]. SSA provides a template, usually referred to as *Statistical Shape Model* (SSM), able to define a new consistent not defective shape still belonging to the same family of shapes of the initial training set. An SSM is basically defined by a *mean shape* and a series of *Modes of Variation* (MoVs) learned from the initial training set. The MoVs represent all possible shape deformations, i.e. the way in which each point of the mean shape can be distributed in space remaining in the same family of shape. As a result, the provided template is a linear parametric model with mathematically convenient properties.

SSM has been widely proposed in orthopedics, especially for anatomical bone modelling, joint cinematic analysis, staging of morphological abnormality, and pre- and intra-operative reconstruction [62]. Furthermore, SSM has already proved its reliability as a template for cranial vault reconstruction [14].

The downside of the SSM is that a lot of training data is needed to provide a pliable enough model to adequately describe all the possible target shapes. Since the training data must be represented by pathological unaffected ROI (usually extrapolated from diagnostic imaging), it could be not trivial to find an adequate number of this kind of data.

Section 4.1 reports a comprehensive description of the SSA strengths and limitations as well as the description of the procedure developed to build a reliable parametric model for the human neurocranium starting from 100 adult healthy human crania.

The operator selects between the two reconstruction strategies (i.e. mirroring or external source), depending on if the defect is unilateral or non-unilateral.

## 3.2. Algorithm implementation

In this section, the *hybrid* procedure briefly described in Figure 3.1 is presented in detail.

### 3.2.1. Model pre-processing

The developed procedure works with the surface mesh representing the defective skull in STL format obtained by a proper image segmentation from the patient's CT or MRI data. Dealing with hard tissues, the CT images are particularly suitable because bones appear with a well-identifiable greyscale intensity window. Therefore, a gray-value thresholding with easily recognizable lower and upper bounds can be applied to filtering out the surrounding tissues from the region of interest. To date, many commercial software packages (e.g. Materialise Mimics® or 3DSlicer®) provide internal tools for such segmentation as well as for exporting the obtained 3D model in STL format.

Since the aim of the proposed algorithm is to restore the external shape of the cranial vault, the procedure requires only the exocranial surface, i.e. the external crust of the skull's mesh, as input. For this reason, only the exterior poly-faces of the STL model are used as an input model (Figure 3.2). Thanks to the regularity of the cranial vault shape, the operations required to the exterior poly-faces selection is straightforward: in the actual implementation, the selection of the exocranial surface is automatically carried out by using a ray-tracing algorithm. The selection algorithm defines an adequate number of *rays* that originate in the centroid of the model and sweep the space in all directions. The STL faces are set as fully transparent so that the exocranial surface can be defined by the last triangle encountered by each ray (Figure 3.3). As a result, the new mesh is no longer a 2-manifold watertight mesh (as resulting from the segmentation step) and each couple of vertices forming the defect boundary is connected by an edge not shared by two faces.

Further manual cleaning of the model is usually required to deliver a proper model on which to apply the procedure. The optimal input model is shown in Figure 3.2(b). Although the algorithm has proved to be not very sensitive to the quality of the input model, its proper definition allows minimizing the risk of reconstruction failure.

In the following,  $\Gamma$  (as defined in Equation 3.1) will represent the PDM of the starting exocranial model.

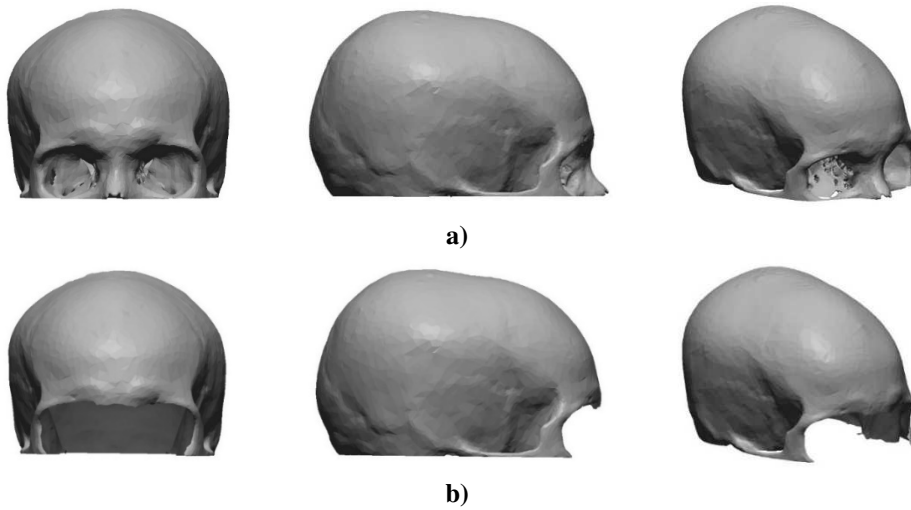


Figure 3.2: a) the neurocranial 3D model as exported after the segmentation; b) the exocranial surface after the pre-processing

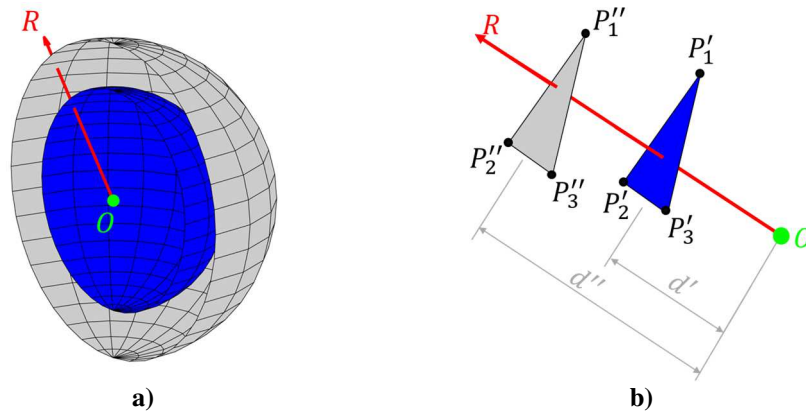


Figure 3.3: The ray-tracing algorithm to select the external surface (in grey). a) Each ray originates from the centroid  $O$  and intersects the surface of the model; b) only the outermost face (i.e. the face with the greatest distance  $d$  from the centroid) is selected

### 3.2.2. Identification of the hole

Once the STL model of the exocranial surface is available, the procedure firstly requires the identification of the boundary edge of the defects. Two types of defects can be found, categorized as *simple* and *ring* holes [38]. A *simple* hole is characterized by only one boundary loop without any internal portions of bone (island), while a *ring* hole has internal islands and therefore at least two independent edges are present. Since during the segmentation a *ring* hole can be easily reduced into a *simple* one by removing the islands or making some bridges between the edges, the proposed approach deals only with *simple* holes.



The properties of the STL are exploited for the automatic identification of the *free edges* on the model. An edge (i.e. each couple of connected points) is considered *free* when it is not shared by at least two triangles (Figure 3.4). Since the starting model  $\Gamma$  is not a 2-manifold watertight mesh, as said in Section 3.2.1, not only the defects' boundaries are selected if all the *free edges* are considered. In this case, all the free edges of the exocranial surface are collected as possible defects. For this reason, the user is required to select one point on the edge of the hole to be filled (using a proper devised GUI). This is the only interaction required to the user in the whole procedure. Starting from this selected point, the boundary loop of the defect under investigation is automatically retrieved. It is worth to note that the algorithm has been designed to repair only one defect at a time.

The points  $\mathbf{x}$  identified as belonging to the edge of the defect to be repaired are named  $\tilde{\mathbf{x}}$  and stored in a vector  $\Lambda$  defined as in Equation 3.3. Henceforward, the points  $\tilde{\mathbf{x}}$  are named *Boundary Points (BPs)*.  $N_d$  is the number of points  $\tilde{\mathbf{x}}$ .

$$\Lambda = \{\tilde{\mathbf{x}}_i | \tilde{\mathbf{x}}_i \in \mathbb{R}^3, i = 1, \dots, N_d\} \quad (3.3)$$

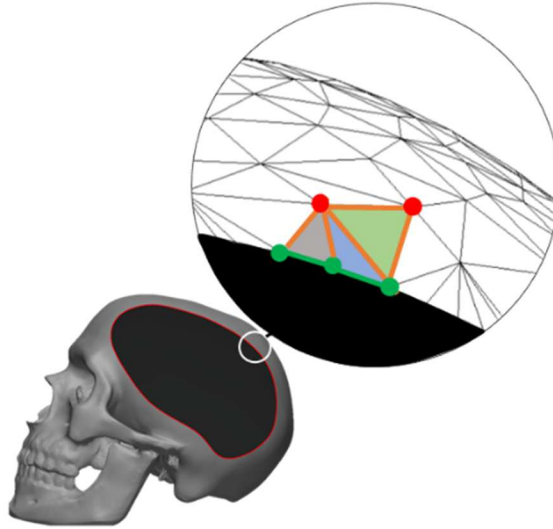


Figure 3.4: Automatic edge detection (*free edges* and *BPs* are reported in green)

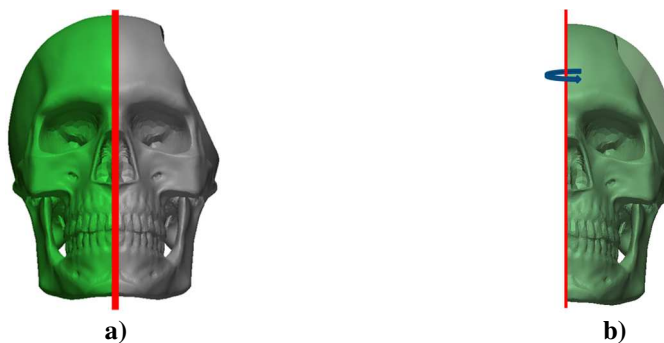
### 3.2.3. Missing Points Definition

The definition of the *Missing Points* represents the most relevant step forward introduced by the proposed procedure. In the Chapter 2 it has been already highlighted that the direct application of a *Surface Interpolation-based* approach, despite it represents the only way to obtain an easily automatable procedure, usually leads to questionable results especially in case of large defects. This is due to the fact that the interpolation is performed through the points around the hole to get the continuity of the reconstructive patch with respect to the surrounding bone, but it is difficult to control the shape only with the points located on the boundary. Usually, the surface close to the defect margin has less reconstruction errors with respect to the center, due to the lack of constraints inside the defect region. As a result, the reconstructed surface typically results in a wrong curvature (see the example reported in Figure

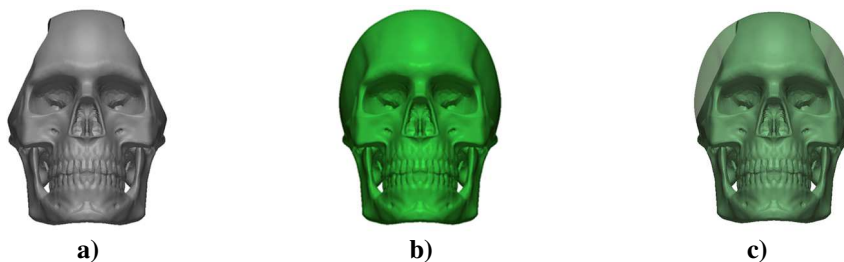
2.3). This represents the most important limitation considering the whole category of methods based on surface interpolation (Table 2.1).

Cheng in [38] suggested to use a reproduction of the pathologically unaffected ROI as a template to guide the interpolation inside the defect: once the template is properly deformed to match the known part of the defective model to be reconstructed it must be able to consistently provide the information on the curvature of the missing area. As explained in Section 3.1.3, an effective solution to obtain such a template is the mirroring of the contralateral part, if the defect is unilateral, or using a Statistical Shape Model in case of non-unilateral defects. The proposed algorithm allows the operator to choose one of these two approaches, depending on whether the defect to be reconstructed is unilateral or non-unilateral.

Although the deformed template encodes the knowledge of the healthy shape of the considered model, how to retrieve such information is not a trivial task: typically, *Template-based* approaches encompass the use of the whole part corresponding to the missing region as a reconstructive patch. Since the template and the target model are never perfectly superimposed, the adaptation of the retrieved patch requires labor-intensive user's interaction to achieve the continuity with the surrounding regions. This limitation affects also the mirroring approach since the *symmetry* in the human skull is only an abstraction and a perfectly symmetric skull does not actually exist.



**Figure 3.5:** a) for unilateral defect the healthy half is used as template and b) mirrored onto the defective one



**Figure 3.6:** for a non-unilateral defect (a) an external template (b) representing the unaffected ROI is used to match the defective model and retrieve the missing information (c)

To enable a data-driven interpolation without any heavy user's interaction or patch adaptation, a new approach is proposed: once the template is defined and properly superimposed onto the defective model (Figure 3.5 and Figure 3.6), only a few meaningful points within the missing region are selected (see Figure 3.7) rather than extrapolating the entire region using it directly as the reconstructive patch. Such meaningful points,

henceforward named *Missing Points (MPs)*, are used as nodes to guide the subsequent surface interpolation.

The *MPs* are defined starting from the deformed template measuring the Euclidean Distance between each point of the template (*query points*  $q_i$ ) and its nearest one belonging to the defective part (*reference points*  $r_i$ ). The nearest points are defined by means of the *k-Nearest Neighbors* algorithm. A simple Boolean subtract cannot be applied because, as reported above, a perfect superimposition between the model and the template is never ensured.

Only the *query points* whose distances to their correspondent nearest neighbors are greater than an imposed threshold  $\bar{d}$  are kept as eligible *MPs*, while the others are filtered out.  $\bar{d}$  is an input of the procedure and represents the maximum distance to search the model's points as neighbors of the ones belonging to the template. Unfortunately, this step identifies the *MPs* of all the cranial holes. Therefore, only the *MPs* inside the selected boundary loop need to be considered.

Finally, points that are at a distance less than a certain value  $m$  from the edge itself are further filtered-out to detach *MPs* from the boundary.  $m$  represents the minimum distance (in mm) between the boundary and its nearest ring of the *MPs*, as showed in Figure 3.7. Too little value of  $m$  could affect the continuity between the skull and the reconstructive patch, while a too great value could be unable to lead to an acceptable outcome due to a lack of information within the hole.

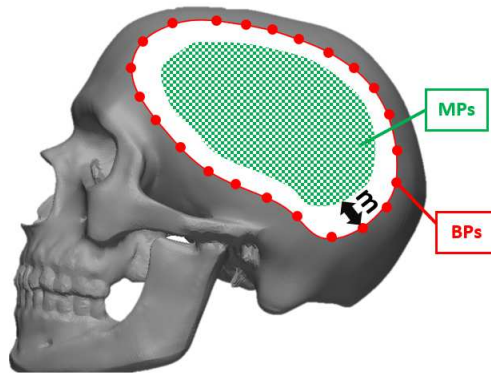


Figure 3.7: the *MPs* and the *BPs*

### 3.2.4. Definition of the Interpolation Centers

The actual definition of the restoration patch is obtained by means of a Surface Interpolation using a properly designed points-set. Considering the missing bone as a 3D surface described by a function  $f: \mathbf{R}^2 \rightarrow \mathbf{R}$  whose value  $f(\mathbf{X}_i)$  is known only on a limited number of points  $\{\mathbf{X}_i \in \mathbf{R}^2: i = 1, 2, \dots, N\}$ , it can be approximated by a properly designed function  $s: \mathbf{R}^2 \rightarrow \mathbf{R}$  which satisfies at least the *interpolation condition*  $s(\mathbf{X}_i) = f(\mathbf{X}_i)$ .  $\mathbf{X}_i$  are called *nodes of interpolation* or *interpolation centers*, and represent the  $(x_i, y_i)$  coordinates of each vertex  $i$  in the STL model, while  $f(\mathbf{X}_i)$  represent the correspondent  $z_i$  values.  $N$  is the total vertices number.

Several authors have proposed such approach for the cranial vault reconstruction using different interpolation strategies [13], but the surface  $s$  is usually defined with the  $\mathbf{X}_i$  nodes represented only by the *Boundary Points (BPs)*, i.e. the vertices forming the edge of the defect that must be filled. This allows achieving the geometrical continuity between the skull and the reconstructed patch thanks to the *interpolation condition* but proves to be inadequate for the correction of large defects, since the information at the boundary is insufficient to guide a consistent reconstruction within the hole. As a result, the patch tends toward a too flat shape [38]. To overcome this limitation, the proposed approach uses not only the *BPs* but also the above-defined *MPs* as nodes of interpolation.

Furthermore, to ensure the continuity between the healthy bone and the corrective patch, an overlapping region between the reconstructed surface  $s$  and the healthy skull is created by adding the *n-Ring Neighbors (n-RNs)* of the boundary loop to the interpolation nodes i.e. the set of points within a given distance  $n$  lying in the outer side of the boundary (see Figure 3.8).  $n$  is a further input of the algorithm: the higher  $n$ , the wider the overlapped region. However, the larger the set of points to be interpolated becomes, the greater is the computational time. Moreover, increasing  $n$  does not ensure a better reconstruction, since there is the possibility to exceed the cranial vault towards more complex areas (e.g. zygomatic or orbital region), thus increasing the complexity of the interpolation nodes.

Summing up, moving away from the SoA *interpolation-based* techniques that consider only the *BPs*, the proposed complete nodes-set  $\mathbf{X}$  contains (Figure 3.8):

- *Boundary points (BPs)*: all the points  $\mathbf{X}_{BP} = [x_{BP}, y_{BP}, z_{BP}]$  on the edge of the hole must be repaired.
- *Missing Points (MPs)*: all the points  $\mathbf{X}_{MP} = [x_{MP}, y_{MP}, z_{MP}]$  of the healthy template falling within the defect whose distances from the defect's edge is greater than  $m$ .
- *n-Ring Neighbors (n-RNs)*: the *n-Ring Neighbors* of the boundary loop, containing the points  $\mathbf{X}_{RN} = [x_{RN}, y_{RN}, z_{RN}]$ .

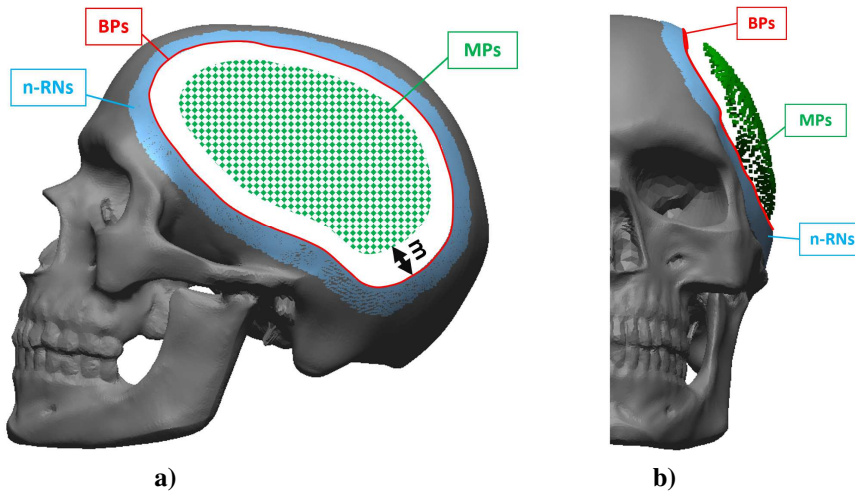


Figure 3.8: The Interpolation centers set: (a) lateral view, (b) frontal view.

### 3.2.5. Surface Interpolation

Among the different surfaces  $s$  proposed in the related literature to solve the interpolation problem (e.g. Quartic Bézier Gregory Patch, Active Control, NURBS) [13], a Radial Basis Function (RBF) named Thin Plate Spline (TPS) has proved to be the most suitable for the proposed approach [36]. TPS is particularly adequate because ensures a  $C^1$  continuity, uses the *smoothest* interpolator of  $f$  and guarantee the lowest computational time. Furthermore, RBF impose few restrictions on the nodes' geometry, being particularly suited to problems where the interpolation centers are represented by a set of scattered data with large data-free region. Using RBF, the interpolating function  $s(\mathbf{X}_i)$  is:

$$s(\mathbf{X}) = p(\mathbf{X}) + \sum_{i=1}^N \lambda_i \Phi(\|\mathbf{X} - \mathbf{X}_i\|) \quad (3.4)$$

As Equation (3.4) shows, RBF are described by the sum of  $N$  Radial Basis Functions  $\Phi$ , each associated with a different center  $\mathbf{X}_i$  and weighted by an appropriate coefficient  $\lambda_i$  plus a low-degree polynomial  $p$ .  $\|\cdot\|$  denotes the Euclidean norm. Regarding the Radial function  $\Phi$ , the specific Thin Plate Spline formulation is:

$$\Phi(r) = r^2 \log(r) \quad (3.5)$$

Using the TPS, the *interpolation condition* is avoided in favor of minimizing the energy functional  $E(s)$  (Equation (3.6)) over all interpolants  $\mathbf{X}_i$ .

$$E(s) = \int_{\mathbf{R}^2} \left[ \left( \frac{\partial^2 s}{\partial x^2} \right)^2 + \left( \frac{\partial^2 s}{\partial x \partial y} \right)^2 + \left( \frac{\partial^2 s}{\partial y^2} \right)^2 \right] dx dy \quad (3.6)$$

Avoiding a strict interpolation in favor of an actual approximation allows great advantages in terms of computational time and smoothness, but an iterative refinement on the *Boundary Points* is required to ensure an adequate continuity between the bone and the patch. The iterations are stopped when the following condition is reached:

$$|f(\mathbf{X}_{i,BP}) - s(\mathbf{X}_{i,BP})| \leq tol \quad (3.7)$$

Where  $f(\mathbf{X}_{i,BP})$  is the  $f$  value known on each  $BP$  node,  $s(\mathbf{X}_{i,BP})$  is the  $s$  value defined on each  $BP$  node and  $tol$  the maximum tolerance imposed in the whole set of  $BPs$ .

In this thesis,  $tol$  is imposed equal to  $10^{-2}$ , that represents a good compromise between accuracy, if compared with the CT maximum resolution (around  $0.5 \text{ mm}$ ), and calculation time.

The tolerance is imposed only on the  $BPs$  since the  $MPs$  are only useful as a reference for the consistent shape restoration within the hole, while the  $n-RNs$  are used to ensure the right curvature at the boundary. Defining soft constraints on the  $MPs$  prevents the surface from being over-constrained, especially when the template and the target model are not properly superimposed: in fact, the function of the  $MPs$  is only that of guiding the reconstruction rather than of defining the actual shape.

That said, a direct comparison between the known  $f(\mathbf{X}_i)$  and the corresponding calculated  $s(\mathbf{X}_i)$  in all the test cases addressed (some of which are reported in the Chapter 5) shows an approximation error lower than  $10^{-1} \text{ mm}$  with respect to the  $MPs$  and the  $n-RNs$ , demonstrating a more than acceptable approximation even for the points not located on the boundary.

### 3.2.6. Transformation of the Data

To avoid interpolation errors, a proper alignment of the nodes  $\mathbf{X}_i$  to the global reference system, identified by the  $x$ ,  $y$  and  $z$  axes, is performed before the actual application of the surface interpolation step. This allows minimizing the number of the points  $f(\mathbf{X}_i)$  that share the same  $\mathbf{X}_i$  consequently obtaining, as far as possible, a single-valued function  $s(\mathbf{X}_i)$ .

Therefore, a rigid translation  $\mathbf{T}_s$  is applied to the STL model until its centroid is on the center of the global reference system. Then, the best-fit plane  $\Pi_f$  through the points  $f(\mathbf{X}_i)$  is defined and the angle  $\vartheta$  between its normal  $\mathbf{n}_f$  and the direction  $z$  is measured. The angle  $\vartheta$  is used to apply a rigid rotation  $\mathbf{R}_\vartheta$  to both the  $\mathbf{X}_i$  and the  $f(\mathbf{X}_i)$ . As a result, the normal vector of the  $\Pi_f$  is parallel to the  $z$  direction.

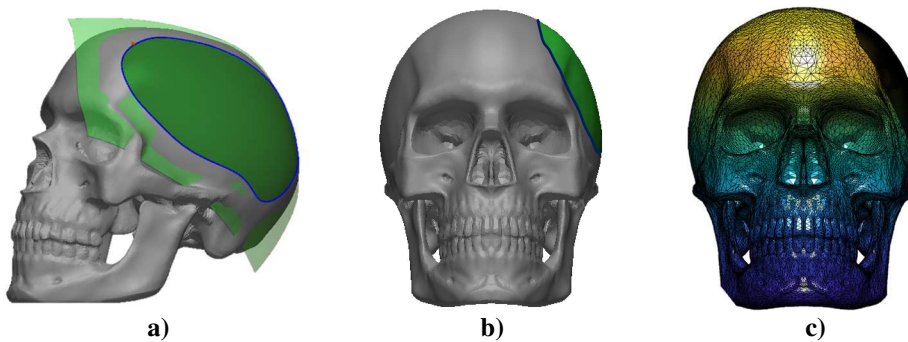
The actual application of the surface interpolation is then applied on the just-defined transformed nodes, named  $\tilde{\mathbf{X}}_i$ , with the corresponding transformed value  $f(\tilde{\mathbf{X}}_i)$ .

### 3.2.7. Patch Tessellation and Merging with the Defective Cranial Vault

Since the application of the TPS provides a mathematical surface exceeding the defect's boundary limits, the reconstructed patch is delimited using the boundary loop as defined in Section 3.2.2 (Figure 3.9).

Furthermore, being a mathematical surface, the delimited patch must be tessellated for the subsequent merging with the skull's STL model. The tessellation is carried out by a Crust-Based algorithm [63] defining a regular grid of nodes  $\{\chi_j \in \mathbf{R}^2: j = 1, 2, \dots, N\}$  in the  $xy$  plane. The resolution of the grid, from which directly depends the resolution of the reconstructive patch, is imposed similar to that of the original STL.

The tessellated patch is then rotated back to its original position, imposing a rotation guided by the  $\mathbf{R}_\vartheta^{-1}$  matrix. A complete re-mesh ensures the merging between the defective STL and the reconstructed patch. Finally, the inverse transformation  $\mathbf{T}_s^{-1}$  is applied to the restored skull in order to return it to its initial position aligned with the original CT images.



**Figure 3.9:** a) Surface interpolation; b) Surface delimitation using the boundary loop (in blue); c) the final STL merged model

## 4. Methods and Tools

In this chapter, a comprehensive description of the methods and tools designed for the actual implementation of the presented reconstruction methodology is provided. The following sections explain how these tools and methods have been developed or adapted to the application presented in this thesis.

### 4.1. Statistical Shape Analysis

The analysis of the geometrical properties of a specific *family* of shapes is usually carried out by statistical methods in order to detect, recognize and interpret the information collected from as many observations as possible; such a statistical approach, known as *Statistical Shape Analysis* (SSA) [14, 16 – 18, 56, 61], enables a reliable quantitative description of the *family* of shape under consideration.

The SSA involves robust and mathematically convenient tools (e.g. multivariate statistical tools) to face complex geometries, to synthesize, analyze and manage information delivered from the initial training set, defined by an adequate number of pathological unaffected samples (henceforward named training samples) of the ROI.

SSA provides a parametric model able to generate new plausible shapes, usually referred to as Statistical Shape Models (SSMs), belonging to the same family of shape of those contained in the training set used to define the model itself. The SSM accounts for the shape variations learned from the training set; these variations are represented by the leading principal components translated in actual deformations applied on the *mean shape* calculated among the training samples (see Equation 4.4).

To date, exploiting their ability to encode a-priori information of the healthy shape of the ROI, SSMs are widely used as templates for 3D medical image segmentation [56, 64], for the reconstruction of deformed or defective model [14, 65, 66] and for dysmorphisms and asymmetries recognition and evaluation [67 – 69].

The way to define the SSM heavily depends on the representation of the training samples. As said in Section 3.1.2, the straightforward solution to represent complex shapes is by means of a Point Distribution Model (PDM) [58], i.e. a discrete description based on a set of points (named landmarks) distributed across the surface [56, 57]. In biology, the statistical characterization of shape variations patterns based on Cartesian landmark coordinates, known as *Geometric Morphometrics*, is an approach grown out from early '900 and fully established with Bookstein [70] starting from the '80s. The great advantage in working with PDMs is that statistics on points are easily interpretable and have a physical significance; on the other hand, the high number of data (i.e. the dense set of points) required to adequately describe complex

3D shapes makes it difficult to gather and analyze the whole set of information. To reduce the problem's dimensionality without losing generality, the typical approach to SSM construction is based on Principal Component Analysis (PCA) [71].

With a PCA-based approach it is possible to define the space of all possible shape deformations described by the set of the  $M$  samples  $\{\Gamma^1 \Gamma^2 \dots \Gamma^M\}$  forming the training set. Each training shape  $\Gamma^i$  is represented as a PDM with a discrete set of landmarks  $\mathbf{x}^i$ . According to Equation 3.1,  $\Gamma^i$  can be defined as:

$$\Gamma^i = \{\mathbf{x}_{k_i}^i | \mathbf{x}_{k_i}^i \in \mathbb{R}^3, k_i = 1, \dots, N_i\} \quad (4.1)$$

Where  $N_i$  is the number of points used to describe the shape  $\Gamma^i$ , and  $\mathbf{x}_k^i$  contains the Cartesian coordinates, in three dimensions, of the  $k$ -th point.  $\Gamma^i$  is then a  $3 \times N_i$  matrix.

Each shape  $\Gamma^i$  is properly rearranged by stacking the coordinates of each point  $k$  in a large ( $3N_i$  elements) column vector  $\bar{\mathbf{x}}^i$ . Considering the global reference system in  $x$ -,  $y$ - and  $z$ -axis:

$$\bar{\mathbf{x}}^i = [x_1^i \ x_2^i \ \dots \ x_{N_i}^i \ y_1^i \ y_2^i \ \dots \ y_{N_i}^i \ z_1^i \ z_2^i \ \dots \ z_{N_i}^i] \quad (4.2)$$

As a result, the column vector reported in Equation 4.2 represents the  $3N_i$  variables of a single observation  $\Gamma^i$ .

To apply the PCA, the whole training set has to be then organized in a matrix (**TS**) whose columns are the observations (i.e. the  $M$  shapes) and rows are the variables:

$$\mathbf{TS} = [\bar{\mathbf{x}}^1 \ \bar{\mathbf{x}}^2 \ \dots \ \bar{\mathbf{x}}^M] \quad (4.3)$$

For a correct definition of the **TS**, i.e. for a correct definition of the raw dataset on which apply the PCA, it must be strictly assumed that the points are in *correspondence*, i.e. the points of all training samples are located at corresponding position. In other words, it means that the  $k$ -th landmark  $x_k^i$  and  $x_k^j$  of two shapes  $\Gamma^i$  and  $\Gamma^j$  represents the same point.

It is worth to note that the correspondence is an essential requirement for building the matrix **TS**: the PDMs from which to derive the training samples could be, and usually are, described by different number of points  $N_i$ . In order to obtain a proper **TS**, such models need to be reworked to satisfy the assumption mentioned before. When all the training samples are in correspondence, all the observations have the same number of rows  $N$ , and **TS** is a  $3N \times M$  matrix. Obviously, the larger is  $N$  and the more complete is the description of the variability of the initial training set; on the other hand, the larger is  $N$  the more complex becomes the correspondence problem.

Find a meaningful correspondence between shapes is one of the fundamental shape analysis tasks [72]: a good correspondence enables to retrieve the correct information from the training set, because each row of the **TS**, i.e. each variable, refers to a specific location across all the training samples. Assuming that the *family* of shapes under consideration is a linear space of  $\mathbb{R}^{3N}$ , new shapes can be generated by linear combinations of the training samples. Once the dataset **TS** is properly defined, this assumption enables the direct calculation of the mean shape by simply averaging over all  $M$  samples:

$$\bar{\mathbf{x}} = \frac{1}{M} \sum_{i=1}^M \bar{\mathbf{x}}_i \quad (4.4)$$

The covariance matrix **S** is given by:



$$\mathbf{S} = \frac{1}{M-1} \sum_{i=1}^M (\bar{\mathbf{x}}_i - \bar{\mathbf{x}})(\bar{\mathbf{x}}_i - \bar{\mathbf{x}})^T \quad (4.5)$$

Statistically, the *family* of shape is then typically modelled by the multivariate normal distribution  $\mathcal{N}(\bar{\mathbf{x}}, \mathbf{S})$ .

A typical PCA-based approach is usually used to provide an eigendecomposition on  $\mathbf{S}$  delivering the principal *Modes of Variation* (MoVs)  $\varphi_m$  (eigenvectors of the matrix  $\mathbf{S}$ ) and their respective variances  $\lambda_m$  (eigenvalues of the matrix  $\mathbf{S}$ ) estimated on each points  $\mathbf{x}_k$  of the initial dataset  $\mathbf{TS}$ .

PCA returns the plausible deformations, delivered as directions ( $\varphi_m$ ) and related amplitudes ( $\lambda_m$ ) of displacement, of every single point of the mean shape.

It is now possible to approximate new valid shapes, i.e. new individuals again belonging to the same *family* of shapes forming the  $\mathbf{TS}$  matrix, by a linear combination of the first  $c$  MoVs:

$$\mathbf{x} = \bar{\mathbf{x}} + \sum_{m=1}^c \alpha_m \sqrt{\lambda_m} \varphi_m \quad (4.6)$$

Where:

- $\bar{\mathbf{x}}$  is the mean shape as defined in Equation (4.4).
- $\lambda_m$  and  $\varphi_m$  are, respectively, the eigenvalues and eigenvectors resulting from the eigendecomposition, ordered by their variances so that  $\lambda_1 \geq \dots \geq \lambda_{M-1}$ .
- $\boldsymbol{\alpha} \in R^M$  is a coefficient vector that permits to constrain the allowed variation to plausible shape; usually,  $\boldsymbol{\alpha}$  is delimited in the range  $[-3;+3]$ , which corresponds to a deformation that is 3 standard deviations away from the mean ( $\boldsymbol{\alpha} = 0$  means that the model is equal to the mean shape).
- $c$  represents the number of significant eigenvalues. In the presented application,  $c$  is defined so that the accumulated variance (the numerator of Equation 4.7) reaches a certain ratio  $r$  of the total variance (the denominator of Equation 4.7). Common values of  $r$  are between 0.9 and 0.98. Henceforward, in this thesis an  $r$  equal to 0.98 will be considered.

$$\frac{\sum_{i=1}^c \lambda_i}{\sum_{j=1}^{M-1} \lambda_j} = r \quad (4.7)$$

As Equation 4.6 shows, the SSA provides a parametric representation of the considered *family* of shapes; the variance is learned by a finite training set of “meaningful” models. Equation 4.6 represents a mathematically convenient representation of an anatomical healthy ROI, able to generate new consistent shapes simply varying the parameters in the vector  $\boldsymbol{\alpha}$ .

In this application, such a model is used to infer the full shape of the defective model to be restored, predicting the likely healthy shapes from given partial data. The resulting model, named *Posterior Shape Model* (PSM), is attained by exploiting the Bayes’ rule. A comprehensive description on how the PSM has been computed can be found in Section 4.1.2.

Notwithstanding the whole procedure seems straightforward, the establishment of the correspondence (i.e. the identification of the points belonging to different models but located at corresponding position) actually represents a critical step. Point correspondence is a crucial assumption to apply standard multivariate statistics to model a probability distribution over

shapes because, as stated above, it enables a proper data collection and interpretation, starting from the training set. Therefore, the quality of the SSM is heavily influenced by the quality of the established correspondences.

For these reasons, the correspondence problem generally represents the most challenging part in the SSM construction [56].

Since the manual landmarking approach is not suitable when working with complex 3D shape (due to the large amount of points required to achieve an adequate superimposition), several methods for the automatic detection of shape correspondences have been proposed [56]. All the proposed automatic algorithms perform a registration between PDMs: the straightforward solution is to choose an arbitrary shape as reference and warping it to all others by using a non-rigid point set registration. To date, the most established methods to perform such registration are based on Iterative Closest Point (ICP) algorithm [73, 74] or, alternatively, on Coherent Point Drift (CPD) one [75]. The main advantage in using non-rigid point set algorithms is that they treat correspondence as a variable to be estimated and not as an input as in the Procrustes-based algorithms. To overcome the bias introduced by choosing an arbitrary reference shape, the procedure can be repeated a second time with the Mean Shape obtained by the SSM [76] or by applying a symmetric version of the non-rigid registration (as presented in [77] with reference to ICP).

In the specific application of human skull the most established approach based on non-rigid registration [56] proved to be inadequate if brutally applied on the 3D model as it is obtained from the CT data.

Actually, due to the wide anatomical variability and the extreme complexity of the hard tissues in the cranial region, the method often fail to detect the shape correspondences. As an example, Figure 4.1 shows a typical mismatching between the points of the outer and inner crust on a cranial vault model: Figure 4.1 shows the result of a non-rigid pair-wise registration between two healthy adult crania. The mismatching is mainly due to a physiological difference in size of the starting models, which cause incorrect correspondences.



**Figure 4.1: Example of correspondence failure: the mismatching between external (in grey) and internal (in red) surface of the skull.**

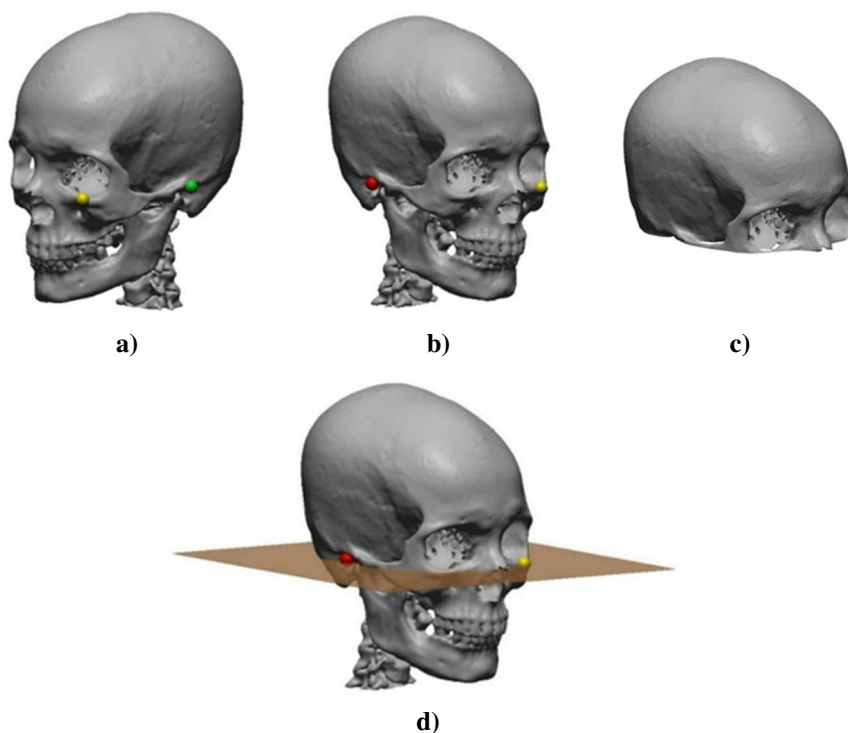
To overcome these drawbacks, in Section 4.1.1 a methodological procedure to compute an SSM using a pair-wise registration based on an automatic detection of shape correspondences is presented. The procedure is designed to obtain a parametric model of the human cranial vault. Being automatic, it makes possible to easily enlarge the number of samples in the

Training Set, consequently increasing the variability of the parametric model and therefore its accuracy

#### 4.1.1. *Statistical Shape Modelling: a reliable and robust procedure for neurocrania*

The procedure starts from a number of PDMs representing pathologically unaffected cranial vault. Instead of PDMs, STL files can be provided as input. STL files can be easily obtained directly from the segmentation process, as explained in Section 3.1.2.

To facilitate the subsequent operations, each model is roughly finished removing outliers and redundant regions.



**Figure 4.2:** a – b) The selection of Left Orbital (yellow) and both the Porions (green and red) landmarks; c) The isolated neurocranium; d) The Frankfurt Plane passing through the three landmarks

The neurocranium is isolated by cutting each STL with its *Frankfurt Plane* (FP) (Figure 4.2(c)). The FP is an anatomical plane passing through the anatomical landmarks *Left Orbital*, and both the *Porions*; these landmarks are manually selected on each model (Figure 4.2).

No further operations are required. In the following, the proposed procedure is described step by step. The flow chart of the proposed procedure is presented in Figure 4.3.

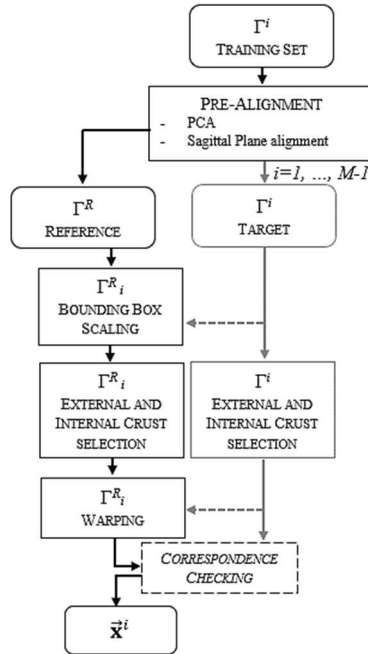


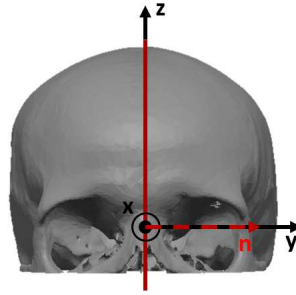
Figure 4.3: The flow chart of the proposed procedure to build the SSM

### Alignment and Scaling

To ensure a well-defined correspondence, the proposed procedure uses a pair-wise approach to deform a reference shape (henceforward called Reference) onto each other sample (henceforward called Target) contained in the Training Set. Such a deformation is achieved by means of a non-rigid registration algorithm based on an Iterative Closest Point (ICP) algorithm, as described in detail in [64]. It is worth to note that also an alternative registration method (i.e. the Coherent Drift Points) have been tested, but the ICP-based method has proved, in this application, to be able to provide better results as well as to require a lower computational cost as the number of points used to represent each model increases (see Section 4.1.3 for further information about the comparison between the two registration methods).

By using the ICP-based approach, the optimal non-rigid transformations to match the Reference to each Target are found, notwithstanding Reference and Targets are STLs with different number of points. This way, a new Training Set is defined, that still describes the same variance of the initial population but containing instances with the same number of points  $N$ , since they are represented by the Reference properly deformed onto each Target.

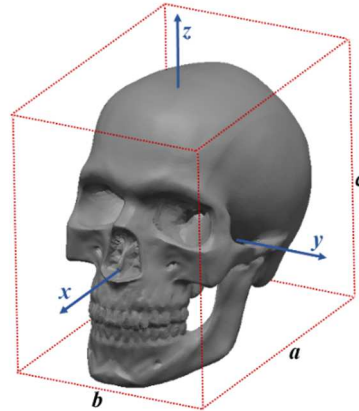
Among the existing approaches, the algorithm proposed in [64] has proved to be reliable in our application as long as the point correspondence is correctly fulfilled; but, as said in Section 4.1, the direct application of a non-rigid pair-wise registration to complex shapes almost certainly leads to questionable results (Figure 4.1). To overcome this shortcoming and to make the procedure more reliable, a different pre-alignment between the Reference and each Target is performed before the application of the ICP.



**Figure 4.4: The initial alignment**

First, a rough alignment is performed by representing each training sample in its Principal Component Space: it means that each shape is translated to superimpose its centroid onto the origin of the global reference system and rotated to align its principal axes of inertia with the  $x$ -,  $y$ - and  $z$ - axis of the global reference system.

To refine the alignment, the sagittal plane of each skull (calculated by the algorithm presented in Section 4.2) is aligned with the  $y$ -plane (i.e. the plane orthonormal to the  $y$  vector). As a result, all the samples are aligned as shown in Figure 4.4.



**Figure 4.5: The coordinate frame of the pre-aligned Training Set. The centroid of each model is superimposed to the origin of the axes. The red dotted line represents the Bounding Box of the sample. The dimension  $a$ ,  $b$  and  $c$  are defined as reported.**

In addition, a new Reference model is created as follows: for each Target  $i$  the original Reference is scaled in the three dimensions  $a$ ,  $b$  and  $c$  (defined as shown in Figure 4.5) by values equal to  $s_a^i$ ,  $s_b^i$  and  $s_c^i$ . The  $s$  values are calculated as in Equation 4.8:

$$s_{\xi}^i = \frac{\xi_{BB}^i}{\xi_{BB}^R}, \quad i = 1, \dots, M - 1 \quad (4.8)$$

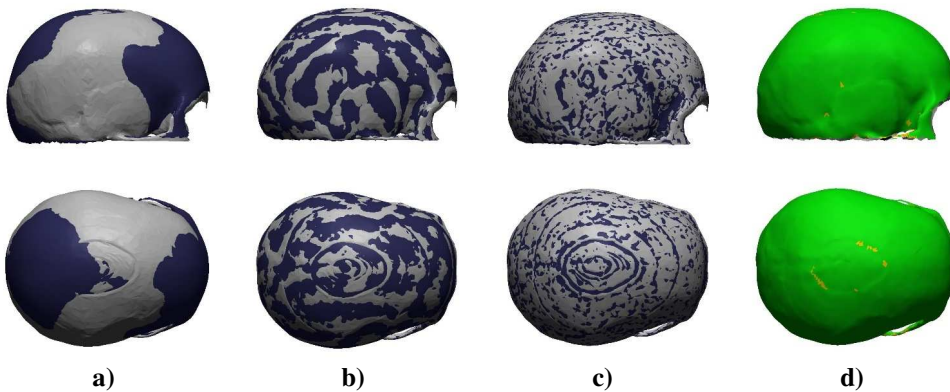
where  $\xi_{BB}$  indicates the dimension  $a$ ,  $b$  or  $c$  of the Bounding Box (red dotted line in Figure 4.5) of the shape indicated by the superscript index, i.e.  $i$  for the considered Target and  $R$  for the original Reference. As a result, the dimensions of the Bounding Box of each deformed Reference  $i$  is equal to the Bounding Box of the corresponding Target  $i$ .

### *Selection of the External and Internal crust*

The previous steps ensure a consistent orientation of the shapes which are now aligned in a common coordinate frame. Despite that, this is not still sufficient to ensure a reliable point-to-point matching during the subsequent ICP- based registration algorithm because of the high complexity and high variability of the population data. To reduce the possibility of mismatching, the internal and external crusts of each cranial vault are automatically isolated using a ray-tracing algorithm [78] as explained in [79]. The aim is to apply the ICP separately to the two crusts by treating them as different surfaces. This way, the data sets to be matched are much simpler than the complete model. The two parts will be re-merged after establishing the correspondence, and the SSM will be computed on the complete neurocranium.

### *Non-Rigid registration*

Non-rigid ICP algorithm described in [64] has been implemented to warp the external and internal crust of the scaled Reference  $i$  onto, respectively, the external and internal crust of each Target  $i$ . This algorithm performs an initial rigid alignment carried out by a bidirectional ICP algorithm [73], that also delivers the correspondence between the scaled Reference and the considered Target, followed by a non-rigid transformation modelled as a sum of Gaussian Radial Basis Function [80].



**Figure 4.6:** a – c) Three subsequent steps of the non-rigid registration between the Reference (deformable, in blue) and the Target (fixed, in grey); d) color maps of the mesh deviation between the Target and the resulting template: green<math><0.1\text{mm}</math>, yellow<math><0.3\text{mm}</math>.

Applying this algorithm on the training set modified as described above allows to obtain an adequate warping (Figure 4.6). A comprehensive evaluation of the effectiveness of the registration process will be given in Section 4.1.3.

As a result, a new training set is generated; Targets are now represented by the properly deformed Reference. As said, this new training set still contains the same variance of the initial population, but the data are organized for the creation of the SSM.

As said above, the ICP-based algorithm has proved to deliver better results if compared with alternative methods: in Section 4.1.3 an SSM built with the presented approach is

compared to a second SSM built replacing the ICP with the CPD, that represents the most established alternative suitable for this application found in literature.

### Correspondence

Having regard to its importance throughout the procedure, a further check is made to ensure that correspondences have been correctly defined. Given the vectors:

- $\mathbf{x}^i$  containing the points' coordinate of the new Target  $i$ , and
- $\mathbf{x}^R$  containing the points' coordinate of the Reference,

a  $k$ -Nearest Neighbor ( $k$ -NN) algorithms is iteratively applied to finds the nearest neighbor (i.e. the closest point) in  $\mathbf{x}^i$  for each query point in  $\mathbf{x}^R$ . So,  $k$  is imposed equal to 1. Then, each Target vector  $\mathbf{x}^i$  is sorted so that the  $j$ -th point is the nearest local neighbor of the  $j$ -th point of the Reference.

To avoid double assignments (i.e. more than one  $\mathbf{x}_j^i$  defined as local neighbor of the same  $\mathbf{x}_j^R$ ), the Target's points already assigned are removed from the list of possible subsequent matches. For each Target, the algorithm is iteratively applied as long as  $d_c$ , i.e. the median of the Euclidean distances calculated between the points in correspondence of the two considered PDMs, converges (Equation 4.9).

$$d_c = \text{median} \left( \sum_{j=1}^N \text{dist}(x_j^R, x_j^i) \right), i = 1, \dots, M - 1 \quad (4.9)$$

The median is considered instead of the mean because, this way,  $d_c$  is more robust to outliers.

After the data have been sorted properly to fulfil the correspondence, the internal and external crust of both Reference and Targets are re-merged as a single model to create the **TS** dataset (as described in Equation 4.3). The SSM of the cranial vault can be then computed starting from the just created **TS** matrix.

Figure 4.7 schematically resumes the flow chart of the correspondence checking.

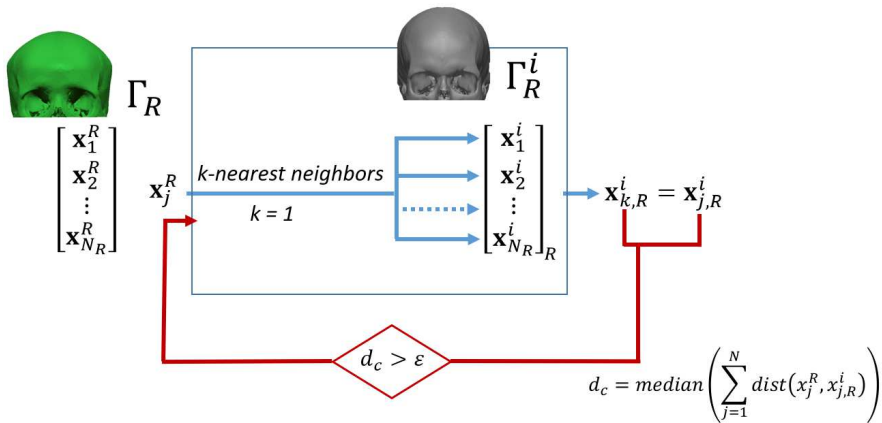


Figure 4.7: Correspondence checking

### Generalized Procrustes Analysis: final alignment

The obtained correspondence can be used as input for the final alignment of the training samples  $\Gamma_R^i$ , performed by means of the *Procrustes Analysis* (PA) [81 – 84]. PA exploit the knowledge of pairwise correspondence to superimpose two or more samples with the aim to provide the transformations that maps one point set to the other.

The *Procrustes* superimposition is performed by removing the information related with the translations, rotations and, optionally, scaling. The aim of the *Procrustes* superimposition is to minimize a measure of shape difference, usually referred to as *Procrustes Distance*. The PA is called *full* or *partial* depending if the scaling is, respectively, performed or not performed. As said in Section 3.1.1, in this application, as usual in biology, the scale is maintained because it represents a morphologic meaningful information.

An essential requirement for applying a PA on PDMs is that the landmarks on all the training samples are located in the corresponding position: in other word, PA strictly requires shapes with well-defined correspondences.

Considering a collection of training samples defined as in Equation 4.1, the classical PA, named *Ordinary Procrustes Analysis* (OPA), aligns each sample to a reference arbitrarily chosen among the training samples [81, 82]. To avoid the possible biases that could be introduced by arbitrarily choosing the reference shape [56], in this application the *Generalized Procrustes Analysis* (GPA) [84] is used instead of the OPA: the GPA seeks the transformations (here, rotations and translations) to be applied to each sample in order to find the optimal superimposition, considering as reference the mean shape calculated among all the registered samples.

The mean shape of the registered samples is obviously unknown at first, so the GPA starts from an estimation  $\bar{\mathbf{X}}$  (Equation 4.10) equal to a chosen sample, as in the OPA. After a first run, the mean shape is computed among the resulting registered shapes; if the *Procrustes distance* between the new mean and the previous reference shape is above a given threshold, the GPA is performed again setting the new mean as reference shape  $\bar{\mathbf{X}}$ . The method runs iteratively until the reference and the new mean are above the threshold.

Considering the correspondence requirement correctly fulfilled among the shapes  $\mathbf{x}$  (defined as in Equation 4.1) and considering the *Euclidean Distance* between corresponding points as *Procrustes Distance*, the full GPA can be defined as:

$$\begin{aligned} \begin{bmatrix} (\hat{\beta}_1, \dots, \hat{\beta}_M) \\ (\hat{\varphi}_1, \dots, \hat{\varphi}_M) \\ (\hat{\gamma}_1, \dots, \hat{\gamma}_M) \end{bmatrix} &= \underset{\substack{\hat{\beta}_1, \dots, \hat{\beta}_M \\ \hat{\varphi}_1, \dots, \hat{\varphi}_M \\ \hat{\gamma}_1, \dots, \hat{\gamma}_M}}{\operatorname{argmin}} \frac{1}{M} \sum_{i=1}^M \sum_{j=i+1}^M \|(\beta_i \mathbf{x}^i \varphi_i + 1_n \gamma_i^T) - (\beta_j \mathbf{x}^j \varphi_j + 1_n \gamma_j^T)\|^2 \\ &= \sum_{j=1}^M \|(\beta_i \mathbf{x}^i \varphi_i + 1_n \gamma_i^T) - \bar{\mathbf{X}}\|^2 \end{aligned} \quad (4.10)$$

Where  $\beta_i$ ,  $\varphi_i$  and  $\gamma_i$  represent, respectively, scale factors, rotations and translations to be applied to each  $i$ -th shape in order to obtain the optimal superimposition among all shapes. As said above, in this application a partial GPA is considered, and only  $\varphi_i$  and  $\gamma_i$  are computed.

GPA is largely used to superimpose a set of objects, being able to define an optimal reference orientation for the samples, while in the OPA the orientation must be arbitrarily selected.



The GPA is here applied to the shapes  $\Gamma_R^i$ ; as a result, the method provides the set of samples adequately arranged to be collected in the **TS** matrix by stacking properly the coordinates of each registered  $\Gamma_R^i$  (see Equation 4.2 and Equation 4.3).

### PCA

The previous subsections have presented a robust methodology to properly rearrange the initial training dataset formed by an adequate number of representative models belonging to a given *family* of shapes; the aim is to build a matrix **TS** which describes the same variability of the initial training set, but properly shaped to enable a correct application of the PCA on the data.

In the actual implementation of the PCA, the calculation of the eigenvectors  $\varphi_m$  and the eigenvalues  $\lambda_m$  is usually performed by a *Singular Value Decomposition* (SVD) [85, 86] on the mean-centered dataset matrix **L** instead of using the eigenanalysis on the covariance matrix **S** defined in Equation 4.5. **L** is obtained by mean-centering the matrix **TS** (Equation 4.11), i.e. by subtracting the variable averages from the data in **TS**.

$$\mathbf{L} = ((\bar{\mathbf{x}}^1 - \bar{\mathbf{x}}), \dots, (\bar{\mathbf{x}}^M - \bar{\mathbf{x}})) \quad (4.11)$$

The SVD performed on **L** delivers the same results of the eigendecomposition applied on **S**, but it is preferable because it ensures a higher numerical stability [56].

By performing the PCA to the defined **TS**, the first  $c$  (see Section 4.1) significant MoVs with the respective variances are delivered; based on our definition of  $c$ , they provide the 98% of the total variance of all the instances contained in **TS**.

Figures 4.8 – 4.10 describe the first three MoVs of the exocranial surface as resulting applying the SSA to the training set under consideration in this thesis; the figures show the maximum and minimum deformation according, respectively,  $\varphi_1$ ,  $\varphi_2$  and  $\varphi_3$  with respect to the mean shape.

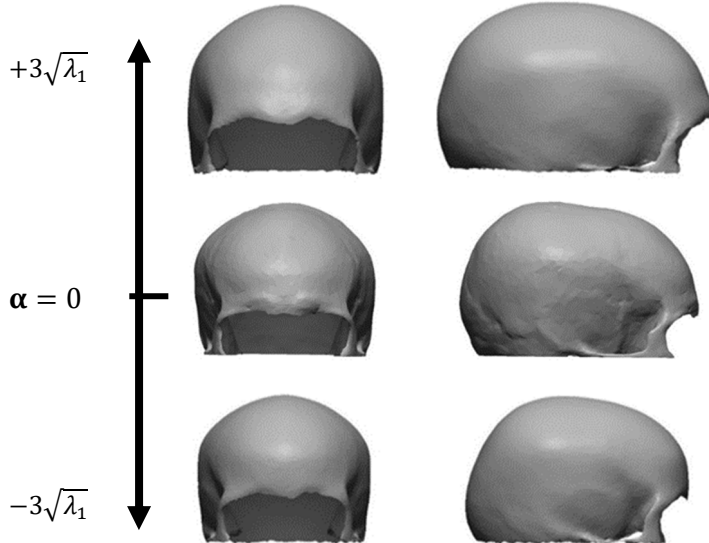
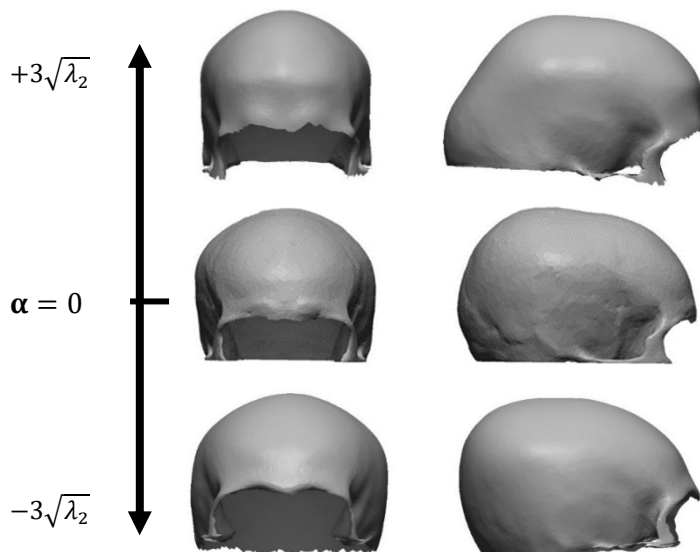
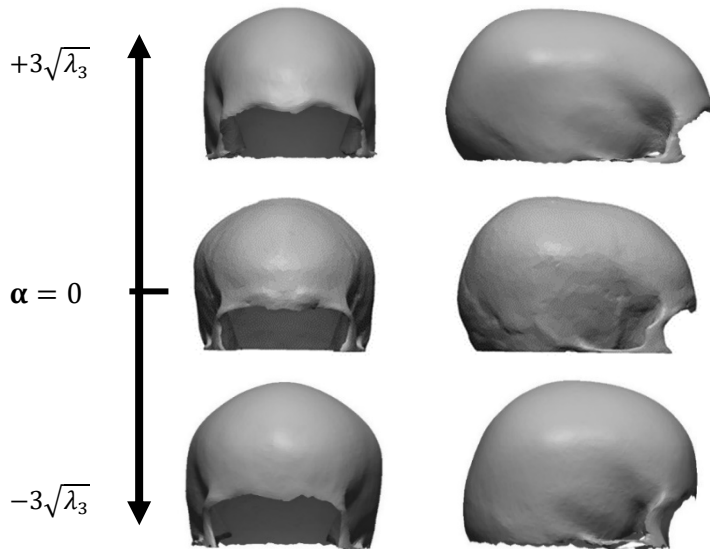


Figure 4.8: The first MoV



**Figure 4.9: The second MoV**



**Figure 4.10: The third MoV**

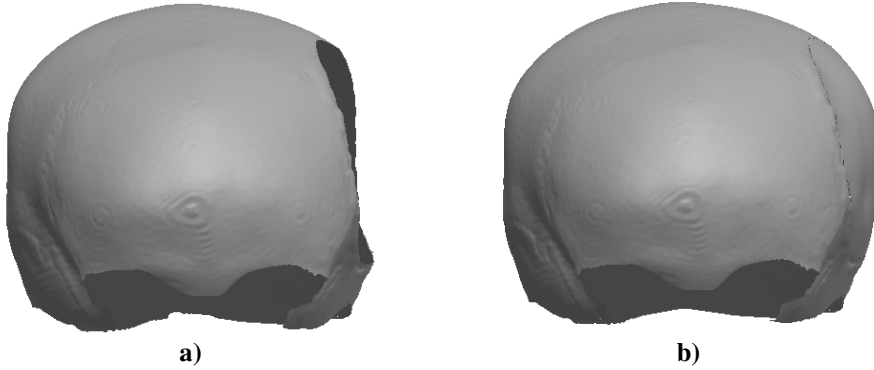
### **SSM**

At this stage, it is possible to define the statistical model learned from the initial training set by introducing in Equation 4.6 the mean shape obtained applying the Equation 4.4 among the instances contained in the **TS**, and the MoVs with their respective variance obtained by means of the PCA. As said presenting the SSM in Section 4.1, by using Equation 4.6 it is

possible to generate a new consistent shape just defining a vector of parameters  $\alpha \in R^M$ ; usually,  $\alpha$  is delimited in the range  $[-3;+3]$  to constrain the maximum displacement value along each MoV of each point of the mean  $\bar{\mathbf{x}}$  to three times its standard deviation: this ensures to obtain only “plausible” shapes.

#### 4.1.2. Posterior Shape Models

In addition to the ability to generate new consistent shapes based on a set of representative training samples, SSMs have also been used to infer the full shape from partial data exploiting the concepts of Bayes’ rule: if a region of the solution shape is partially known, it can be used as a prior knowledge to restrict the solution space. This approach leads to a *posterior distribution*, that describes the probability distribution of the unknown quantity conditional on the known evidence (Figure 4.11).



**Figure 4.11: The prior model (a) constrains the possible shapes of the posterior model (b)**

This can be done by computing the conditional distribution  $p(\mathbf{x}|\mathbf{x}_g)$  (i.e. the likelihood of event  $\mathbf{x}$  occurring given that  $\mathbf{x}_g$  is true) of the SSM  $\mathbf{x}$  given the partial data  $\mathbf{x}_g$ . The aim is to generate the most likely shape by conditioning the statistical model on the a priori known region. The result is a *Posterior Shape Model* (PSM), a new statistical model which is again an SSM (i.e. a parametric model that represent a *family* of shapes) with the same form described in Equation 4.6.

When a neurocranium restoration is faced, only a part of the shape is missing or deformed, while the remaining is known. So, the PSM can be used to exploit this prior knowledge and find the most likely shape of the missing part. In the presented application, the PSM is then used to define the template required to retrieve the MPs in case of non-unilateral defects, as described in Section 3.2.3.

Following the mathematical framework presented in [87], the SSM defined in Equation 4.6 can be represented in matrix form as:

$$\mathbf{x} = \mathbf{x}(\alpha) = \bar{\mathbf{x}} + \mathbf{UD}\alpha = \bar{\mathbf{x}} + \mathbf{Q}\alpha \quad (4.12)$$

Where  $\mathbf{U} = (\varphi_1, \dots, \varphi_M)$  and  $\mathbf{D} = (\sqrt{\lambda_1}, \dots, \sqrt{\lambda_M})$  are the matrices that contain, respectively, the eigenvectors and the eigenvalues of the covariance matrix  $\mathbf{S}$  as defined in

Equation 4.5. With this notation, the multivariate normal distribution that models the *family* of shapes can be written as  $\mathcal{N}(\bar{\mathbf{x}}, \mathbf{U}\mathbf{D}^2\mathbf{U}^T)$ .

Since the SSM relies on the consistent choice of the parameters  $\boldsymbol{\alpha}$  to create a new shape (see Section 4.1), the definition of the PSM (useful to predict the shape of the missing or deformed region of the model to be corrected) is reduced to the computation of the correct parameters  $\boldsymbol{\alpha}$ . By assuming that  $p(\boldsymbol{\alpha}) \sim \mathcal{N}(\mathbf{0}, \mathbf{I}_M)$ , i.e. the coefficients  $\boldsymbol{\alpha} \in \mathbb{R}^M$  follow a standard normal distribution whose mean is 0 and its covariance is the  $M$ -dimensional identity matrix, a probability distribution  $p(\mathbf{s}) \sim \mathcal{N}(\bar{\mathbf{x}}, \mathbf{Q}\mathbf{Q}^T)$  is induced on the shape space, i.e. the space of the possible shape configurations.

The information available (namely the locations of the known points describing the model to be reconstructed) is given in form of  $q < 3N$  entries. These entries are henceforward denoted as  $\mathbf{x}_g \in \mathbb{R}^q$ . Related to the data  $\mathbf{x}_g$ , the sub-vector  $\bar{\mathbf{x}}_g \in \mathbb{R}^q$  and sub-matrix  $\mathbf{Q}_g \in \mathbb{R}^{q \times M}$  can be defined by selecting the rows corresponding to the given entries from the full model's  $\bar{\mathbf{x}}$  and  $\mathbf{Q}$ . In order to select the appropriate sub-vector  $\bar{\mathbf{x}}_g$  and sub-matrix  $\mathbf{Q}_g$ , the given points need to be in correspondence with the training samples in  $\mathbf{TS}$ : it is necessary to know which entries in  $\mathbf{x}_g$  correspond to which entries in  $\mathbf{x}$  in order to select the correct rows from  $\bar{\mathbf{x}}$  and  $\mathbf{Q}$ .

Once the a priori knowledge has been effectively defined and according to the Bayes' rule, the conditional distribution  $p(\boldsymbol{\alpha}|\mathbf{x}_g) \sim \mathcal{N}(\boldsymbol{\eta}, \boldsymbol{\Lambda})$  can be computed:  $p(\boldsymbol{\alpha}|\mathbf{x}_g)$  is again a multivariate normal distribution which restricts the choice of the parameters  $\boldsymbol{\alpha}$  by imposing the a priori knowledge  $\mathbf{x}_g$ .

Since in the discussed application the number of training samples  $M$  is always less than the dimensionality  $3N$  of the shape space (typically  $M$  is in the hundreds while  $N$  is in the thousands), the resulting normal distribution  $\mathcal{N}(\bar{\mathbf{x}}, \mathbf{Q}\mathbf{Q}^T)$  is singular because the covariance matrix  $\mathbf{Q}\mathbf{Q}^T$  does not have full rank. As a consequence, it is not possible to directly compute the conditional distribution  $p(\boldsymbol{\alpha}|\mathbf{x}_g)$ , because, being singular, it is not able to defines a valid probability distribution on the space  $\mathbb{R}^{3N}$  of all possible shape deformations. In other words, if  $M < 3N$ , the probability density function of  $\mathcal{N}(\bar{\mathbf{x}}, \mathbf{Q}\mathbf{Q}^T)$  assigns a value of 0 to a shape that do not exactly lie in the span of the training set, even though it is very close to one of the training samples. This results in a poor ability to recognize a shape belonging to the same *family*, but that also varies little compared to the training samples; so, it is not generally possible to use the singular distribution  $\mathcal{N}(\bar{\mathbf{x}}, \mathbf{Q}\mathbf{Q}^T)$  or rather  $\mathcal{N}(\bar{\mathbf{x}}_g, \mathbf{Q}_g\mathbf{Q}_g^T)$  to directly interpret given data.

As a consequence, since the model to be reconstructed does not lie in the span of the training set, the statistical model applied to the partial data lead to an approximation of the  $\mathbf{x}_g$ .

A standard approach [87, 88] to overcome this shortcoming and to compute such conditional distribution, involves the regularization of the  $\mathbf{Q}_g\mathbf{Q}_g^T$  (i.e. the part of the covariance matrix corresponding to the given data) by adding a small noise  $\varepsilon$  to the partial data. This noise can be represented by a parameter  $\sigma^2$  that multiplies the identity matrix  $\mathbf{I}$ :

$$\varepsilon = \sigma^2 \mathbf{I}_M \quad (4.13)$$

Therefore, the resulting statistical model still assigns a high probability to shapes that are in or near the span of the training samples, but is also able to give a low, but greater than 0, probability to shapes further away.

It is thus modelled the distance of the data set  $\mathbf{x}_g$  from the model space (learned from the training samples) by means of a noise variable  $\varepsilon \sim \mathcal{N}(\mathbf{0}, \sigma^2 \mathbf{I}_q)$ , considering a small variance

of  $\sigma^2$ . So, the parameters  $\sigma^2$  models the deviation of the given data  $\mathbf{x}_g$  from the shapes that the parametric model can describe. An established formulation of  $\sigma^2$  is [87]:

$$\sigma^2 = \frac{1}{q} \|\mathbf{x}_g - \hat{\mathbf{x}}_g\|_2^2 \quad (4.14)$$

where  $\hat{\mathbf{x}}_g$  represents the best approximation of  $\mathbf{x}_g$  modelled by the statistical model:

$$\hat{\mathbf{x}}_g = \bar{\mathbf{x}}_g + \mathbf{Q}_g \boldsymbol{\alpha} \quad (4.15)$$

Once the noise  $\varepsilon$  has been computed, the given data can be described as:

$$\mathbf{x}_g = \bar{\mathbf{x}}_g + \mathbf{Q}_g \boldsymbol{\alpha} + \varepsilon \quad (4.16)$$

Actually, Equation 4.16 describes a non-singular distribution on the space  $\mathbb{R}^q$  of all partial data  $\mathbf{x}_g$ . Since it is non-singular, the conditional distribution  $p(\boldsymbol{\alpha}|\mathbf{x}_g)$  of the model parameters  $\boldsymbol{\alpha}$ , given the partial information  $\mathbf{x}_g$  can be computed with standard methods.

Because the definition of the parameters  $\boldsymbol{\alpha}$  naturally means the definition of a new full shape  $\mathbf{x}(\boldsymbol{\alpha})$ , the  $p(\boldsymbol{\alpha}|\mathbf{x}_g)$  also defines the conditional distribution  $p(\mathbf{x}|\mathbf{x}_g)$  of the full shapes given the partial data.

It is worth to note that, since the distribution of the parameters  $\boldsymbol{\alpha}$  and the conditional distribution  $p(\mathbf{x}_g|\boldsymbol{\alpha})$  are both normal, the conditional distribution  $p(\boldsymbol{\alpha}|\mathbf{x}_g)$  is again a multivariate normal distribution: that entails that it can be calculated using Bayes' rule [89]:

$$p(\boldsymbol{\alpha}|\mathbf{x}_g) = \mathcal{N}(\mathbf{M}^{-1}\mathbf{Q}_g^T(\mathbf{x}_g - \bar{\mathbf{x}}_g), \sigma^2 \mathbf{M}^{-1}) =: \mathcal{N}(\boldsymbol{\eta}, \boldsymbol{\Lambda}) \quad (4.17)$$

Where:

$$\mathbf{M} = \mathbf{Q}_g^T \mathbf{Q}_g + \sigma^2 \mathbf{I}_M \quad (4.18)$$

It is now possible to calculate the mean and the covariance matrix of the posterior distribution of the full shape  $\mathbf{x}$ :

$$p(\mathbf{x}|\mathbf{x}_g) = \mathcal{N}(\bar{\mathbf{x}} + \mathbf{Q}\boldsymbol{\eta}, \mathbf{Q}\boldsymbol{\Lambda}\mathbf{Q}^T) =: \mathcal{N}(\bar{\mathbf{x}}_c, \mathbf{S}_c) \quad (4.19)$$

The Equation 4.19 is by all means an SSM, whose explicit representation of the mean  $\bar{\mathbf{x}}_c$  is:

$$\bar{\mathbf{x}}_c = \bar{\mathbf{x}} + \mathbf{Q}(\mathbf{Q}_g^T \mathbf{Q}_g + \sigma^2 \mathbf{I}_M)^{-1} \mathbf{Q}_g^T (\mathbf{x}_g - \bar{\mathbf{x}}_g) \quad (4.20)$$

And its covariance is equal to:

$$\mathbf{S}_c = \sigma^2 \mathbf{Q}(\mathbf{Q}_g^T \mathbf{Q}_g + \sigma^2 \mathbf{I}_M)^{-1} \mathbf{Q}^T \quad (4.21)$$

In this thesis, we are interested in the only posterior mean  $\bar{\mathbf{x}}_c$  because it represents the most likely (complete) shape, once given the partial data [87, 90]: so, in this application, it represents the most likely healthy cranial vault reproducing the healthy known bone.  $\bar{\mathbf{x}}_c$  is, then, the template useful for the shape prediction of the missing or deformed part to be restored on the defective skull under consideration.

The computation of the posterior mean  $\bar{\mathbf{x}}_c$  can be easily included in the procedure presented in the previous sections, as they share the same mathematical framework: in this regard, this section has explained how to build matrices  $\mathbf{Q}$  and  $\mathbf{Q}_g$ , as well as how to compute the mean  $\bar{\mathbf{x}}_g$  and the noise  $\varepsilon$ . All of them can be easily attained from the data obtained performing the PCA on the dataset matrix  $\mathbf{TS}$ .

### 4.1.3. Assessment of the proposed procedure for the SSM construction

The procedure presented in Section 4.1.1 and in Section 4.1.2 to obtain the parametric model and to calculate the PSM from known given data has been implemented in Matlab® (MathWorks, Inc.); then, the algorithm has been used to compute the statistical model based on an initial training set containing 100 STL models of pathologically unaffected adult crania (43 females, 57 males, average age= 48.08 years). The STL models have been obtained from anonymized CT diagnostic images using specifically designed tools in Materialise Mimics® software (Materialise NV, Leuven, Belgium) for image segmentation and for exporting the STL model.

To facilitate the following operations, each of the so obtained STL models are roughly finished (removal of outliers and redundant regions). In order to maintain the calculation cost limited, the number of points of each training neurocranium is decimated up to about 10000-15000 points.

As a result, the developed algorithm automatically provides the matrix **TS** (as defined in Equation 4.3) and the parametric representation of the SSMs (Equation 4.6). As explained in Section 4.1.2, **TS** and the parametric model can be also used to restore an incomplete shape given the known parts of the shape itself: in this case, the algorithm automatically provides also the most likely PSM by taking as input the coordinates of the known points of the shape to be reconstructed.

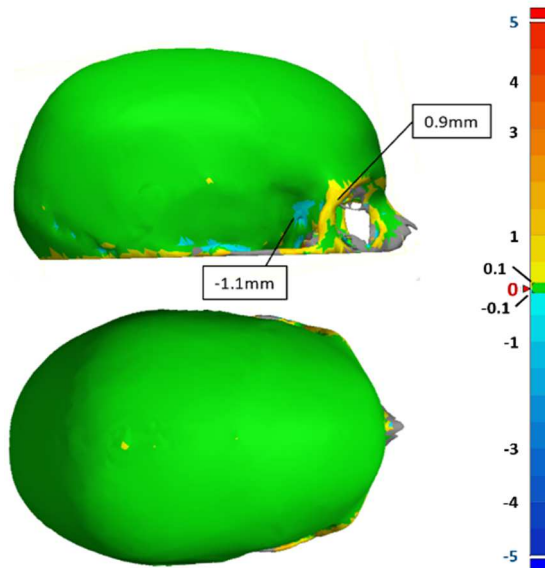
For the purpose of this thesis, the PSM undoubtedly represents the most relevant result, because it delivers the external source useful as template to define the MPs (see Section 3.2.3); but, in the related literature, there are no well-established tools designed for assessing the quality of the PSM, while there are many to evaluate the quality of the SSM [56, 91]. For this reason, in this Section, the performance of the developed algorithm has been evaluated on the quality of the provided SSM instead of on the PSM, directly. However, the evaluation of the SSM also provides a meaningful assessment of the PSM since the quality of the PSM is strictly related to the one of the SSM.

In addition, for a comprehensive assessment of the effectiveness of the delivered results, the following paragraph reports also an evaluation of the quality of the **TS** matrix and, consequently, of the quality of the correspondences established among the training samples.

The ability of the algorithm to deliver an effective PSM (i.e. useful to provide a reliable approximation of the missing shape) will be investigated in Chapter 5, after defining a quantitative methodology able to measure the quality of such approximation.

#### *Evaluation of the matrix TS*

To evaluate the registration process and the establishment of the correspondences, each model of the **TS** was compared with the corresponding cranial vault contained in the initial training set. The comparison is carried out by a deviation analysis between corresponding models (i.e. the deformed Reference and the correspondent Target). Figure 4.12 shows an example of the deviation measured between two corresponding samples.



**Figure 4.12: Deviation (in mm) between the deformed Reference  $\Gamma_R^i$  and the Target  $\Gamma^i$**

Considering all the comparisons, the results showed a deviation in the range of  $-0.5 \div 0.5$  mm, with the exception of few small areas characterized by high curvature and high shape complexity where the correspondence is still not reliable, and the deviation increases to values between  $-2$  and  $2$  mm. This error is however limited and, as said, relegated to small areas.

Furthermore, no model in the **TS** has showed inaccurate geometry, in contrast with the outcomes obtained without pre-processing the data according the procedure presented in this thesis (see Section 4.1 and Figure 4.1).

These results are, then, fully acceptable: they prove the ability of the proposed procedure to transform the data into a suitable form for the subsequent analysis, providing a set of shapes in correspondence which properly represent the ones contained in the initial training set.

For a further evaluation of the registration process based on the ICP-method, its performance is compared with the most established alternative proposed in literature, that is represented by the Coherent Drift Point (CPD) [75]. CPD has been developed to overcome the principal downside of the ICP that requires that the two sets of points to be registered have to be as close as possible.

CPD is a probabilistic method for non-rigid registration of point sets. The registration is treated as a *Maximum Likelihood* (ML) estimation problem with motion coherence constraint over the velocity field such that one points-set moves coherently to align with the second points-set. Further information about the CPD can be found in [75].

To perform this evaluation, two different **TS** are built using respectively the ICP-based registration and CPD-based registration. In the latter, the CPD algorithm is used instead of the ICP, while all the other steps and tools are maintained as described in the related sections. Then, two different SSMs are provided by performing an SSA on the two **TS** matrices.

In the following paragraph, the evaluation of the resulting SSMs (obtained applying the two registration methods) has been reported: the results (Figures 4.16 – 4.18) show that the

SSM obtained with the ICP-based registration is better than the SSM provided by the CPD. The evaluation is performed according to the evaluation method proposed by [91] and described in detail below.

### *Evaluation of the SSM*

The most established approach for the SSM quality assessment is based on the work published by Davies in 2002. In [91], the author proposed a methodological procedure to evaluate the general quality of an SSM identifying the properties that would be ideally required for such a model: the *Generalization ability*, the *Specificity* and the *Compactness* [91].

The initial aim of the author was to compare different models constructed starting from the same training set rather than to propose an absolute measure of the quality of an SSM. So, to provide a more significant and objective evaluation of the quality of an SSM, over the years, many authors [56, 92–95] have proposed alternative approaches, especially for the calculation of the *Generalization ability* and the *Specificity*, that heavily depends on the metric  $\mathcal{D}$  used to compare different shapes (see Equation 4.22 and Equation 4.23).

However, over the years only the way of measuring the three parameters presented by Davies has changed, while the concepts underlying the evaluation approach have proved to be very robust.

In the following, an exhaustive description of the three properties will be provided, and the approach followed in this application to calculate each of them is described and justified.

Regarding the first property, the *Generalization ability*  $\mathcal{G}$  quantifies the capability of the model to reproduce a given model; in other words,  $\mathcal{G}$  measures the ability of the model to learn the characteristics of the *family* of shapes under consideration from a limited training set. It is estimated by performing a series of leave-one-out tests on the training set, measuring the distance of the omitted training shape  $\Gamma^i$  to the closest match of the reduced model  $\Gamma_*^i(c)$ .

The *Generalization ability* is provided as a function of the number  $c$  of the significant eigenvalues used to define the parametric model in Equation 4.6 (see Section 4.1 and Equation 4.7 for the definition of  $c$ ):

$$\mathcal{G}(c) = \frac{1}{M} \sum_{i=1}^M \mathcal{D}(\Gamma_*^i(c), \Gamma^i) \quad (4.22)$$

Lower values of  $\mathcal{G}$  indicates better SSMs.

$\mathcal{D}$  represent the metric used to compute the distance between the shapes: by varying  $\mathcal{D}$ , the significance of the difference changes. In this thesis, according to the approach presented in [93], the *Symmetric Mean* (SM) distance calculated between the nearest points is used as the metric  $\mathcal{D}$  (see [93] for further information). Using the SM calculated between the nearest points instead of exploiting the pairwise correspondences ensures to exclude from the evaluation any aspect regarding the registration process providing only a sensitive appraisal of the model ability to match a given shape.

This approach also considers a normalization with respect to the  $N$  (i.e. the number of the points of  $\Gamma_*^i$  and  $\Gamma^i$ ). This way,  $\mathcal{G}$  value is not just an index for direct comparison with other SSMs but represents also a measure of the fitting error (in *mm*) between a target shape and its closest SSM.

Consequently, using such an approach and considering an adequate number of leave-one-out tests,  $\mathcal{G}$  can be interpreted as an estimate of the expected fitting error (in *mm*) of the statistical model under consideration.



The second measure to evaluate an SSM is the *Specificity*  $\mathcal{S}$  that describes the model's ability to generate new consistent shapes, i.e. shapes belonging to the *family* of shapes under consideration. The measure is estimated by generating random parameters  $\mathbf{a}$  from a normal distribution defined, as usual, as  $p(\mathbf{a}) \sim \mathcal{N}(\mathbf{0}, \mathbf{I}_M)$ . The distance of the generated shape to the closest match of the training set is then averaged over a large number of runs  $n$ . As the *Generalization ability*, the *Specificity* is provided as a function of the number  $c$  of the significant eigenvalues:

$$\mathcal{S}(c) = \frac{1}{n} \sum_{k=1}^n \min_{\{i=1, \dots, M\}} \mathcal{D}(\Gamma_*^k(c), \Gamma^i) \quad (4.23)$$

For the *Specificity*, the metric  $\mathcal{D}$  used in this thesis is the *Mean Absolute Distance* (MAD) between corresponding points to make the measurement robust and independent from the number of landmarks [92]. As for the  $\mathcal{G}$ , lower values of  $\mathcal{S}$  indicates better SSMs.

The last measure is the *Compactness*  $\mathcal{C}$ , that simply represents the cumulative variance of the model as calculated with the PCA. In this thesis, the  $\mathcal{C}$  value is normalized with the total variance  $\sum_{j=1}^{M-1} \lambda_j$ :

$$\mathcal{C}(c) = \frac{\sum_{i=1}^c \lambda_i}{\sum_{j=1}^{M-1} \lambda_j} \quad (4.24)$$

A compact model (i.e. small value of  $\mathcal{C}$ ) requires few parameters to define a new shape. So, contrarily to the two previous measures, higher values of  $\mathcal{C}$  indicates better SSMs.

The just-defined values of  $\mathcal{G}(c)$ ,  $\mathcal{S}(c)$  and  $\mathcal{C}(c)$  for the constructed SSM have been computed and reported in the Figures 4.13 – 4.15.

To calculate  $\mathcal{G}(c)$  a number of leave-one-out tests equal to the number of shape samples has been performed, so all the 100 shapes has been tested. The number of runs  $n$  carried out to calculate the  $\mathcal{S}(c)$  is 10000, as recommended by Davies in [96].

Despite  $\mathcal{S}(c)$  and  $\mathcal{C}(c)$  cannot be used as absolute measures of the quality of an SSM,  $\mathcal{G}(c)$  can be interpret, as said before, as an indication of the fitting error between the SSM and a target shape. As a consequence,  $\mathcal{G}(c)$  (Figure 4.13) indicates that the SSM built in this application is able to match a target shape with an expected absolute mean error equal to  $1.25 \pm 0.17$  mm since  $c$  (i.e. the number of the MoVs) has been defined equal to 73 to ensure an  $r$  equal to 0.98 (see Equation 4.7).

As said in the previous paragraph,  $\mathcal{G}(c)$ ,  $\mathcal{S}(c)$  and  $\mathcal{C}(c)$  are also employed to compare two different registration methods used for the establishment of correspondences across the training samples and to build the matrix  $\mathbf{TS}$ . Two different  $\mathbf{TS}$  are built using respectively the ICP-based registration and CPD-based registration. Then, the two SSMs here compared are provided by performing an SSA on the two  $\mathbf{TS}$  matrices.

Figures 4.16 – 4.18 show, respectively, the  $\mathcal{G}(c)$ , the  $\mathcal{S}(c)$  and the  $\mathcal{C}(c)$  of the two SSMs.

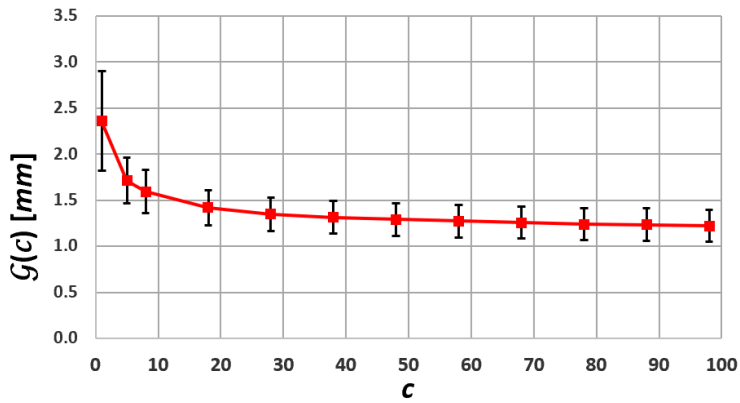


Figure 4.13: Generalization ability

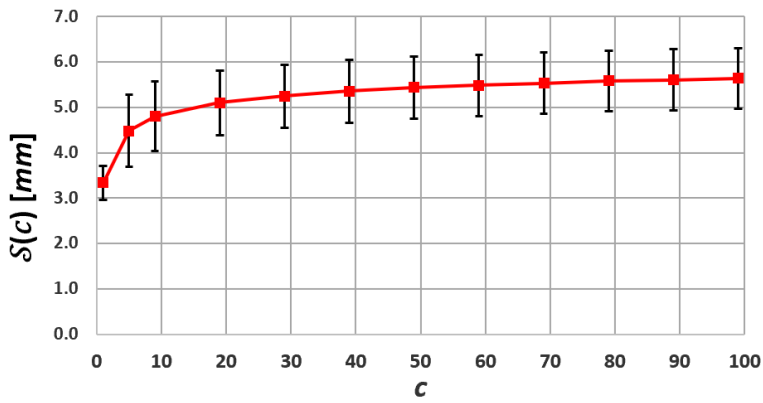


Figure 4.14: Specificity

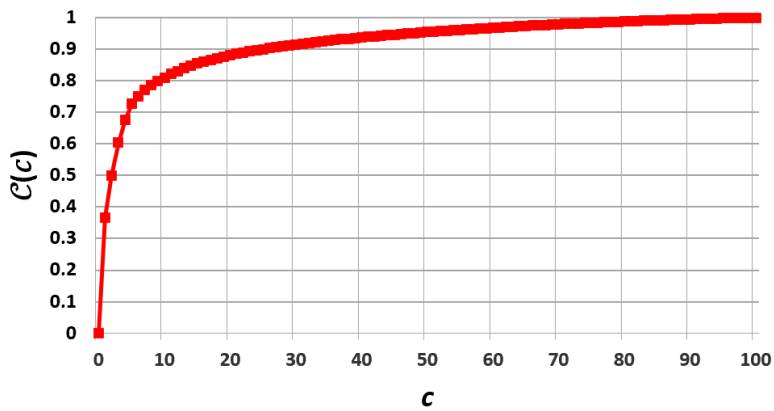


Figure 4.15: Compactness

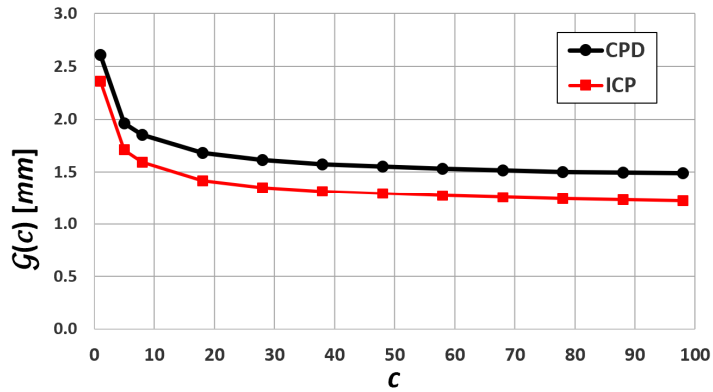


Figure 4.16: The comparison between the *Generalization ability* of the ICP-based model (square) and the CPD-based model (circle)

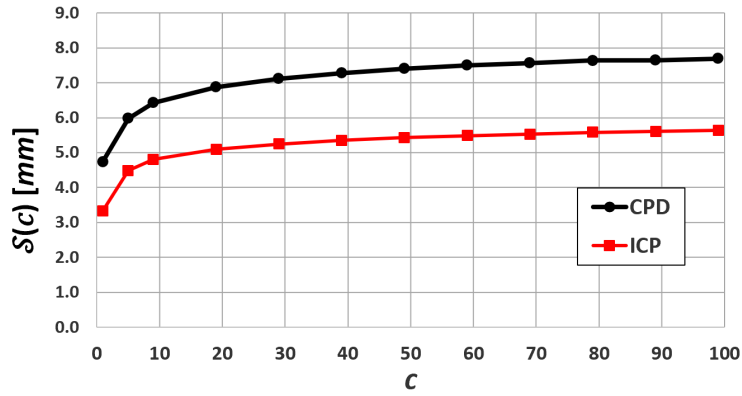


Figure 4.17: The comparison between the *Specificity* of the ICP-based model (square) and the CPD-based model (circle)

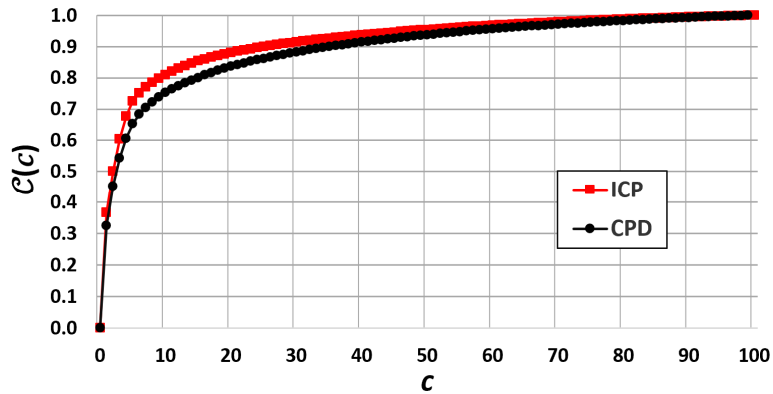


Figure 4.18: The comparison between the *Compactness* of the ICP-based model (square) and the CPD-based model (circle)

As shown in Figures 4.16, 4.17 and 4.18 (and as anticipated above), an ICP-based registration yields to a better SSM in terms of all the three measures. This proves that the ICP is able to provide a better SSM for this application; as a consequence, it has been actually used for the final implementation of the presented algorithm.

At last, one thing worth pointing out (although it seems trivial) regarding the quality of a statistical model is that it is strictly related on the quantity of available training data: enlarging the training set means increasing the variability of the resulting parametric model and therefore its accuracy. Unfortunately, the availability of 3D anatomical models is almost always too low, because of the modality with which these data can be collected: it is uncommon to have properly resolute diagnostic image of a healthy ROI. Furthermore, the required pre-processing (i.e. manual segmentation and model cleaning) is very cumbersome and time-consuming. This inevitably leads to training sets with few samples, resulting in models that are over-constrained. In other words, the restriction imposed on the allowed deformation do not enable them to adapt accurately to new data. For this purpose, methods to enlarge the training dataset without adding actual training samples have been proposed [56]. Among these methods, a promising one has been proposed by Luthi et al. [97] that exploits the mathematical framework of the *Gaussian Processes* to model shape variations: using analytically defined covariance functions to build significant priors it is possible to enlarge the training set in order to increase the variability and consequently the accuracy of the resulting parametric model. Obviously, the covariance functions have to be properly defined according to the ROI under consideration, since they must enable only consistent deformation on the mean shape.

This approach introduces a generalization of SSMs known as *Gaussian Process Morphable Models* (GPMMs).

Future developments of the procedure presented in this thesis for the construction of a parametric model of human cranial vault will concern the construction of GPMMs, instead of PCA-based SSMs, considering both real models and “mathematically defined” shapes as training samples to improve the quality of the resulting model.

## 4.2. Unilateral Defects: a robust and automatic method for the best *symmetry plane* detection of the craniofacial skeletons

When the defect is unilateral, i.e. it does not cross (or slightly crosses) the mid-sagittal plane, instead of the SSM, the contralateral healthy part of the neurocranium can be exploited as a template to retrieve the information needed to define the MPs, considering the skull almost symmetrical.

As briefly introduced in Section 3.1.3, the most widely used approach to face this class of defect uses a mirroring technique to superimpose the healthy half on the defective one. This approach greatly simplifies the problems discussed in Section 4.1 related to the fitting of an external source on the defective skull and also allows to exploit the patient's own data, which could potentially lead to better results (even if this strictly depends on the case under consideration).

To properly perform the mirroring approach, the accurate location of a reliable *symmetry plane* is fundamental since it enables a correct superimposition between the healthy half of the skull onto the defective one. So, in this case, the quality of the template is closely related to the quality of the *symmetry plane* around which perform the mirroring. On the other

hand, the definition of the *symmetry plane* is here not trivial, since there is no perfect symmetry in human skulls and a “perfect” *symmetry plane* cannot be strictly defined; in common practice it is usually approximated with the mid-sagittal plane (MSP) [13, 98 – 103], i.e. the plane that bisects the body vertically through the midline dividing the body, and, more specifically for this application, the cranio-facial skeleton, exactly in left and right side.

To date, the most widespread method in clinical practice computes the mid-sagittal plane location by a sequence of operations mainly involving manual landmarking on the cross-sectional slices (or, alternatively, on the 3D digital model) provided by diagnostic imaging. The MSP is then calculated based on the locations of at least 3 so-defined landmarks. This typical approach, referred to as *Cephalometric method*, is time-consuming, little reproducible and repeatable, and heavily depends on the professional experience of the operator that performs the landmarking. In addition, the possibility to select a large number of alternative landmarks on the craniofacial skeleton has given rise to many different definitions of the MSP plane; the consequence is that the best combination of landmarks to select to provide the optimal approximation of the MSP is still under debate.

In order to improve the accuracy and reliability of the MSP localization, several techniques have been proposed moving away from the traditional cephalometric approach toward more complex methodologies [104 – 107]. These alternative approaches are principally based on statistical techniques such as *Morphometric-based* (e.g. *Ordinary Procrustes Analysis (OPA)* [105]) or PCA followed by an ICP methods [104, 106]. Both are mirroring-and-registration methods, in which the midsagittal plane is established after a refined superimposition between the original skull and its mirrored configuration.

*Morphometric* methods reduce, but do not eliminate, the dependence of landmarks selection on the outcome; in addition, they continue to need the interaction with a skilled operator. On the other hand, ICP-based methods are landmark-independent, but fail in presence of strong asymmetries [4].

Di Angelo and Di Stefano [34] have recently proposed a fully automatic mirroring-and-registration method based on an original weighted function. Among all the analyzed methods, the results obtained in [34] for the *symmetry plane* detection for asymmetrically scanned human faces seemed to be the most promising for developing a method for estimation of the *symmetry plane* of skulls without interactions with the operator.

In this thesis, a new implementation of the algorithm presented in [34] has been provided, in order to overcome its major limitations (discussed in the following). The improved algorithm has been developed in collaboration with professors Di Angelo and Di Stefano from University of L’Aquila.

The new method has been tested for the *symmetry plane* detection of the human skulls; test cases include both synthetic and real skulls with large artificial or real defects. The results derived from these experiments and the comparison with the state-of-the-art are critically discussed hereinafter.

#### 4.2.1. Related work

The methods proposed in literature to *symmetry plane* detection of craniofacial skeleton can be classified into the following three categories:

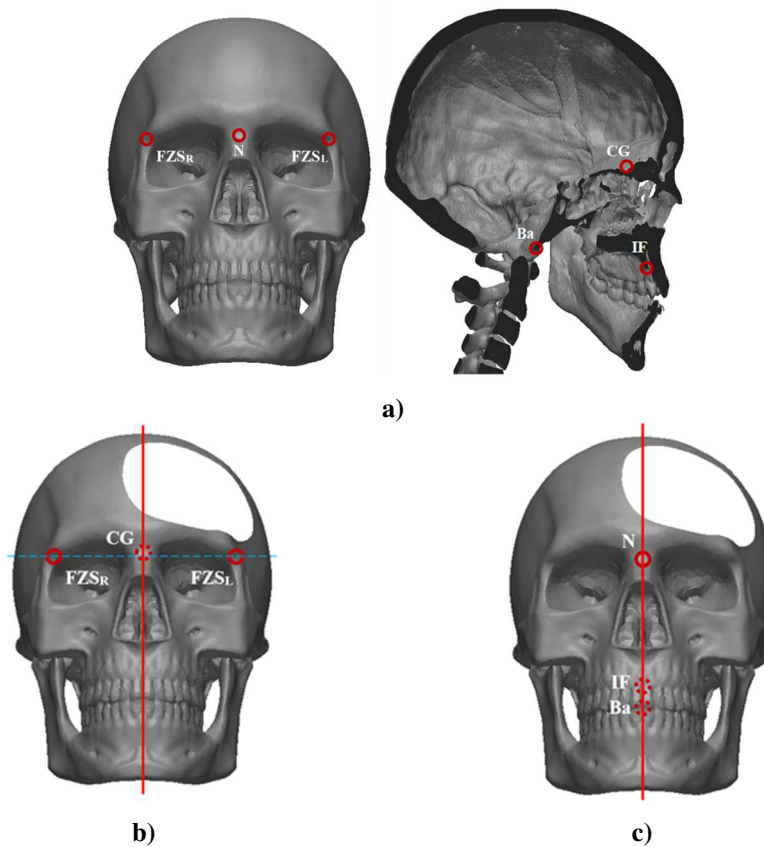
- *Cephalometric methods*;
- *Morphometric methods*;
- *ICP-based methods*.

### *Cephalometric methods*

In the clinical practice, the evaluation of the facial asymmetries is based on a cephalometric (2D or 3D) approach, which simplifies the analyses by using a selection of standardized landmarks. A very large number of possible landmarks combination has been explored in literature [103 – 105, 108]: some of the most relevant ones are reported in Table 1. Depending on published methods, the MSP is defined as the plane:

- passing through a central landmark (e.g. Nasion or Crista Galli, see Table 4.1) and perpendicular to a horizontal line crossing bilateral skeletal landmarks [109];
- of best fit passing through a selection of midline landmarks [110].

An example of the first type of MSP definition is proposed by Kim et al. [109], whose MSP is defined by Crista Galli (CG) and the left and right Frontozigomatic Sutures (FZS) (Figure 4.19(a) and Figure 4.19(b)). The accuracy of this method was demonstrated in [104]. Green et al. in [110] proposed the evaluation of MSP as the plane passing through the three central landmarks: Nasion (N), Basion (Ba) and the Incisive Foramen (IF) (Figure 1.a and Figure 1.c). According to the authors results, this choice leads to better results than using the lateral ones.



**Figure 4.19:** a) Landmarks localization; b) MSP definitions according to methods proposed in [109] and c) [110]

As qualitatively showed in Figure 4.19, the main advantage of using landmarks is that the result is not affected by all skeletal defects and the considered reference points set can be changed and adapted as needed. On the other hand, it has been demonstrated that different landmarks set could lead to very different MSP [105]; there is still no consensus on the best set of landmarks to consider, and on which is the most accurate cephalometric plane. In any case, some authors highlight that a symmetry plane defined using manually identified cephalometric landmarks results in not very accurate estimations of symmetry, principally for the lack of accuracy and reproducibility of landmark identification and selection strategies [34, 104, 106, 111 – 113].

Although there have been some attempts to automate the selection of landmarks [112], to date the selection is still completely manual and, as such, the operation is tedious and must be performed by a skilled person.

**Table 4.1: Landmarks definition**

Landmark	Abbr.	Definition
<i>Basion</i>	Ba	Most anterior point on the margin of the foramen magnum in the mid-sagittal plane
<i>Nasion</i>	N	Most anterior point of the frontonasal suture in the mid-sagittal plane
<i>Crista Galli</i>	CG	Most Superior point of the Crista Galli
<i>Incisive Foramen</i>	IF	Midpoint of the Incisive Foramen
<i>Frontozygomatic Suture</i>	FZS	The most medial and anterior point of left (FZSL) or right (FZSR) frontozygomatic suture at the level of the lateral orbital rim
<i>Supraorbital Foramen</i>	SOF	Midpoint of supraorbital foramen
<i>Frontorbitomaxillare</i>	FOM	Lateral point of the frontomaxillary suture on the medial margin of the orbit
<i>Frontonasomaxillare</i>	FNM	Intersection of the nasomaxillary, frontomaxillary, and frontonasal sutures
<i>Sella</i>	S	Center of the Sella Turgica
<i>Pogonion</i>	Pog	Most anterior point of the bony chin in the median plane
<i>Anterior Nasal Spine</i>	ANS	Most anterior midpoint of the anterior nasal spine of the maxilla

### ***Morphometric methods***

The *Morphometric* method for defining the plane of symmetry of a craniofacial skeleton has been proposed by Damstra et al. in [105] and results demonstrate that the technique can potentially produce very accurate and reliable MSP. It exploits the *Ordinary Procrustes Analysis* (OPA) applied to landmarks manually defined by the user. In particular, the proposed method requires the identification of visible facial anatomical landmarks in the supraorbital and nasal bridge region for the superimposition (SOF, FNM, FZS, and FOM as defined in Table 4.1 and shown in Figure 4.20(a), and three central landmarks (S, ANS and Pog, as defined in Table 4.1 and Figure 4.20(a) for the MSP definition. The original surface model and centroid landmarks are mirrored around an arbitrary plane. A shape alignment by means of partial OPA is then applied to attain the superimposition. The centroid markers of

the original and mirrored surface models are superimposed using a rigid translation. Then, a rigid rotation of the mirrored landmarks configuration around the geometric midpoint of the superimposed centroid markers is performed until the best fit between all homologous supraorbital and nasal bridge landmarks are achieved by means of the least squared point distance. The MSP is defined as the plane passing through three points, in Figure 4.20(b) called  $S^*$ ,  $ANS^*$  and  $Pog^*$ , each of which is the midpoint of the segment joining the original landmarks  $S$ ,  $ANS$  and  $Pog$  with their mirrored counterparts.

Although the resulting MSP can be considered more reliable than the one obtained through a cephalometric approach, *Morphometric* methods are still landmarks-depend requiring the interaction of a skilled operator. In addition, as said above, the ICP-based mirroring-and-registration technique fails in the presence of strong asymmetries, leading to questionable results.

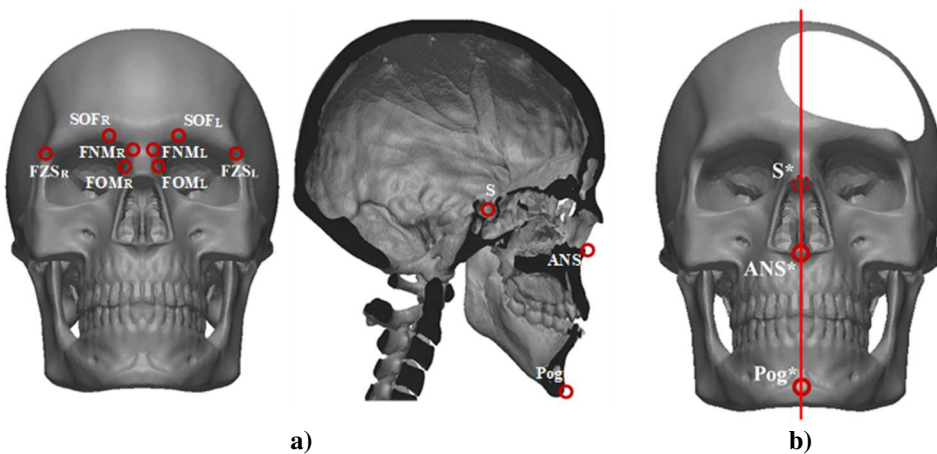


Figure 4.20: a) Landmarks and MSP definitions according to methods proposed in b) [105]

### *ICP-based methods*

The ICP-based approach is a mirroring-and-registration method. The mirroring of the original data is carried out with respect to an initial plane of symmetry, which is usually estimated by the PCA [34, 104, 106, 107, 114]. Then, the source point cloud and the mirrored data are registered by means of an ICP algorithm [73]. After alignment, the MPS is calculated by approximating, in the least-squares sense, the middle of the segments joining homologous points in the original and mirrored point cloud. The superimposition can be done using:

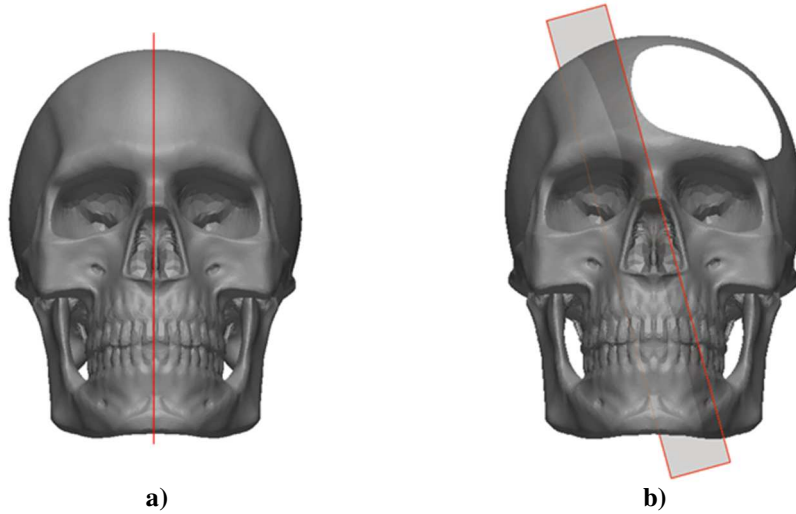
- complete models [104, 114];
- some homologous surface areas selected by the user on the left and right facial skeleton [106] or by specifically designed operators [107].

Although the ICP-based approach can be easily automated, being landmarks-independent, its use for MSP localization in clinical practice is mainly limited by 2 factors:

- the final solution is strictly affected by the initial one;
- the function to be minimized considers likewise all the points of the model, including local defectiveness, such as holes or bony prominences, that should not be considered in the evaluation of symmetry plane of the skull.



Figures 4.21(a) and Figure 4.21(b) show, respectively, MSP evaluation by using our implementation of [114] of a perfectly symmetric synthetic skull and a synthetic skull with a local asymmetry. It is evident that these approaches are not able to achieve an acceptable result for the skull in presence of asymmetries, even if the asymmetry is localized.



**Figure 4.21: MSP resulting by methods proposed in [114] for (a) complete and (b) defective skull**

#### 4.2.2. The Mirroring and Weighted Approach

The proposed method is an upgraded version of the mirroring-and-registration technique presented in [34] (in the following referred as *MaWR method: mirroring and weighted registration method*) proposed for bilateral symmetry estimation of human faces. It is based on an iterative registration algorithm which minimizes an objective function specifically designed to filter out any kind of asymmetry.

In the following sections, the published method, its limitations, and the proposed improvements to extend its applicability to skulls as well are presented

##### The published method

The published method [34], whose flow-chart is depicted in Figure 4.22, starts from a 3D discrete model ( $PC$ ) and evaluates the symmetry plane by a preliminary first-attempt ( $\Pi_0$ ), carried out with a PCA algorithm, which is then refined iteratively until its final estimation.

The final estimation  $\Pi_f$  of the MSP is obtained by the Levenberg-Marquardt algorithm [115] that iteratively minimizes the following objective function ( $OF_i$ ), whose expression at the  $i$ -th step is:

$$OF_i = \frac{\sum_{j=1}^n [w_{i,j} \cdot d_{\text{Haus}}(p_j, T(PC_{m,i}))]}{\sum_{j=1}^n w_{i,j}} \quad (4.25)$$

where:

- $n$  is the number of points of the source point cloud ( $PC$ );
- $p_j$  is the  $j$ -th point belonging to  $PC$ ;
- $T(PC_{m,i})$  is the tessellated surface of the mirrored data at  $i$ -th iteration ( $PC_{m,i}$ );
- $d_{\text{Haus}}(p_j, T(PC_{m,i}))$  is the *Hausdorff distance* between  $p_j$  and  $T(PC_{m,i})$ ;
- $w_{i,j}$  is the weight associated to  $p_j$  at  $i$ -th iteration.

The *Hausdorff distance* is calculated between each point  $p_j$  on the source  $PC$  and the tessellated surface  $T(PC_{m,i})$ , instead of point-point, in order to avoid the asymmetry in surface sampling and to make the distance as independent as possible on points density.

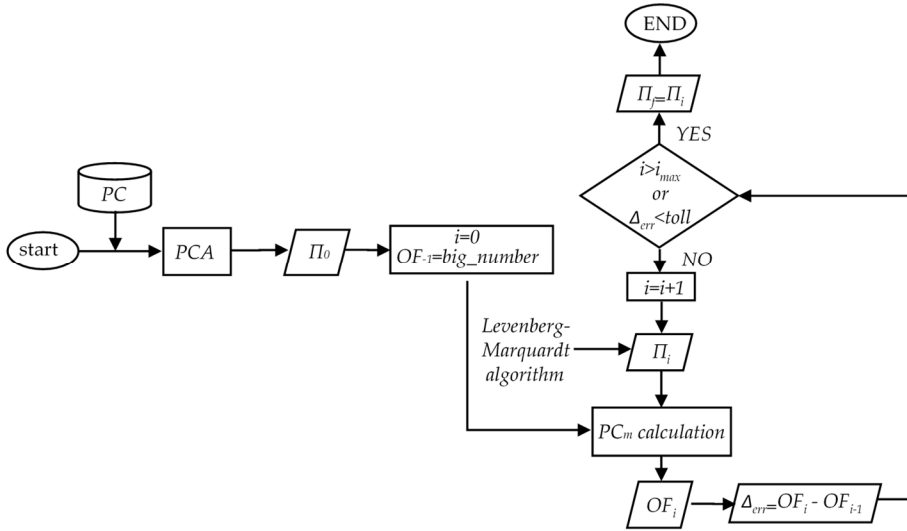


Figure 4.22: The flow chart of the *MaWR* methods as presented in [34]

The weights  $w_{i,j}$  play an important role in the functionalities of the method being presented. They are expressed as the product of two specific weights:

$$w_{i,j} = w_{s,i,j} \cdot w_{r,i,j} \quad (4.26)$$

The weights  $w_{s,i,j}$  and  $w_{r,i,j}$  are both expressed according to the *Leclerc function* [116] which has its maximum in correspondence to the symmetry plane:

$$w_{s,i,j} = \frac{1}{\sigma_s^2} e^{-\left(\frac{d_{i,j}}{\sigma_s}\right)^2} \quad (4.27)$$

$$w_{r,i,j} = \frac{1}{\sigma_r^2} e^{-\left(\frac{d_{\text{Haus}}(p_j, T(PC_{m,i}))}{\sigma_r}\right)^2} \quad (4.28)$$

Where:

- $d_{i,j}$  is the distance between  $p_j$  and the symmetry plane  $\Pi_i$  (at the  $i$ -th iteration).

- $\sigma_s$  and  $\sigma_r$  define, respectively, the distance and the radius values for which the weight is the 36.79% of its maximum value [116].

The weight  $w_{s,i,j}$  works to reduce the effects of the asymmetries in the acquisition process which are mainly located far from the symmetry plane. The weight  $w_{r,i,j}$  works as a filter which excludes from the registration process any local asymmetries, whether they are near or far from the symmetry plane.

More details about the original algorithm can be found in [34].

#### Main limitations and proposed improvements

Although the method presented in [34] represents a valid tool for estimation of the plane of symmetry for human faces acquired by a 3D scanner, it leads to questionable results when applied to a 3D skull model presenting local asymmetry, as shown in Figure 4.23(a). This is mainly due to two different limitations affecting the algorithm: the weight definition  $w_{i,j}$  (Equation 4.26) and the objective function's (Equation 4.25) minimization strategy.

The weight definition is designed to avoid also the effects of the asymmetries due to the acquisition process. Since for a 3D facial-cranial skull model coming from CT images the acquisition quality is not affected by the distance from the symmetry plane and the most symmetrical areas may be those that are farthest from the symmetry plane, the weight  $w_{s,i,j}$  proves to be not only useless but also negatively affecting the results.

For this reason, in the new version of the algorithm, the contribution of  $w_{s,i,j}$  has been neglected and the weight  $w_{i,j}$  works only as a filter which excludes from the registration process any local asymmetries:

$$w_{i,j} = w_{r,i,j} = \frac{1}{\sigma_r^2} e^{-\left(\frac{d_{\text{Haus}}(p_j, T(PC_{m,i}))}{\sigma_r}\right)^2} \quad (4.29)$$

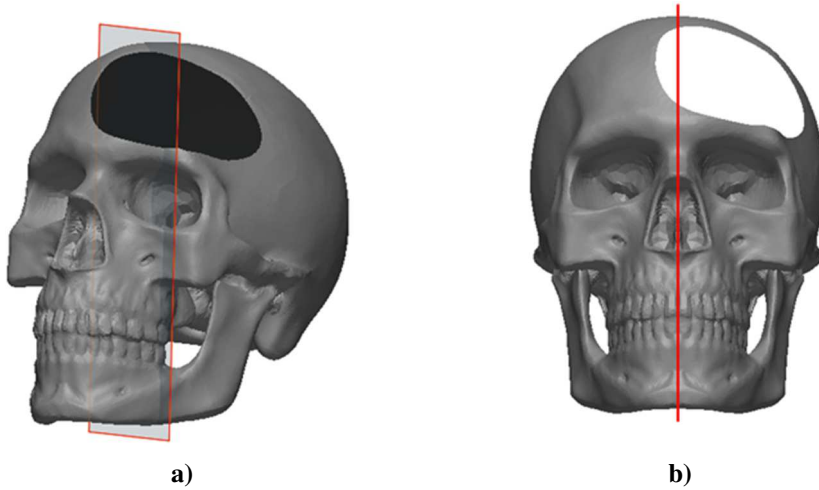
Large values of  $\sigma_r$  guarantee a robust registration, whereas small values allow a greatly accurate registration of the symmetric parts, excluding all asymmetries. In the experiments described hereafter, since we analyze real skulls with large asymmetries, the value of  $\sigma_r$  is assumed to be the 50 % of the maximal width of the skull.

Dealing with the minimization strategy, the Levenberg-Marquardt algorithm used to minimize the objective function proved unable to get out of the local minimum resulting after the PCA. For this reason, the new algorithm uses the Particle Swarm Optimization (PSO) [117] which belongs to the class of Meta-heuristic algorithms, whose adoption is widespread in practical applications for the lower computational burden and lack of strict usage hypothesis with respect to exact methods. Although the convergence to a global minimum cannot be guaranteed, we observed that in all the considered scenarios, by using an appropriate search space, good solution (considering the application here analyzed) is found.

The discussed improvements have been implemented in a new algorithm specially designed for the symmetry plane detection of the craniofacial skeleton. As shown in Figure 4.23b, the novel algorithm can potentially lead to much better results compared with the ones obtainable with the original version.

The proposed algorithm has been tested upon several models, both healthy and with significant asymmetric areas to evaluate its ability to provide a reliable approximation of the *symmetry plane* of the skull. The results are reported in the following Section.

Instead, the assessment of the ability of this approach to provide an effective model for the definition of MPs will be presented in Chapter 5, where the results of the reconstruction algorithm in its entirety will be discussed.



**Figure 4.23:** The MPS resulting from: a) the *MaWR* method as presented in [34]; b) the *MaWR* improved method

#### 4.2.3. Evaluation of the proposed procedure for the *symmetry plane* detection

The proposed method (*MaWR-method*), has been implemented in an original algorithm, coded in MATLAB. In order to evaluate the *MaWR-method* accuracy in the identification of the *plane of symmetry* of craniofacial skeletons, selected test cases have been designed and the resulting planes are compared with the ones provided by two *Cephalometric methods* (*Cplm1-method* proposed by Kim et al. [109] and *Cplm2-method* proposed by Green et al. in [110]) and the *Morphometric method* (*Mpm-method*) proposed in [105]. These three methods, already presented in Section 4.2.1, have been selected since, according to [104], [105] and [110], they tend to deliver more reliable results amongst those published in the literature.

The performances of the proposed method are quantified and compared with the state-of-the-art by analyzing 20 skulls, segmented from anonymous CT provided by the Meyer Children Hospital of Florence (Italy): two healthy real skulls, and 18 real defective skulls with large defects. This pool of 18 cases includes (i) large unilateral defects, (ii) large bilateral defects and (iii) large defects crossing the MSP; they have been deemed by hospital doctors as representative of the clinical cases they commonly face.

In the following, the experimental analysis will be discussed in detail; the results of all the cases will be reported, but, for the sake of brevity, only for the first 5 test cases the model will be shown explicitly.

These 5 test cases include:

- TC#1 and TC#2, which are two healthy real skulls (Figure 4.24(a – b)), to demonstrate the reliability of each method in real cases. For TC#2 an incomplete skull model has been chosen because, commonly, the TC images acquisition addresses only the region of interest to reduce the irradiation risks.
- TC#3, TC#4 and TC#5, which are real defective skulls with a large defect (so, large asymmetry) (Figure 4.24(c – d – e)), to demonstrate the reliability and

the robustness of the new method compared with the other approaches. These three case studies include one unilateral defect, one bilateral defect and one defect crossing the MSP.

For each skull, a proper segmentation of the hard tissue of the skull is provided by a skilled operator using Materialise Mimics® software. Then, the segmented region is exported as a surface model (i.e., in STL format) and analyzed by using the four previously mentioned methods for the *symmetry plane* estimation. For the cephalometric and the morphometric methods, all the landmarks in Table 4.1 are manually selected by a skilled operator using the volume renderings and the cross-sectional slices in all three planes of the CT images.

Since no real skull is perfectly symmetrical and the *plane of symmetry* does not actually exist, in this paper the comparison among the four methods here considered is carried out by an original index, named *Asymmetry Value (AV)*:

$$AV = \text{median}(AV_{\text{point}}) \quad (4.30)$$

Where:

$$AV_{\text{point}} = \text{dist}(p_j, T(PC_{m,i})) \quad (4.31)$$

The *AV* is defined as the mean of  $AV_{\text{point}}$  that is the Euclidean distances between each point of the source point cloud ( $p_j$ ) with respect to its closer tessellated surface triangle ( $T(PC_{m,i})$ ) of the mirrored configuration. The mirrored configuration is obtained reflecting the *PC* upon the estimated *symmetry plane*. The distance point-triangle permits to avoid the asymmetries due to the surface model sampling. The *AV* is calculated as the median instead of the mean in order to reduce the weight of the natural little asymmetrical skull's regions in the calculation. The distance point-triangle permits to avoid the asymmetries due to the surface model sampling.

Preliminarily, it has been verified that for the synthetic mesh previously showed (Figure 4.21(a)), the *AV* value is zero. For real skulls, based on the previously mentioned considerations, the *AV* value cannot be zero; however, the method for which the *AV* is smallest performs the best localization of the *symmetry plane*.

The MSPs of all the 20 skull surface models are calculated using the proposed algorithm (*MWR-method*), a morphometric-based (*Mpm-method*) and two *cephalometric-based methods* (*Cplm1-method* and *Cplm2-method*). The calculated *AV* is then used to perform a direct comparison among the different approaches.

Table 4.2 shows the *Asymmetry Value* related to the different MSPs calculated for each of the considered test cases. For the TC#5, the MSP is not evaluated for *Cplm2-method* since, being the TC incomplete, the landmark IF is missing. Table 4.2 shows that the proposed method is able to find the MPS with a comparable *AV* value (in fact, always lower for all the test cases) with respect to the other methods without any user's interaction. The presented approach has therefore proved capable of obtaining a clinically acceptable result in a fully automatic manner.

It is worth to note that even small differences in terms of *AV* correspond to different three-dimensional distributions of asymmetries on the skull. As an example, in Figure 4.25 the  $AV_{\text{point}}$  maps for the TC#5 and the four methods compared here are shown. It is evident that the proposed method determines a better localization of the *symmetry plane* than the state-of-the-art alternatives.

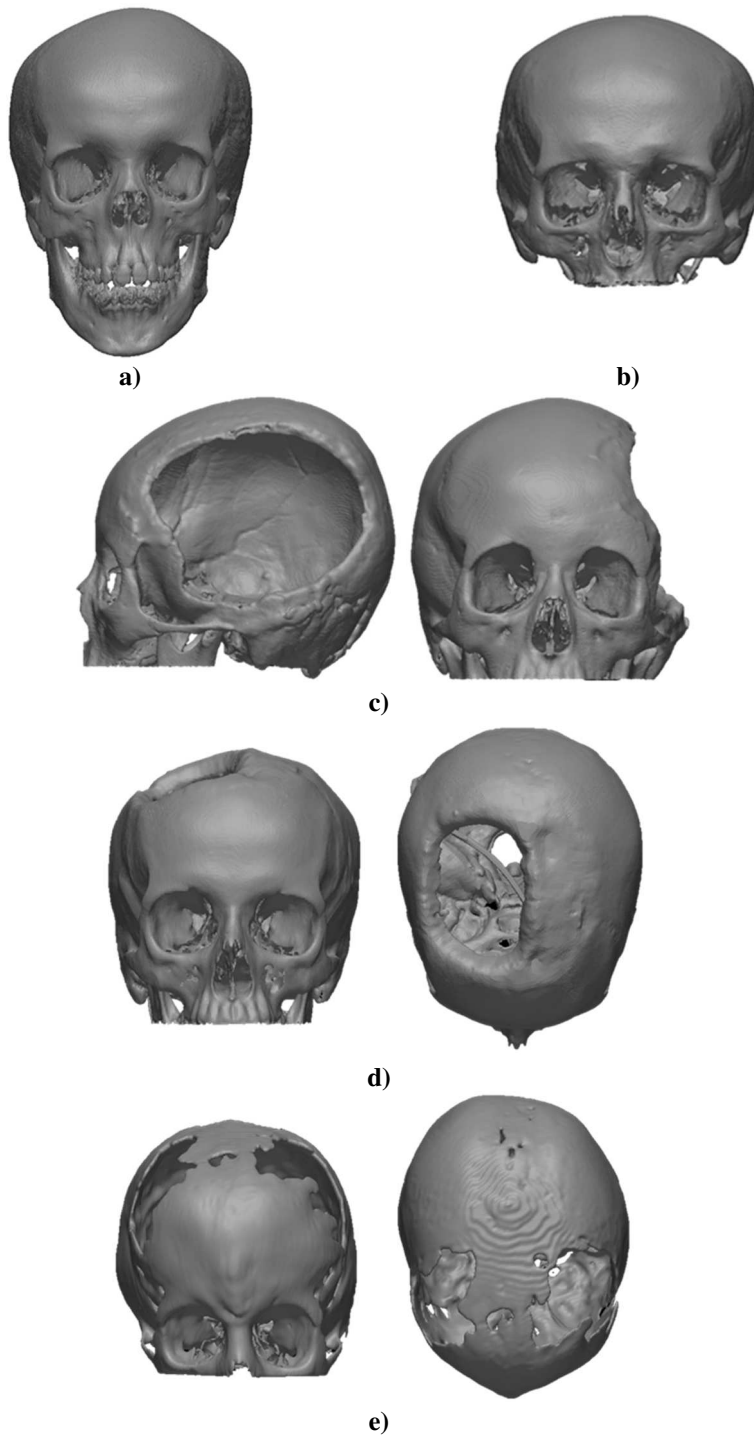


Figure 4.24: The first 5 test cases. a) TC#1; b) TC#2; c) TC#3; d) TC#4; e) TC#5

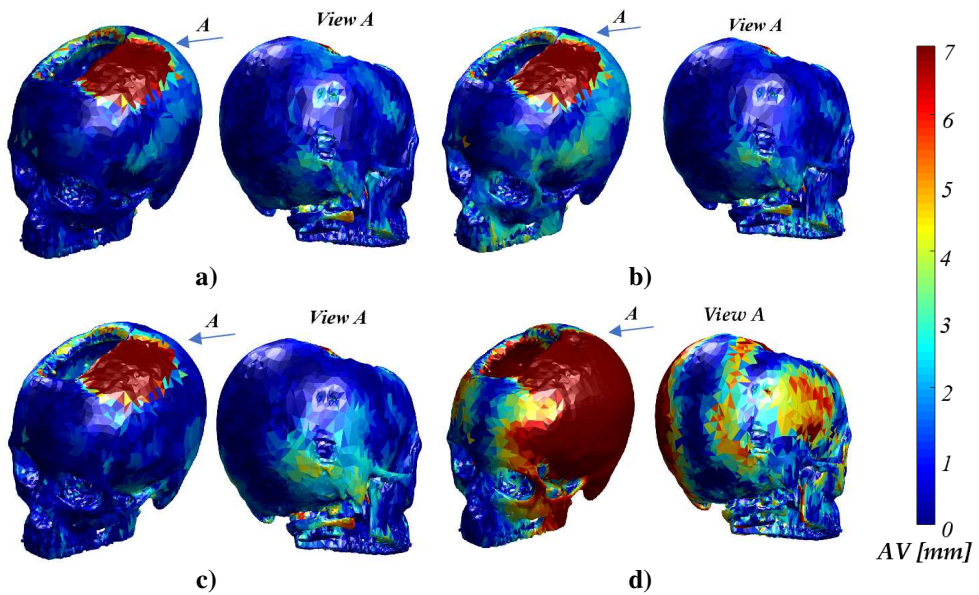
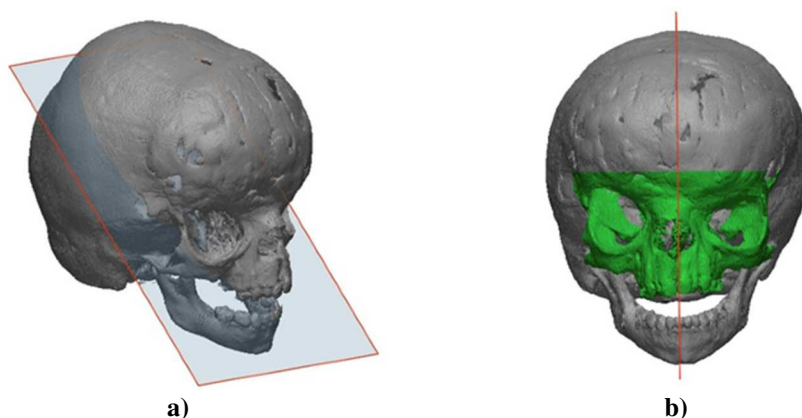


Figure 4.25: The AV maps for the TC#5 and the four methods here compared

Table 4.2: The Asymmetry Value for the twenty test cases and four methods analyzed. The best value for each row is bolded

Test cases	MWR-method	Mpm-method	Cplm1-method	Cplm2-method
TC#1	<b>0.95</b>	1.02	0.98	0.97
TC#2	<b>0.66</b>	1.09	0.72	0.73
TC#3	<b>0.78</b>	0.88	1.01	1.01
TC#4	<b>0.76</b>	0.88	0.80	1.48
TC#5	<b>1.30</b>	1.56	1.59	--
TC#6	<b>1.11</b>	1.33	1.43	1.21
TC#7	<b>0.75</b>	0.81	0.88	1.24
TC#8	<b>0.63</b>	0.72	0.76	0.75
TC#9	<b>0.65</b>	0.80	0.75	0.76
TC#10	<b>1.02</b>	1.13	1.18	1.27
TC#11	<b>1.26</b>	1.52	1.38	1.55
TC#12	<b>0.87</b>	1.24	1.25	1.20
TC#13	<b>1.04</b>	1.11	1.42	1.39
TC#14	<b>0.76</b>	0.84	0.86	1.10
TC#15	<b>0.89</b>	1.07	1.21	1.20
TC#16	<b>0.69</b>	0.92	0.90	0.98
TC#17	<b>1.18</b>	1.40	1.24	1.37
TC#18	<b>0.70</b>	0.85	0.97	0.92
TC#19	<b>1.23</b>	1.39	1.56	1.55
TC#20	<b>0.84</b>	1.09	0.93	0.92

The proposed method, as it was presented, fails in the case in which the symmetry plane of the skull does not coincide with the MSP. Among all the analyzed test cases, this occurred only for a rare case of craniofacial dysmorphism due to hypertelorism combined with a severe form of plagiocephaly (Figure 4.26(a)). In this case, the user has to segment the area (highlighted in green in Figure 4.26(b)) for which the symmetry plane approximates the MSP one. However, even in this case, the selection is much faster and easier to perform than the landmark identification.



**Figure 4.26: Skull with craniofacial dysmorphism due to hypertelorism combined with a severe form of plagiocephaly. a) MSP resulting from the proposed method; b) MSP resulting from the proposed method applied to the user selected area highlighted in green.**

Summing up, a new fully automatic technique able to extract an accurate and reliable symmetry plane is proposed. It is, indeed, an ICP-based method with a specifically designed objective function and minimum searching function, which has proved to be robust to local minima.

The performances of the proposed method were quantified and compared with the ones of other recent techniques by analyzing 20 skulls, and experimental results demonstrated that the method leads to the accurate localization of the MSP even in cases where there are a very large missing areas and strong asymmetries without any user interaction and any landmark selection.

Regarding the aim of this thesis, this consists of an effective procedure able to find a reliable *symmetry plane* around which perform the mirroring to superimpose the healthy half of the neurocranium on the defective one and, consequently, to retrieve a consistent shape prediction of the missing or deformed part to be reconstructed. The proposed method, being automatic, overcome the discussed shortcomings of the existing approaches, which are time consuming and quite inaccurate.

Furthermore, this procedure can be easily integrated into the reconstructive method proposed in this thesis, since it can work on the same STL on which the whole reconstructive procedure works, without requiring further user's interaction.



Concerning the computational time, it is closely related to the resolution of the surface model (number of points of the PDM) and the complexity of the model itself. For the analyzed test cases, 3D discrete models with points number from 80000 to 120000, the computational time was between 10 and 25 minutes. The algorithm is tested with CPU Intel® Core™ i7-4712HQ/2.3 GHz and RAM 16 GB.



## **5. Results**

The activity presented in this Ph.D. thesis deals with the development of a procedure for the reconstruction of a defective or deformed anatomy, specifically tailored for human neurocrania. Since in Cranioplasty the surgical outcome is mainly related to aesthetics, a consistent shape restoration represents an essential requirement to ensure a successful reconstruction. In the previous Sections, a new approach to face the cranial reconstruction starting from the defective model has been presented.

In this Chapter, the quantitative assessment of the reconstructions carried out through the devised procedure, applied on several case studies, is presented and described in detail.

In addition, in the first Section, new evaluation criteria to assess the quality of the cranial vault restoration are discussed, and a new evaluation approach is proposed accordingly.

### **5.1. New Evaluation criteria**

In the related literature, the main criterion for evaluating a reconstructive patch is how closely it matches the original surface. For this purpose, usually the test cases addressed are represented by a complete skull with artificial holes [14] since the original surface of a real defective skull is rarely known.

Notwithstanding, in the author's view such comparison does not represent the best criterion for assessing the reconstruction outcome. At first analysis, it is not applicable in the normal clinical practice as the original surface is commonly unknown. More importantly, it does not consider the actual aesthetical outcome, which is the most relevant aim in the cranial vault shape restoration [8, 9, 15]. In addition, the skull to be reconstructed has often high asymmetries or visible dysmorphism and retrieving the original shape could be a questionable strategy.

Consequently, further investigations have concerned with the definition of quantitative criteria able to objectively assess the quality of the reconstruction of a human neurocranium, considering that the criteria to evaluate the reconstruction outcome should not be influenced by how close the restored skull is to the original surface.

In this thesis it has been emphasized several times that, for an acceptable aesthetical outcome, it is necessary to obtain a restored cranial vault as symmetrical as possible and with no discontinuity between the reconstructed patch and the surrounding bone.

With this aim, a new evaluation approach is here proposed: it allows both a quantitative evaluation of the skull asymmetry by introducing an index and a point-by-point map to evaluate the continuity of the entire cranial vault.

The asymmetry index is evaluated by means of the same Asymmetry Value ( $AV$ ) already presented in Equation 4.30 and here re-proposed for sake of clarity:

$$AV = \text{median} \left( \text{dist} \left( p_j, T(PC_{m,i}) \right) \right) \quad (5.1)$$

where:

- $p_j$  is the  $j$ -th vertex belonging to the restored skull model. The Point-Cloud formed by the vertices of the restored skull model is named  $PC$ .
- $PC_m$  is the mirrored configuration of the  $PC$ . The mirrored configuration  $PC_m$  is obtained reflecting  $PC$  upon the same *symmetry plane* used throughout the procedure (see Section 2.3).
- $T(PC_m)$  is the tessellated surface obtained from the vertices  $PC_m$ .

As mentioned in the related Section,  $AV$  provides a quantitative evaluation of the overall skull asymmetry: small value of the  $AV$  index means a symmetrical reconstruction and, consequently, an acceptable outcome.

In addition, the reconstruction consistency is checked also by looking for any discontinuities at the boundary between the bone and the reconstructed patch by means of the point-value of the  $AV$ , named  $AV_{point}$  and defined as in Equation 4.31:

$$AV_{point} = \text{dist} \left( p_j, T(PC_{m,i}) \right) \quad (5.2)$$

When applied throughout the cranial vault,  $AV_{point}$  provides the color map of the local asymmetries between the  $PC$  and the  $PC_m$ , suitable to highlight possible macroscopic discontinuities at the connection region between the bone and the patch.

It is worth to note that the proposed evaluation can be applied also to assess the reconstruction when the original healthy shape is completely unknown, that represents the most common situation in the actual clinical practice.

The new metrics ( $AV$  and  $AV_{point}$ ) have been applied on several case studies to evaluate the accuracy of the proposed approach in the cranial shape restoration. A thorough discussion about the results is reported in Section 5.3.

Before that,  $AV$  and  $AV_{point}$  have also been used to define the best combination of the parameters required as inputs for the reconstruction algorithm, as explained in Section 3.2. The description of the test campaign carried out to define such parameters is reported in Section 5.2.

For all the case studies addressed, the CT images are provided by the Children's Hospital A. Meyer of Florence and include the neurocrania of Caucasian males and females aged between 11 and 33 years, both healthy and defective. For each test case, the skull bone has been segmented and exported in STL format by a skilled user by means of Materialise® Mimics' tools. The obtained STL is used as an input for the procedure presented in this thesis. The whole procedure has been implemented in an original algorithm coded in MATLAB®.

## 5.2. Estimate of input parameters

In addition to the STL of the defective neurocranium to be reconstructed, the algorithm requires also three more input parameters:

- $\bar{d}$ , that represents the maximum distance (in *mm*) to search the model's points as neighbors of the ones belonging to the template.
- $m$ , that represents the minimum distance (in *mm*) between the boundary loop and outer ring of the MPs.
- $n$ , that represents the number of points-rings lying in the outer side of the boundary loop to create an overlapping region between the interpolating surface and the healthy bone.

For further information about the three parameters, see Section 3.2 and Figure 3.8.

Before facing the actual reconstruction task, several tests have been performed in order to define the best combination of the three parameters.

This preliminary experimental campaign involved 15 models, including 5 real defective skulls, 9 real skulls with synthetic defects and a synthetic skull with synthetic defects. Both unilateral and non-unilateral defects have been considered.

Regarding the parameter  $\bar{d}$ , the tests showed that it does not affect the reconstruction when it is defined greater than a certain threshold: large values of  $\bar{d}$  actually ensure that all the points of the template that fall inside the boundary loop are selected as possible MPs. Furthermore, high values of  $\bar{d}$  have shown to have no negative consequences for the algorithm. So, after an initial tuning,  $\bar{d}$  has been imposed equal to 100 in all the tests reported henceforward.

The tests have therefore been carried out by applying twelve times the algorithm to each of the 15 test cases with the parameters  $m$  and  $n$  combined as follow:

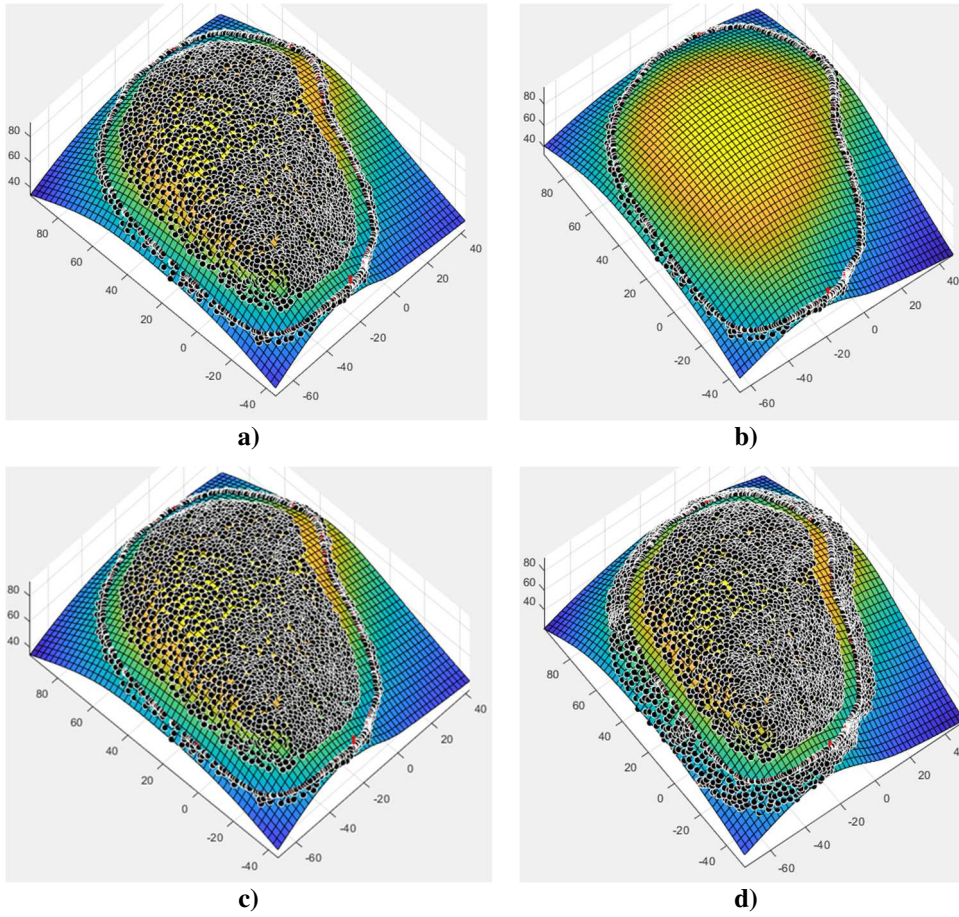
**Table 5.1: The combinations of parameters  $n$  and  $m$  in each of the test case addressed**

	$m=10\text{ mm}$	$m=25\text{ mm}$	$m=40\text{ mm}$	$m=80\text{ mm}$
$n=10\text{ rings}$	$n=10 ; m=10$	$n=10 ; m=25$	$n=10 ; m=40$	$n=10 ; m=80$
$n=40\text{ rings}$	$n=40 ; m=10$	$n=40 ; m=25$	$n=40 ; m=40$	$n=40 ; m=80$
$n=70\text{ rings}$	$n=70 ; m=10$	$n=70 ; m=25$	$n=70 ; m=40$	$n=70 ; m=80$

The choice of the  $m$  and  $n$  values is defined as explained in the following.

With the minimum value of  $m$ , the MPs are very close to the boundary loop but far enough not to compromise the continuity of the reconstructed surface. Values less than 10 would lead to interpolation centers too close to the boundary loop: this situation is to be avoided because it would lead to the same continuity problems as in the typical *Template-based* approaches. On the other hand, the maximum value of  $m$  has been chosen because it guarantees to have no MPs, i.e. to consider a typical *Surface Interpolation-based* approach. For these reasons, values less than 10 and greater than 80 are not significant for the parameter  $m$ .

Figure 5.1(a) and Figure 5.1(b) depict the interpolating surface passing through the showed centers defined with, respectively,  $m=10$  and  $m=80$ . In both the Figures,  $n$  is defined equal to 10.



**Table 5.2:** The reconstructed surface by varying the interpolation centers. The outer rim are the  $n$ -RNs and the BPs while the inner points are the MPs. a)  $n=10$  and  $m=10$ ; b)  $n=10$  and  $m=80$ ; c)  $n=10$  and  $m=10$ ; d)  $n=40$  and  $m=10$

Regarding the  $n$  value, it relates to the thickness of the overlapping region between the interpolating surface and the healthy bone: the larger is  $n$  the more extensive is the overlapping region.

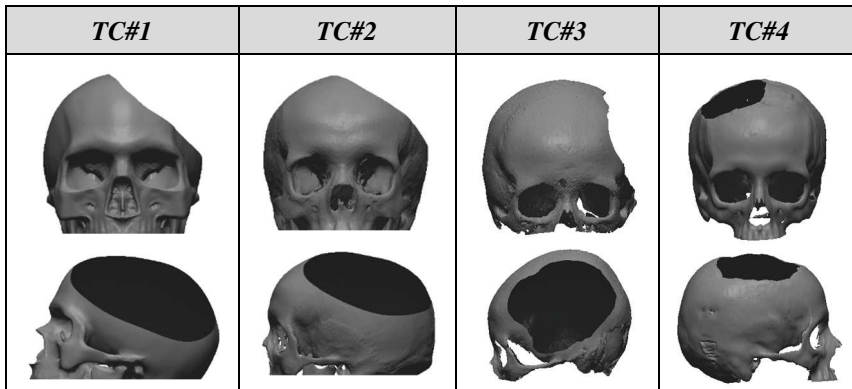
Figure 5.1(c) and Figure 5.1(d) show the interpolating surface passing through the centers defined with, respectively,  $n=10$  and  $n=40$ . In both the Figures,  $m$  is defined equal to 10.

As for  $m$ , values less than  $n=10$  or greater than  $n=40$  have proved to be non-significant for the parameter  $n$ . In particular, the resulting reconstruction has proved to be not very sensitive to small variations of the parameter  $n$ , and imposing values less than 10 would be equivalent to imposing  $n = 10$ . Obviously,  $n=0$  has been not taken into consideration because it cannot ensure the continuity of the curvature between the healthy bone around the defect and the reconstructed patch (see Section 3.2.4).

The tests showed consistent results in all the 15 case studies considered. In the following, a selection of 4 representative models is presented and discussed in detail. The discussed models are showed in Table 5.3 and include:

- TC#1 and TC#2 which are, respectively, a synthetic and perfectly symmetric skull and a real skull. Both have a large synthetic defect that crosses the sagittal plane
- TC#3 and TC#4 which are real defective skulls with, respectively, a purely unilateral large defect and a defect which slightly crosses the *symmetry plane*

**Table 5.3: The four test cases discussed in detail**



Tables 5.4 – 5.7 show the results of the test campaign carried out on the four case studies and presented in Table 5.3.

The results show that the quality of the reconstruction heavily depends on the  $m$  value, while it is little influenced by the value of  $n$ . In particular, the best reconstruction can be achieved by imposing a low value of  $m$ , i.e. by minimizing the distance between the MPs and the boundary loop.


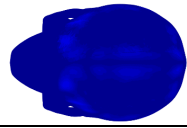
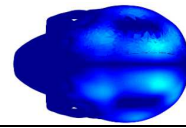
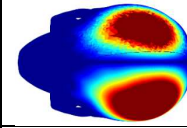
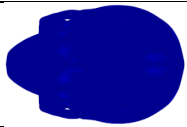
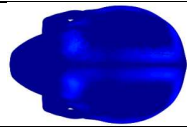
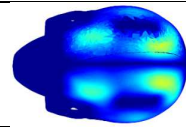
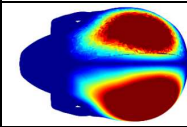
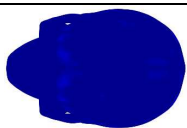
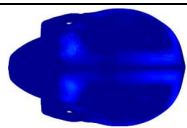
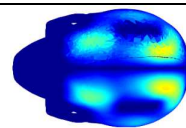
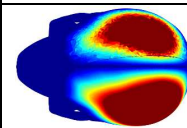
But, as can be seen in Table 5.5, a too low value of  $m$  could lead to worse results in those cases where the template is not able to adequately follow the defective model. In such cases, the coarse alignment between the MPs and the others interpolation centers can cause curvature discontinuities on the surface if  $m$  is too small, i.e. no sufficient distance is left between the boundary loop and the outer ring of the MPs. As said, this situation leads to the typical problems of *Template-based* approaches. For these reasons, an optimal value of  $m$  can be found only after an initial tuning of the parameter experimentally assessed on the defective model under consideration. However, it can be assumed that, according to the reported results, the optimal value of  $m$  falls between 10 and 25  $mm$  (see Tables 2.5 – 5.7). This could be seen as a limitation of the devised algorithm, but it must be considered that a *trial-and-error* approach is commonly exploited in RE methods to find the best parameters definition because usually there is not sufficient a priori information able to provide such parameters.

With reference to  $m = 80$ , the results clearly underline that the reconstruction obtained without considering the MPs (therefore following the typical *Surface interpolation-based* approach) leads to questionable reconstructions in all the cases addressed. This confirms that considering the MPs actually means an important improvement over the classic *Surface Interpolation-based* approach.

Regarding the  $n$  value, as already mentioned, the results show that it has little influence on the quality of the reconstruction. However, in all the case studies the reconstruction worsens slightly if  $n$  increases. Probably, a high value of  $n$  over-constrains the interpolating surface that is less able to adapt accurately to interpolation centers.

A further and more comprehensive assessment of the ability of the proposed algorithm to restore defective cranial vaults is provided in the following Sections.

**Table 5.4: The resulting  $AV$  and  $AV_{point}$  for TC#1**

TC#1	$m=10\text{ mm}$	$m=25\text{ mm}$	$m=40\text{ mm}$	$m=80\text{ mm}$
$n=10\text{ rings}$				
	$AV = 0.000\text{ mm}$	$AV = 0.058\text{ mm}$	$AV = 0.399\text{ mm}$	$AV = 2.043\text{ mm}$
$n=40\text{ rings}$				
	$AV = 0.000\text{ mm}$	$AV = 0.130\text{ mm}$	$AV = 0.611\text{ mm}$	$AV = 2.596\text{ mm}$
$n=70\text{ rings}$				
	$AV = 0.003\text{ mm}$	$AV = 0.125\text{ mm}$	$AV = 0.666\text{ mm}$	$AV = 2.600\text{ mm}$

**Table 5.5: The resulting  $AV$  and  $AV_{point}$  for TC#2**

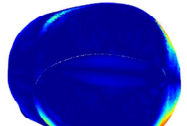
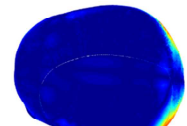
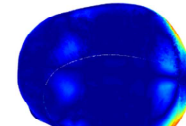
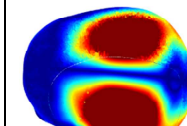
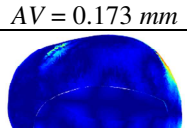
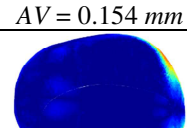
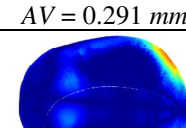
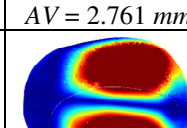
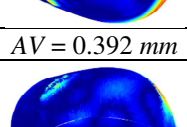
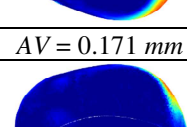
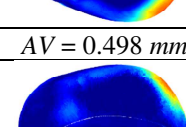
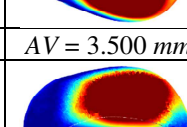
TC#2	$m=10\text{ mm}$	$m=25\text{ mm}$	$m=40\text{ mm}$	$m=80\text{ mm}$
$n=10\text{ rings}$				
	$AV = 0.173\text{ mm}$	$AV = 0.154\text{ mm}$	$AV = 0.291\text{ mm}$	$AV = 2.761\text{ mm}$
$n=40\text{ rings}$				
	$AV = 0.392\text{ mm}$	$AV = 0.171\text{ mm}$	$AV = 0.498\text{ mm}$	$AV = 3.500\text{ mm}$
$n=70\text{ rings}$				
	$AV = 0.533\text{ mm}$	$AV = 0.163\text{ mm}$	$AV = 0.503\text{ mm}$	$AV = 3.536\text{ mm}$



Table 5.6: The resulting  $AV$  and  $AV_{point}$  for TC#3

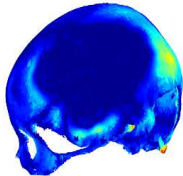
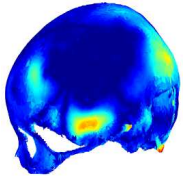
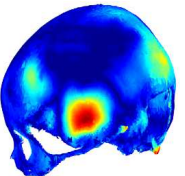
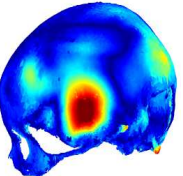
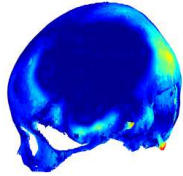
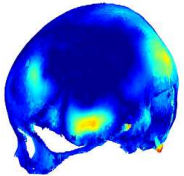
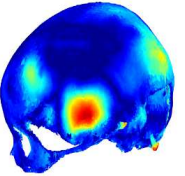
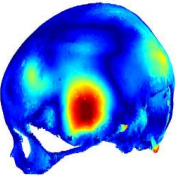
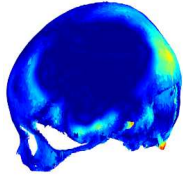
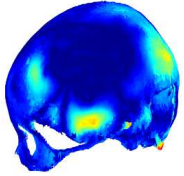
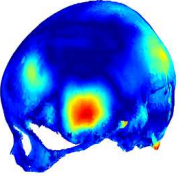
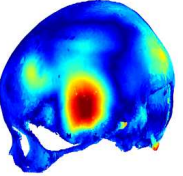
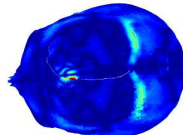
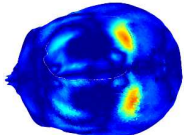
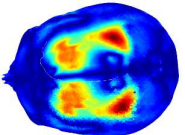
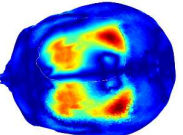
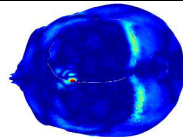
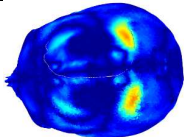
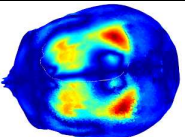
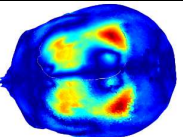
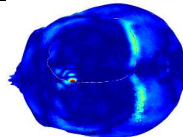
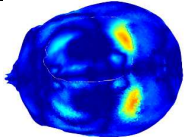
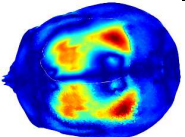
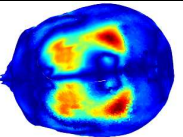
TC#3	$m=10\text{ mm}$	$m=25\text{ mm}$	$m=40\text{ mm}$	$m=80\text{ mm}$
$n=10\text{ rings}$				
	$AV = 0.144\text{ mm}$	$AV = 0.405\text{ mm}$	$AV = 0.710\text{ mm}$	$AV = 1.300\text{ mm}$
$n=40\text{ rings}$				
	$AV = 0.156\text{ mm}$	$AV = 0.431\text{ mm}$	$AV = 0.737\text{ mm}$	$AV = 1.277\text{ mm}$
$n=70\text{ rings}$				
	$AV = 0.163\text{ mm}$	$AV = 0.423\text{ mm}$	$AV = 0.718\text{ mm}$	$AV = 1.344\text{ mm}$

Table 5.7: The resulting  $AV$  and  $AV_{point}$  for TC#4

TC#4	$m=10\text{ mm}$	$m=25\text{ mm}$	$m=40\text{ mm}$	$m=80\text{ mm}$
$n=10\text{ rings}$				
	$AV = 0.144\text{ mm}$	$AV = 0.405\text{ mm}$	$AV = 0.710\text{ mm}$	$AV = 1.300\text{ mm}$
$n=40\text{ rings}$				
	$AV = 0.156\text{ mm}$	$AV = 0.431\text{ mm}$	$AV = 0.737\text{ mm}$	$AV = 1.277\text{ mm}$
$n=70\text{ rings}$				
	$AV = 0.163\text{ mm}$	$AV = 0.423\text{ mm}$	$AV = 0.718\text{ mm}$	$AV = 1.344\text{ mm}$

### 5.3. Evaluation of the proposed algorithm

Several test cases have been considered to evaluate the quality of the reconstruction carried out by means of the algorithm devised in this thesis. In this Section, the results of nine representative cases are reported. These nine test cases include five different skulls (see Table 5.8):

- TC#1, which is a complete and perfectly symmetric synthetic skull.
- TC#2, which is a real healthy skull.
- TC#3, TC#4 and TC#5, which are real defective skulls: TC#3 has a purely unilateral large defect, TC#4 has a defect which slightly crosses the *symmetry plane*, and TC#5 has a bilateral defect (i.e. one defect for each half).

For each of the complete skulls (TC#1 and TC#2), three different kinds of artificial defects are modeled: the first, named *A*, is purely unilateral, the second, named *B*, slightly crosses the *symmetry plane*, while the third, named *C*, is a bilateral defect.

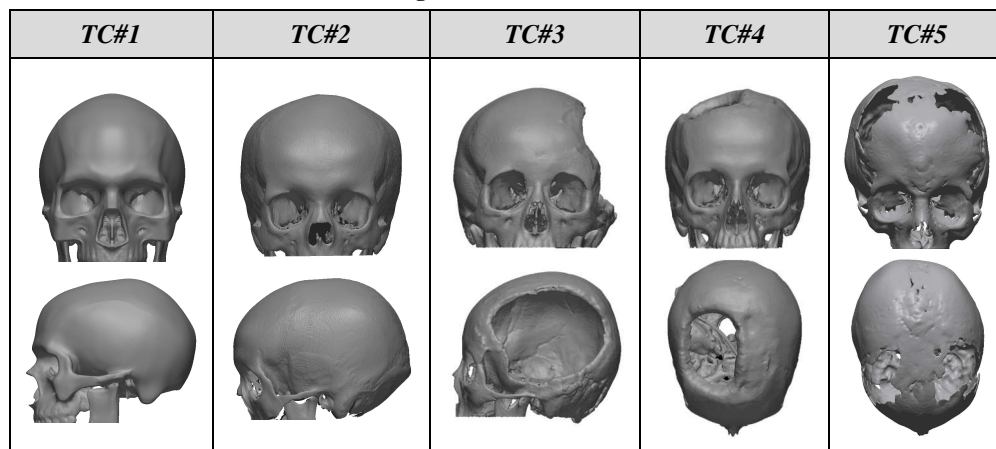
Being actually defected skulls, TC#3, TC#4 and TC#5 are not further modified.

In all the reported cases, the area of each defect (real or synthetic) is greater than 100 cm<sup>2</sup>, so they can be considered *large defects* [38].

According to Section 5.2, the procedure's inputs are imposed as follow:  $\bar{d}$  is imposed equal to 100 mm,  $m$  equal to 18 mm and  $n$  equal to 10 rings.

In particular, the  $m$  value is set equal to 18 mm after an initial tuning, because it has proved to be a compromise value between the quality of the reconstruction and the robustness of the procedure in all the cases addressed.

**Table 5.8: Starting models for the discussed test cases**



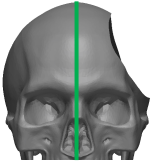
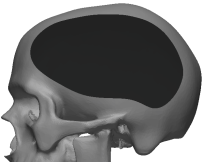
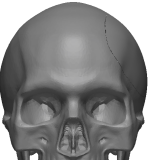
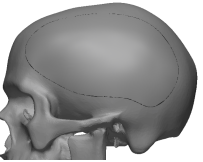
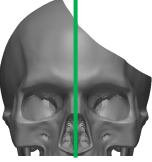
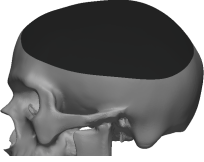
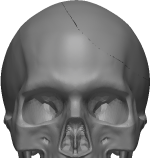
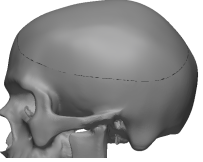
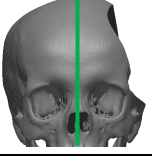


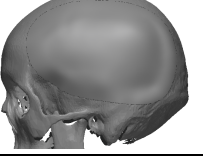
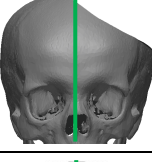
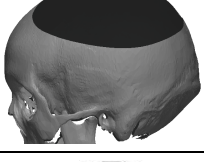
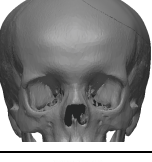
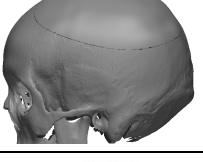
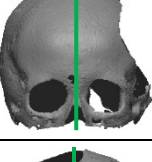
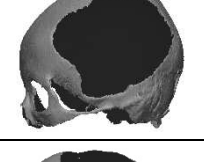
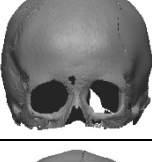
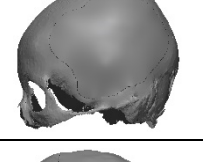
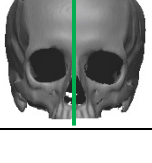



In the following, the results attained by the two reconstruction strategies described in Chapter 3 (i.e. for unilateral and non-unilateral cases) are discussed separately to evaluate the quality of the restoration provided by the proposed algorithm. Such evaluation is carried out by means of the *AV* index and the  $AV_{point}$  map with the aim to deliver a quantitative assessment of the algorithm's ability to reach a consistent reconstruction in terms of symmetry of the

resulting neurocranium and in terms of continuity between the patch and the surrounding healthy bone.

### 5.3.1. Unilateral Defects

The case studies presenting unilateral defects (i.e. defects that do not cross the *symmetry plane*) or quasi-unilateral defects (i.e. defects that slightly cross the *symmetry plane*) have been faced with a mirroring approach exploiting the *symmetry plane* automatically provided as explained in Section 4.2. The whole procedure followed to attain the reconstruction starting from the defective model is comprehensively reported in Chapter 3.

**Table 5.9: Unilateral or quasi-unilateral defects: algorithm outcomes**

<i>Test Case</i>	<i>Defective Frontal view</i>	<i>Defective Lateral view</i>	<i>Restored Frontal view</i>	<i>Restored Lateral view</i>
#1_A				
#1_B				
#2_A				
#2_B				
#3				
#4				

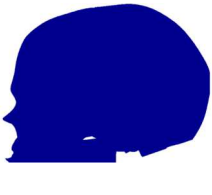
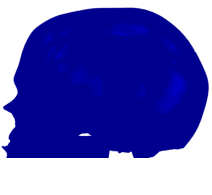


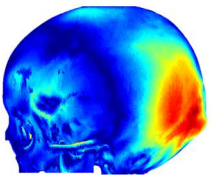
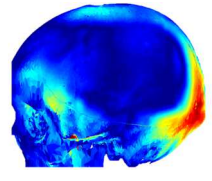
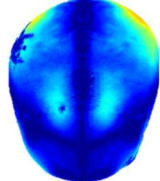
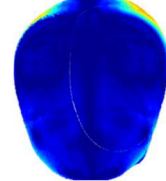
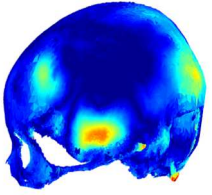
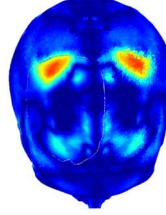
Among all the test cases tackled to evaluate the quality of the proposed procedure, the results of the six defective models depicted in Table 5.9 are discussed in detail in the following to assess the ability of the proposed algorithm to perform the reconstruction using the contralateral healthy half of the skull as a template to retrieve the MPs.

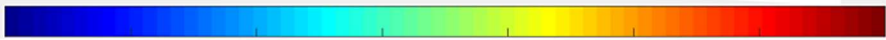
The discussed test cases are defined as described in Section 5.3.

**Table 5.10: AV values for all the unilateral and quasi-unilateral test cases discussed**

Test Cases	Undefective	Def A	Def B
#1	0.000 mm	0.000 mm	0.000 mm
#3	0.945 mm	0.614 mm	0.360 mm
#4	N.A.	0.574 mm	N.A.
#5	N.A.	N.A.	0.691 mm

**Table 5.11: AV<sub>point</sub> maps for the unilateral and quasi-unilateral test cases discussed**

TC	Defect Type: A		Defect Type: B	
	Complete	Reconstructed	Complete	Reconstructed
#1				
#2				
#3	N.A.		N.A.	N.A.
#4	N.A.	N.A.	N.A.	



0[mm]    1    2    3    4    5    6    7

Along with the defective models, Table 5.2 reports also the outcomes of the presented algorithm applied to the considered test cases with unilateral or quasi-unilateral defects.

Table 5.10 reports the  $AV$  values of the reconstructions showed in Table 5.2 (lower values of  $AV$  indicate a more symmetric skull). Table 5.10 shows that the proposed procedure provides reconstructed models with an  $AV$  even lower than the original ones, where the comparison is possible. Where the original shape was unknown (TC#3 and TC#4), the low value of  $AV$  still allows to demonstrate the “good” symmetry of the reconstruction and, consequently, allows a quantitative evaluation of the reconstruction acceptability.

The  $AV_{point}$  maps, reported in Table 5.11, also confirms the effectiveness of the reconstruction in terms of symmetry of the outcome as demonstrated by the larger dark blue areas in the reconstructed skulls compared to the originals. In addition, Table 5.11 shows the lack of any kind of discontinuities or asymmetries at the interface between healthy skull and reconstructive patch as evidenced by the absence of sudden color variations on the cranial surface.

### 5.3.2. Non-Unilateral Defects

The same evaluation approach followed for the unilateral and quasi-unilateral defects (based on the  $AV$  index and the  $AV_{point}$  map) has been applied to assess the non-unilateral defects reconstruction.

As explained in Section 5.3, three representative models, selected among all the test cases addressed, are discussed in detail in the following. The aim is to assess the quality of the reconstruction provided by the algorithm in the case of a bilateral defect, so by retrieving the MPs from the PSM (see Section 4.1.2).

The three models under consideration are reported in Figures 5.3(a) – 5.5(a) and described in Section 5.3 as test cases TC#1\_C, TC#2\_C and TC#5.

Along with the defective models to be reconstructed, Figures 5.3(b) – 5.5(b) and Figures 5.3(c) – 5.5(c) also show, respectively, the resulting PSM of each model (computed as described in Section 4.1.2) and the deviation map between each defective model (a) and its respective PSM (b). The deviation maps depict, point by point, the Euclidian distances measured between correspondent points. It is worth to underline that the deviation maps confirm the expected absolute mean error between the fitted SSM and the target model: in fact, as reported in Section 4.1.3, the expected error has been computed in about  $1.25 \pm 0.17$  mm, very close to the values measured in the reported cases (i.e., respectively, 1.43 mm, 1.21 mm and 1.58 mm).

The fitting errors shown in Figures 5.3(c) – 5.5(c) clearly demonstrate that performing the reconstruction by means of a typical *Template-based* approach (namely extrapolating from the PDM the whole points-set that falls into the boundary loop) can lead to a distance up to 2.5 mm between the outer rim of the reconstructed patch and the edge of the surrounding bone.

This results in a lack of continuity between patch and bone which must be fixed by the operator through a series of manual time-consuming and cumbersome operations: as widely discussed in Chapter 2, this actually represents the main limitation of the *Template-based* methods.

On the contrary, performing the reconstruction by means of the proposed algorithm enables to overcome these shortcomings: Figures 5.3(d) – 5.5(d) and Figures 5.3(e) – 5.5(e) show, respectively, the reconstruction provided by the devised algorithm and the deviation maps between each defective model (a) and the reconstructed model (d).

In particular, Figures 5.3(c) – 5.5(c) show that the reconstruction is perfectly superimposed on the known part of the skull to be reconstructed: by retrieving the BPs and  $n$ -RNs directly from the defective model, the algorithm is able to provide a restored cranial vault that perfectly matches the actual model to be reconstructed without requiring time-consuming manual operations.

Dealing with the quantitative assessment of the reconstruction it is performed, again, according to the  $AV$  index and the  $AV_{point}$  map. For the discussed test cases with non-unilateral defects, the computed  $AV$  index is reported in Table 5.12. The results show that exploiting an external source as a template cannot ensure reconstructed models with an  $AV$  even lower than the original ones, as was the case in the *mirroring-based* reconstruction (see Table 5.10). While a reconstruction driven by the contralateral part leads obviously to a maximization of the similarity of the two halves, there are no constraints able to ensure the symmetry when the external template is exploited to retrieve the MPs.

Despite that, where the comparison is possible (i.e., for TC#1\_C and TC#2\_C)  $AV$  shows a value for the restored skulls very close to that of the originally known shapes, proving the effectiveness of the reconstruction provided by the algorithm.

As regards test case #5, whose original shape is not known, the reconstruction achieves an  $AV$  index comparable with the  $AV$  computed for the undefective real model TC#2. That allows demonstrating the ability of the procedure to deliver consistent results.

In addition, the  $AV_{point}$  maps reported in Table 5.13 show the lack of any kind of discontinuities or asymmetries at the interface between healthy skull and reconstructive patch for all the three test cases.

As a consequence, both  $AV$  and  $AV_{point}$  prove the effectiveness of the delivered reconstruction.

**Table 5.12:  $AV$  values for all the unilateral test cases discussed**

<i>Test Cases</i>	<i>Undefective</i>	<i>Def C</i>
#1_C	0.000 mm	0.003 mm
#2_C	0.945 mm	1.130 mm
#5	N.A.	1.326 mm

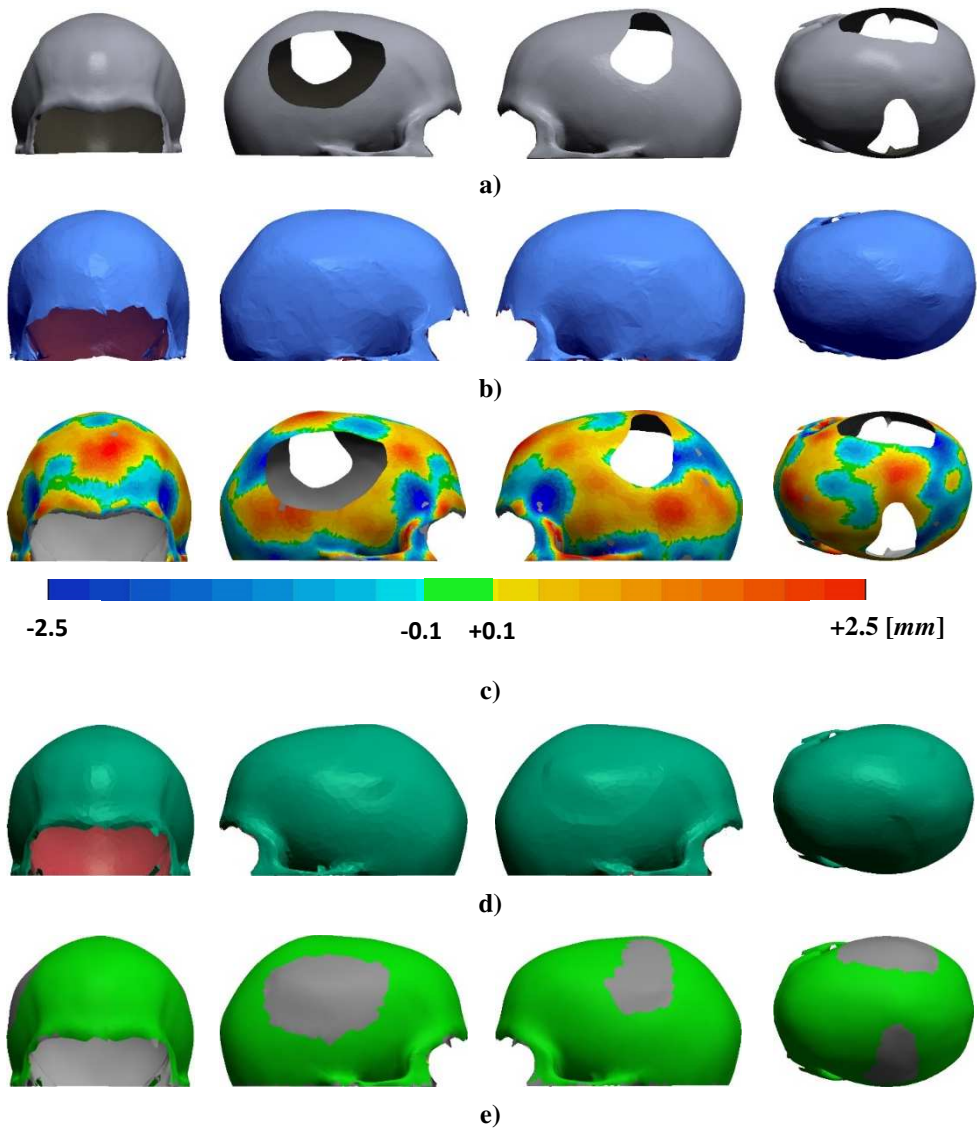


Figure 5.1: Test Case #1\_C – a) The defective model; b) The Posterior model; c) Deviation map between a) and b); d) The reconstruction provided by the proposed algorithm; e) Deviation map between d) and a)

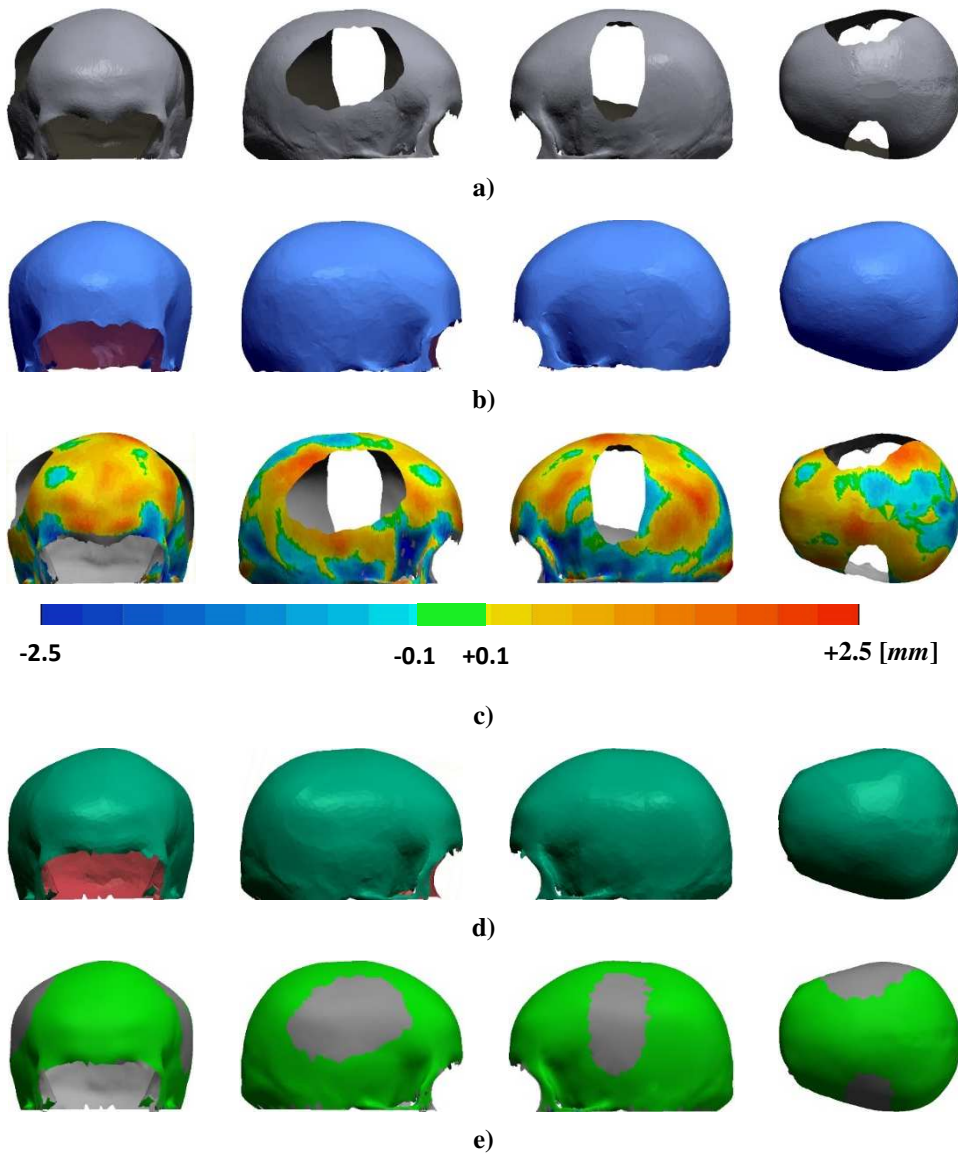
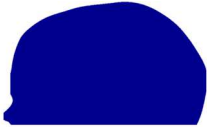

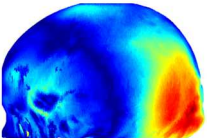
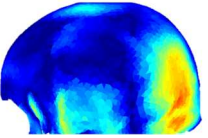
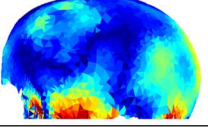



Figure 5.2: Test Case #2\_C – a) The defective model; b) The Posterior model; c) Deviation map between a) and b); d) The reconstruction provided by the proposed algorithm; e) Deviation map between d) and a)





**Table 5.13:  $AV_{point}$  maps for the non-unilateral test cases discussed**

TC	Defect Type: C	
	Complete	Reconstructed
#1		
#2		
#5	N.A.	



0mm    1    2    3    4    5    6    7

### 5.3.3. Comparison of results with commercial software

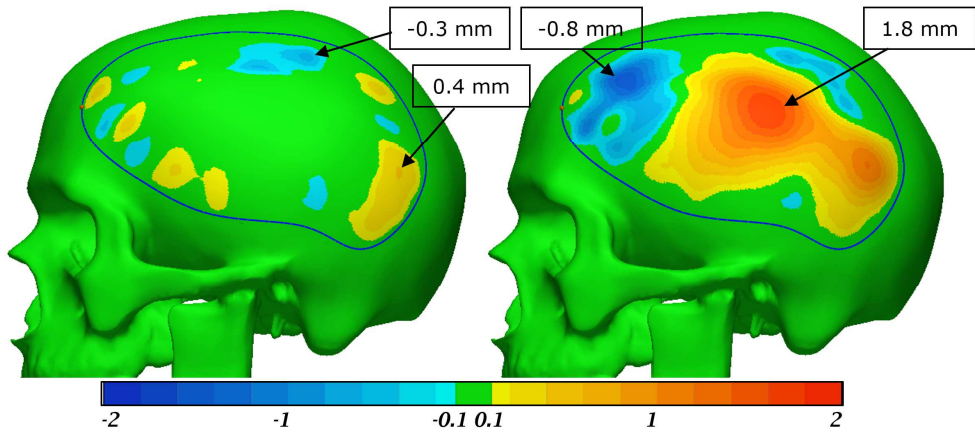
In order to perform a further assessment of the proposed procedure, a direct comparison between the reconstructed cranial vault and a properly designed reference skull has been also performed. To obtain reliable results, such reference shape must be able to minimize all the possible variables that could affect the final assessment, such as the natural asymmetry of a real cranial vault shape. For this aim, TC#1 has been chosen as test case: thanks to its perfect symmetry, this model allows to avoid all the external factors that could affect the reconstruction, limiting the evaluation only to the specific behavior of the developed procedure. Consequently, specifically for TC#1 the closer the reconstructed surface gets to the original shape, the better the reconstruction will be.

Figure 5.4 and Figure 5.5 show such a comparison in terms of mesh deviation between the starting model and the reconstructed one for, respectively, cases #1\_A and #1\_B. The reconstruction has been carried out both using the presented procedure (Figure 5.4(a) and Figure 5.5(a)) and the hole-filling tool provided by Geomagic® Design X (Figure 5.4(b) and Figure 5.5(b)).

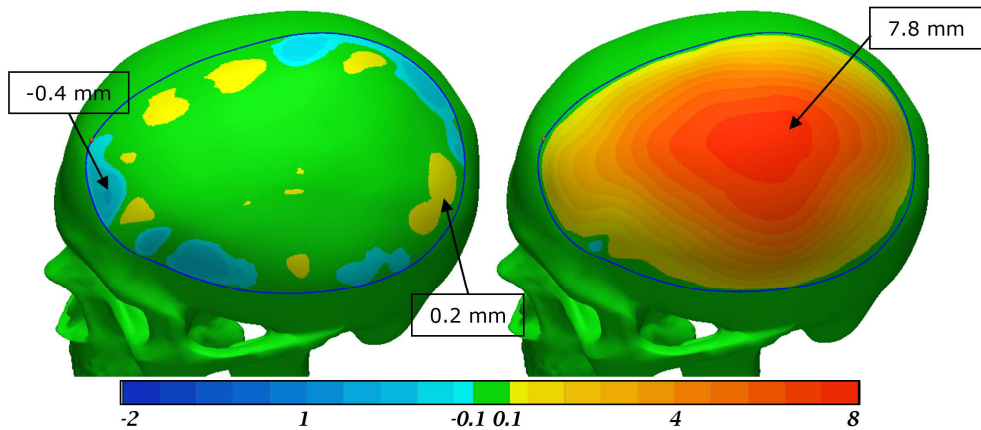
The procedure's inputs value (i.e.  $\bar{d}$ ,  $m$  and  $n$ ) are defined as explained above.

As expected, the reconstruction achieved by adding the MPs yields a shape very close to the original model, providing a better outcome than the one obtained by Design X and guided only by the BPs.

As shown in Figure 5.4(a) and Figure 5.5(a), the deviation in the middle of the hole, where the reconstruction is driven by the MPs, is about 0 mm, while the reconstructed surface deviates slightly (max 0.4 mm) from the reference in the area close to the edge. In this area, the MPs are not considered to ensure a better continuity at the defect's edge when the perfect symmetry of the cranial vault is not verified, that means in all the real cases.



**Figure 5.4:** TC#1\_A – The comparison between the complete symmetric synthetic skull and the reconstructed carried out by (a) the proposed method and (b) the hole-filling tool provided by using Geomagic® Design X



**Figure 5.5:** TC#1\_B – The comparison between the complete symmetric synthetic skull and the reconstructed carried out by (a) the proposed method and (b) the hole-filling tool provided by using Geomagic® Design X

Considering all the evaluations discussed in this Chapter, it can be concluded that the proposed algorithm is able to automatically provide an aesthetically consistent outcome ensuring both mathematical continuity at the boundary of the defect and an acceptable symmetric reconstruction.

This consistent reconstruction is guaranteed both for unilateral defects and for non-unilateral defects.



## 6. Conclusions and final remarks

The increasingly powerful and specialized CAx tools for handling complex geometries, such as anatomical ones, are representing breakthrough for clinical practice. Especially in Cranioplasty, the capability to make reliable simulations as well as to design the actual implant at preoperative stage using the patient's own diagnostic images has proved to be worthwhile, both in terms of effectiveness and costs.

To date, one of the toughest tasks in the Cranioplasty surgery is the pre-operative virtual design of a corrective cranial plate. To ensure an acceptable aesthetical and functional outcome, such a design must be based on a proper anatomical reconstruction usually done in virtual environments by skilled operators.

Several techniques have been developed for the cranial vault digital reconstruction, but all of them share some drawbacks that limit their applicability (e.g. too complex or time-consuming operations or incorrect resulting geometries). The limitations are mainly related to the lack of information in the missing area and the complexity of the shape that must be restored.

In order to overcome these drawbacks, a novel hole-filling procedure for the restoration of defective cranial vaults has been presented in this thesis. The procedure is suited for both unilateral and non-unilateral large defects.

The procedure works automatically starting from the external poly-faces of the defective neurocranium, leaving to the user only the selection of the hole to be repaired by clicking one point on its edge. Being landmark-independent and avoiding any patch adaptation, the developed procedure represents a valid alternative for the existing approaches in terms of user's burden, requiring less time consuming and less cumbersome operations.

The innovative idea is to exploit a properly defined template to obtain some meaningful points (named MPs) in the missing or deformed region, with the aim to guide the subsequent reconstruction carried out by a *Surface Interpolation-based* technique.

This approach enables to overcome the shortcomings of the typical *Surface Interpolation-based* technique, which usually leads to non-consistent shape: usually, the reconstructed patch results too flat due to the lack of centers of interpolation inside the defect region able to guide the reconstruction.

In the devised approach, the missing information is retrieved from a template able to deliver a shape prediction of the region to restore. The aim is to perform a data-driven interpolation through the whole region to be reconstructed.

Two different kinds of templates are defined in this thesis, depending on whether the defective skull has a unilateral or a non-unilateral defect.

In the former case, the patient own data is exploited by mirroring the healthy half on the defective one. The plane around which perform the mirroring is automatically provided by means of an original algorithm developed during the Ph.D. in collaboration with Prof. Luca Di Angelo and Prof. Paolo Di Stefano from the University of L'Aquila.

When a healthy half is not available (i.e., in the case of non-unilateral defects), an external source is used as a template, i.e. a Statistical Shape Model which has been specifically built in this thesis. A Statistical Shape Model is a statistical representation of the shape under consideration (namely, the cranial vault), capable of deforming to match the known regions of the model to be reconstructed. In addition, the SSM can be used to infer the full shape of the anatomy starting from the partially known model. This approach leads to a *posterior distribution*, that describes the more likely full shape exploiting the prior knowledge provided by the healthy part of the cranial vault.

A procedure able to ensure a reliable automatic construction of the SSM starting from a training set of significant healthy ROI has been proposed. Not requiring any manual operation, the number of samples in the training set can be increased at will, without time-consuming or heavy and tedious operations required of the user. Therefore, this allows to have a training set with a larger population and, consequently, a more precise template for improving the ability to reproduce the wide interpersonal variability of the anatomical structures.

Several case studies have been faced to assess the effectiveness and reliability of the devised procedure. Since the quality of the reconstruction is strictly related to the aesthetical outcome, a new evaluation method has been developed to evaluate the quality of the procedure considering those criteria that mainly affect the aesthetics. These criteria are the symmetry of the resulting skull and the continuity between the reconstructed patch and the surrounding bone.

According to the proposed evaluation method, the case studies addressed show that the novel procedure leads to a consistent aesthetic outcome, both in the case of unilateral and non-unilateral defects.

In addition, the test cases confirm that the reconstruction driven by the MPs enables to overcome the limitations of both the *Surface Interpolation-based* and the *Template-based* techniques, ensuring the skull surface continuity and the resulting shape consistency without time-consuming user's operation.

Dealing with the computational time starting from the properly modified STL, it is closely related to the resolution of the surface model (number of vertices forming the STL file). For the addressed test cases, the computational time resulting to be between 5 and 10 minutes for point sets from 4,000 to 10,000. The algorithm is tested with CPU Intel® Core™ i7-4712HQ/2.3 GHz and RAM 16 GB. The slower step to be carried out is the *symmetry plane* definition, which requires at least 80% of the total computational burden.

Considering the specific procedure devised in this thesis, several aspects to be improved can be identified.

The proposed approach is specially developed for the cranial vault. Because of the high complexity of the anatomy structures, it is difficult to provide a methodology reliable for all applications. Despite that, the possibility to extend the applicability of the proposed approach to other anatomies could be worthy of further investigations.

In addition, future developments could regard the application of the devised algorithm to reconstruct missing areas from incomplete acquired 3D data in other fields, such as cultural

heritage or industrial ones. From this point of view, the proposed approach could represent a powerful tool to be included in the traditional RE process.

Future work should also concern the optimization of the whole procedure, to make it more robust given the wide variability of the input models. In order to improve the applicability of the procedure by making it fully automatic, future efforts must concern the pre-processing steps like, for instance, the diagnostic images segmentation and the subsequent preparation of the STL (cleaning the model and isolating the cranial vault).

Further work should also be addressed to the improvement of the SSM, expanding the training set to increase its ability to match the defective model and to provide a more consistent PDM. As discussed in the relative Section, a promising approach to overcome the lack of availability of 3D anatomical models of healthy ROI involves exploiting the mathematical framework of the *Gaussian Processes* to mathematically model shape variations. By using analytically defined covariance functions, it is possible to build significant priors to enlarge the training set and consequently to increase the accuracy of the resulting parametric model.

According to this approach, it is possible to mathematically constrain the possible deformation of the SSM so that the resulting skull would be as symmetrical as possible. This allows to maximize the symmetry and, therefore, the effectiveness of the reconstruction.





## Bibliography

- [1] Tarsitano, A.; Battaglia, S.; Crimi, S.; Ciocca, L.; Scotti, R.; Marchetti, C.: Is a computer-assisted design and computer-assisted manufacturing method for mandibular reconstruction economically viable?, *Journal of Cranio-Maxillo-Facial Surgery*, 44(7), 2016, 795-799
- [2] Rogers-Vizena, C.R.; Sporn, S.F.; Daniels, K.M.; Padwa, B.L.; Weinstock, P.: Cost-Benefit Analysis of Three-Dimensional Craniofacial Models for Midfacial Distraction: A Pilot Study, *The Cleft Palate–Craniofacial Journal*, 54(5), 2017, 612-617.
- [3] Volpe, Y.; Furferi, R.; Governi, L.; Uccheddu, F.; Carfagni, M.; Mussa, F.; Scagnet, M.; Genitori, L.: Surgery of complex craniofacial defects: A single-step AM-based methodology, *Computer Methods and Programs in Biomedicine*, 165, 2018, 225-233
- [4] Bartalucci, C.; Furferi, R.; Governi, L.; Volpe, Y.: A Survey of Methods for Symmetry Detection on 3D High Point Density Models in Biomedicine, *Symmetry* 10(7), 2018
- [5] Martelli, N.; Serrano, C.; van den Brink, H.; Pineau, J.; Prognon, P.; Borget, I.; El Batti, S.: Advantages and disadvantages of 3-dimensional printing in surgery: a systematic review, *Surgery*, 159 (6), 2016, 1485-1500
- [6] Martini, M.; Klausning, A.; Messing-Jünger, M.; Lüchters, G.: The self-defining axis of symmetry: A new method to determine optimal symmetry and its application and limitation in craniofacial surgery, *Journal of Cranio-Maxillofacial Surgery*, 45(9), 2017, 1558-1565
- [7] Meyer-Marcotty, P.; Alpers, G.W.; Gerdes, A. B. M.; Stellzig-Eisenhauer, A.: Impact of facial asymmetry in visual perception: A 3-dimensional data analysis, *American Journal of Orthodontics and Dentofacial Orthopedics*, 137, 2010, 168.e1–168.e8
- [8] Grammar, K.; Thornhill, R.: Human facial attractiveness and sexual selection: The role of averageness and symmetry, *Journal of Comparative Psychology* 108(3), 1994, 233–242
- [9] Gangestad, S.W.; Thornhill, R.; Yeo, R.A.: Facial attractiveness, developmental stability, and fluctuating asymmetry, *Ethology and Sociobiology* 15(2), 1994, 73–85
- [10] Aydin, S.; Kucukyuruk, B.; Abuzayed, B.; Aydin, S.; Sanus, G. Z.: Cranioplasty: Review of materials and techniques, *Journal of Neurosciences in Rural Practice*, 2(2), 2011, 162-167

- [11] Girod, S.; Teschner, M.; Schrell, U.; Kevekordes, B.; Girod, B.: Computer-aided 3D simulation and prediction of craniofacial surgery: a new approach, *Journal of Cranio-Facial Surgery*, 29(3), 2001, 156-158
- [12] Maravelakis, E.; David, K.; Antoniadis, A.; Manios, A.; Bilalis, N.; Papaharilaou, Y.: Reverse engineering techniques for cranioplasty: A case study, *Journal of Medical Engineering and Technology*, 32(2), 2008, 115-121
- [13] Buonamici, F.; Furferi, R.; Genitori, L.; Governi, L.; Marzola, A.; Mussa, F.; Volpe, Y.: Reverse engineering techniques for virtual reconstruction of defective skulls: An overview of existing approaches, *Computer-Aided Design and Applications* 16(1), 2018, 103-112
- [14] Fuessinger, M. A.; Schwarz, S.; Cornelius, C.-P.; Metzger, M. C.; Ellis, E.; Probst, F.; Semper-Hogg, W.; Gass, M.; Schlager, S.: Planning of skull reconstruction based on a statistical shape model combined with geometric morphometrics, *International Journal of Computer Assisted Radiology and Surgery*, 13(4), 2018, 519-529
- [15] Penton-Voak, I.S.; Jones, B.C.; Little, A.C.; Baker, S.; Tiddeman, B.; Burt, D.M.; Perrett, D.I.: Symmetry, sexual dimorphism in facial proportions and male facial attractiveness, *Proceedings of the Royal Society Biological Sciences*, 268 (1476), 2001, 1617-1623
- [16] Cootes, T.F.; Taylor, C.J.; Cooper, D.H.; Graham, J.: Active Shape Models-Their Training and Application, *Computer Vision and Image Understanding* 61(1), 1995, 38-59
- [17] Cootes, T.F.; Edwards, G.J.; Taylor, C.J.: Active appearance models, *IEEE Transactions on Pattern Analysis and Machine Intelligence*, 23(6), 2001, 681-685
- [18] Blanz, V.; Vetter, T.: A morphable model for the synthesis of 3D faces, in: *SIGGRAPH '99*, 1999, 187-194, ACM press
- [19] Hierl, T.; Wollny, G.; Schulze, F. P.; Scholz, E.; Schmidt, J. G.; Berti, G.; Hendricks, J.; Hemprich, A.: CAD-CAM Implants in Esthetic and Reconstructive Craniofacial Surgery, *Journal of Computing and Information Technology*, 14(1), 2006, 65-70
- [20] Marreiros, F. M. M.; Heuzé, Y.; Verius, M.; Unterhofer, C.; Freysinger, W.; Recheis, W.: Custom implant design for large cranial defects, *International Journal of Computer Assisted Radiology and Surgery*, 11(12), 2016, 2217-2230
- [21] Möller, T.; Trumbore, B.: Fast, minimum storage ray-triangle intersection, *Journal of Graphics Tools*, 2(1), 1997, 21-28
- [22] Dean, D.; Min, K.-J.; Bond, A.: Computer Aided Design of Large-Format Prefabricated Cranial Plates, *Journal of Craniofacial Surgery*, 14(6), 2003, 819-8322
- [23] Dean, D.; Min, K. J.: Deformable templates for preoperative computer-aided design and fabrication of large cranial implants, *International Congress Series*, 1256(C), 2003, 710-715
- [24] Wu, T.; Engelhardt, M.; Fieten, L.; Popovic, A.; Radermacher, K.: Anatomically constrained deformation for design of cranial implant: methodology and validation,

- Medical Image Computing and Computer Assisted Interventions, 9(1), 2006, 9–16
- [25] Linney, A. D.; Tan, A. C.; Richards, R.; Gardener, J.; Grindrod, S.; Moss, J. P.: Three-dimensional visualization of data on human anatomy: diagnosis and surgical planning, *Journal of Audiovisual Media in Medicine*, 16(1), 1993, 4–10
- [26] Fantini, M.; de Crescenzo, F.; Persiani, F.; Benazzi, S.; Gruppioni, G.: 3D restitution, restoration and prototyping of a medieval damaged skull, *Rapid Prototyping Journal*, 14(5), 2008, 318–324
- [27] Alonso-Rodriguez, E.; Cebrián, J. L.; Nieto, M.J.; Del Castillo, J.L.; Hernández-Godoy, J.; Burgueño, M.: Polyetheretherketone custom-made implants for craniofacial defects: Report of 14 cases and review of the literature, *Journal of Cranio-Maxillofacial Surgery*, 43(7), 2015, 1232-1238
- [28] Chen, X.; Xu, L.; Li, X.; Egger, J.: Computer-aided implant design for the restoration of cranial defects, *Scientific Reports*, 7, 2017, 4199
- [29] Gall, M.; Li, X.; Chen, X.; Schmalstieg, D.; Egger, J.: Computer-Aided Planning and Reconstruction of Cranial 3D Implants, *IEEE Engineering in Medicine and Biology Society*, 2016, 1179–1183
- [30] Jardini, A. L.; Larosa, M. A.; Filho, R. M.; de Carvalho Zavaglia, C. A.; Bernardes, L. F.; Lambert, C. S.; Calderoni, D. R.; Kharmandayan, P.; Cranial reconstruction: 3D biomodel and custom-built implant created using additive manufacturing, *Journal of Cranio-Maxillofacial Surgery*, 42(8), 2014, 1877-1884
- [31] Lee, M. Y.; Chang, C. C.; Lin, C. C.: Custom implant design for patients with cranial defects, *IEEE Engineering in Medicine and Biology Magazine*, 21(2), 2002, 38-44
- [32] Li, X.; Yin, Z.; Wei, L.; Wan, S.; Yu, W.; Li, M.: Symmetry and template guided completion of damaged skulls, *Computers & Graphics*, 35(4), 2011, 885-893
- [33] Wagner, M. E. H.; Lichtensteiner, J. T.; Winkelmann, M.; Shin, H.; Gellrich, N. C.; Essig, H.; Development and first clinical application of automated virtual reconstruction of unilateral midface defects, *Journal of Cranio-Maxillofacial Surgery*, 43(8), 2015, 1340-1347
- [34] Di Angelo, L.; Di Stefano, P.: A computational Method for Bilateral Symmetry Recognition in Asymmetrically Scanned Human Faces, *Computer-Aided Design and Applications*, 11(3), 2013, 275-283
- [35] Egger, J.; Gall, M.; Tax, A.; Ücal, M.; Zefferer, U.; Li, X.; von Campe, G.; Schafer, U.; Schmalstieg, D.; Chen, X.: Interactive reconstructions of cranial 3D implants under MeVisLab as an alternative to commercial planning software, *PLoS ONE*, 12(3), 2017, Article Number e0172694
- [36] Carr, J. C.; Fright, W. R.; Beatson, R. K.: Surface interpolation with radial basis functions for medical imaging, *IEEE Transactions on Medical Imaging*, 16(1), 1997, 96–107
- [37] Zhou, L.; Song, Y.; Wu, J.; Li, H.; Zhang, G.; Sun, C.: Surface reconstruction of bilateral skull defect prosthesis based on radial basis function, *Informatics and Management Science I, Lecture Notes in Electrical Engineering*, Springer-Verlag,

- London, 2013
- [38] Chong, C. S.; Lee, H.; Kumar, A. S.: Automatic Hole Repairing for Cranioplasty using Bézier Surface Approximation, *Journal of Craniofacial Surgery*, 17(2), 2006, 344–352
  - [39] Jiang, L.; Ma, X.; Lin, Y.; Yu, L.; Ye, Q.: Craniofacial Reconstruction Based on MLS Deformation, *Wseas Transactions On Computers*, 9(7), 758-767
  - [40] Chen, J. J.; Liu, W.; Li, M. Z.; Wang, C. T.: Digital manufacture of titanium prosthesis for cranioplasty, *International Journal of Advanced Manufacturing Technology*, 27(11-12), 2006, 1148–1152
  - [41] Van der Meer, W. J.; Bos, R. R. M.; Vissink, A.; Visser, A.: Digital planning of cranial implants, *British Journal of Oral and Maxillofacial Surgery*, 51(5), 2013, 450-452
  - [42] Rudek, M.; Canciglieri Junior, O.; Greboge, T.: A PSO application in skull prosthesis modelling by superellipse, *Electronic Letters on Computer Vision and Image Analysis*, 12(2), 2013, 1–12
  - [43] Liao, Y.-L.; Lu, C.-F.; Sun, Y.-N.; Wu, C.-T.; Lee, J.-D.; Lee, S.-T.; et al.: Three-dimensional reconstruction of cranial defect using active contour model and image registration, *Medical & Biological Engineering & Computing*, 49(2), 2011, 203–211
  - [44] Liao, Y. L.; Lu, C. F.; Wu, C. T.; Lee, J. D.; Lee, S. T.; Sun, Y. N.; Wu, Y. N.: Using three-dimensional multigrid-based snake and multiresolution image registration for reconstruction of cranial defect, *Medical and Biological Engineering and Computing*, 51(1-2), 2013, 89–101
  - [45] Chen, Y. W.; Shih, C. T.; Cheng, C. Y.; Lin, Y. C.: The Development of Skull Prosthesis Through Active Contour Model, *Journal of Medical Systems*, 41(10), 2017, Article Number 164
  - [46] Lin, Y. C.; Cheng, C. Y.; Cheng, Y. W.; Shih, C. T.: Skull Repair Using Active Contour Models, *Procedia Manufacturing*, 11, 2017, 2164-2169
  - [47] Canciglieri, O.; Rudek, M.; Greboge, T.: A prosthesis design based on genetic algorithms in the concurrent engineering context, *Improving Complex Systems Today*, Springer-Verlag, London, 2011
  - [48] Zhang, Z.; Zhang, R.; Song, Z.: Skull defect reconstruction based on a new hybrid level set, *Bio-Medical Materials and Engineering*, 24(6), 2014, 3343–3351
  - [49] Gelaude, F.; Vander Sloten, J.; Lauwers, B.: Automated Design and Production of Cranioplasty Plates: Outer Surface Methodology, Accuracies and a Direct Comparison to Manual Techniques, *Computer-Aided Design and Applications*, 3(1-4), 2006, 193–202
  - [50] Hsu, J. H.; Tseng, C. S.: Application of three-dimensional orthogonal neural network to craniomaxillary reconstruction, *Computerized Medical Imaging and Graphics*, 25(6), 2001, 477-482
  - [51] Di Angelo, L.; Di Stefano, P.: A new Method for the Automatic Identification of the Dimensional Features of Vertebrae, *Computers Methods and Programs in Biomedicine*, 121(1), 2015, 36-48

- [52] Di Angelo, L.; Di Stefano, P.; Bernardi, S.; Continenza, M. A.: A new computational Method for Automatic Dental Measurement: The case of maxillary central incisor, *Computers in Biology and Medicine*, 70(1), 2016, 202-209
- [53] Gelaude, F.; Vander Sloten, J.; Lauwers, B.: Automated Design and Production of Cranioplasty Plates: Outer Surface Methodology, Accuracies and a Direct Comparison to Manual Techniques, *Computer-Aided Design and Applications*, 3(1-4), 2006, 193–202
- [54] Kendall, D.G.: Shape Manifolds, Procrustean Metrics, and Complex Projective Spaces. *Bulletin of the London Mathematical Society*, 16 (2), 1984, 81–121
- [55] Neumann A.; Lorenz C.: Statistical shape model-based segmentation of medical images, *Computerized Medical Imaging and Graphics*, 22 (2), 1998, 133–143
- [56] Heimann, T.; Meinzer, H.P.: Statistical shape models for 3D medical image segmentation: A review, *Medical Image Analysis*, 13(4), 2009, 543-563
- [57] Bookstein, F.L.: Landmark methods for forms without landmarks: morphometrics of group differences in outline shape. *Medical Image Analysis*, 1(3), 1997, 225-243
- [58] Cootes, T.F.; Taylor, C.J.; Cooper, D.H.; Graham, J.: Training Models of Shape from Sets of Examples. In: Hogg, D., Boyle, R. (eds) *BMVC92*, Springer, London, 1992
- [59] Kendal, D.G.: A survey of the statistical theory of shape, *Statistical Science*, 4(2), 1989, 87-120.
- [60] Bookstein, F.L.: *Morphometric Tools for landmark data*, Cambridge University Press, 2003
- [61] Heimann, T., et al.: Comparison and evaluation of methods for liver segmentation from CT datasets. *IEEE Transactions Medical Imaging*, 28(8), 2009,1251-1265
- [62] Cerveri, P., Belfatto, A., Manzotti, A.: Pair-wise vs group-wise registration in statistical shape model construction: representation of physiological and pathological variability of bony surface morphology. *Computer Methods in Biomechanics and Biomedical Engineering*, 22(7), 2019, 772-787
- [63] Amenta, N.; Bern, M.; Kamvysselis, M.: A new voronoi-based surface reconstruction algorithm, *Proceedings of the 25th Annual Conference on Computer Graphics and Interactive Techniques, SIGGRAPH*, 1998, 415-422
- [64] Audenaert E. A., et al.: Cascaded Statistical Shape Model Based Segmentation of the Full Lower Limb in CT, *Computer Methods in Biomechanics and Biomedical Engineering*, 22 (6), 2019, 644–657
- [65] Fuessinger M., et al.: Virtual reconstruction of bilateral midfacial defects by using statistical shape modeling, *Journal of Cranio-Maxillofacial Surgery*, 47 (7), 2019, 1054–1059
- [66] Semper-Hogg W.; et al.: Virtual Reconstruction of Midface Defects Using Statistical Shape Models, *Journal of Cranio-Maxillofacial Surgery*, 45, 2017, 461–466

- [67] Mendoza C. S.; Safdar N.; Okada K.; Myers E.; Rogers G. F.; George M.: Personalized Assessment of Craniosynostosis Via Statistical Shape Modeling, *Medical Image Analysis*, 18, 2014, 635–646.
- [68] Keustermans W.; et al.: High Quality Statistical Shape Modelling of the Human Nasal Cavity and Applications, *Royal Society Open Science*, 5, 2018
- [69] Lynch J. T.; et al.: Statistical Shape Modelling Reveals Large and Distinct Subchondral Bony Differences in Osteoarthritic Knees, *Journal of Biomechanics*, 93, 2019, 177–184.
- [70] Bookstein, F. L.: Size and Shape Spaces for Landmark Data in Two Dimensions, *Statistical Science*, 1(2), 1986, 181-222.
- [71] Jolliffe, I.T.: *Principal Component Analysis*. 2nd edn. Springer, 2002
- [72] Van Kaick O.; Zhang H.; Hamarneh G.; Cohen-Or D.: A survey on shape correspondence, in: *Computer Graphics Forum*, Wiley Online Library, 30, 2011, 1681–1707
- [73] Besl P. J.; McKay N. D.: A Method for Registration of 3-D Shapes, *IEEE Transactions on Pattern Analysis and Machine Intelligence*, 14 (2), 1992, 239–256
- [74] Chen Y.; Medioni G.: Object Modeling by Registration of Multiple Range Images, *Image and Vision Computing*, 10 (3), 1992, 145–155
- [75] Myronenko A.; Song X.: Point Set Registration: Coherent Point Drift, *IEEE Transactions on Pattern Analysis and Machine Intelligence*, 32 (12), 2010, 2262–2275.
- [76] Vos, F.M.; de Bruin, P.W.; Aubel, J.C.M.; Streekstra G.J.; Maas, M.; van Villet, L.; Vossepoel, A.: A statistical shape model without using landmarks, in: *ICPR 2004*, 3, IEEE, 2004
- [77] Brett, A.D; Taylor, C.J.: A Method of Automated Landmark Generation for Automated 3D PDM Construction, *Image and Vision Computing*, 18(9), 1999, 739-748
- [78] Möller, T.; Trumbore, B.: Fast, minimum storage ray-triangle intersection, *Journal of Graphics Tools*, 2(1), 1997, 21-28
- [79] Marzola, A.; Governi, L.; Genitori, L.; Mussa, F.; Volpe, Y.; Furferi, R.: A Semi-Automatic Hybrid Approach for Defective Skulls Reconstruction. *Computer-Aided Design and Applications*, 17(1), 2019, 190-204
- [80] Carr, J.C.; Beatson, R.K.; Cherrie, J.B.; Mitchell, T.J.; Fright, W.R.; McCallum, B.C.; Evans, T.R.: Reconstruction and representation of 3D objects with radial basis functions, in: *SIGGRAPH '01*, 67-76, ACM press, 2001
- [81] Dryden, I. L.; Mardia K. V.: *Statistical Shape Analysis*, 2nd ed. West Sussex, John Wiley & Sons, 2016

- 
- [82] Stegmann, M. B.; Gomez, D. D.: A Brief Introduction to Statistical Shape Analysis, Informatics and mathematical modelling, Technical University of Denmark, DTU, 2002
- [83] Goodall, C.: Procrustes Methods in the Statistical Analysis of Shape, *Journal of the Royal Statistical Society B*, 53 (2), 1991, 285–339
- [84] Gower, J. C.: Generalized Procrustes Analysis, *Psychometrika*, 40 (1), 1975, 33–51
- [85] Abdi, H.; Williams, L. J.: Principal component analysis, *Wiley interdisciplinary reviews: computational statistics*, 2 (4), 2010, 433–459
- [86] Abdi, H.: Singular Value Decomposition ( SVD ) and Generalized Singular Value Decomposition ( GSVD ), *Encyclopedia of measurement and statistics*, 2007, 907–912
- [87] Albrecht, T.; Lüthi, M.; Gerig, T.; Vetter, T.: Posterior Shape Models, *Medical Image Analysis*, 17(8), 2013, 959 - 973.
- [88] Schäfer, J.; Strimmer, K.: A shrinkage approach to large-scale covariance matrix estimation and implications for functional genomics, *Statistical Applications in Genetics and Molecular Biology*, , 4, 2005, Article 32
- [89] Bishop, C.: *Pattern Recognition and Machine Learning*, Springer, 2006.
- [90] Blanz, V.; Vetter, T.: Reconstructing the complete 3D Shape of faces from partial information, *Informationstechnik und Technische Informatik*, 44, 2002, 1 - 8
- [91] Davies, R.H.: *Learning Shape: Optimal Models for Analysing Natural Variability*, PhD Thesis, Division of Imaging Science and biomedical Engineering, University of Manchester, 2002
- [92] Styner, M.A.; et al.: Evaluation of 3D Correspondence Methods for Model Building, in: Taylor C., Noble J.A. (eds) *Information Processing in Medical Imaging. IPMI 2003. Lecture Notes in Computer Science*, vol 2732. Springer, Berlin, Heidelberg, 2003
- [93] Gollmer, S. T.; Buzug, T. M.: A method for quantitative evaluation of statistical shape models using morphometry, in: *2010 IEEE International Symposium on Biomedical Imaging: From Nano to Macro*, Rotterdam, 2010, 448-451
- [94] Davies, R.H.; Twining, C. J.; Taylor, C. J.: *Statistical Models of Shapes: Optimisation and Evaluation*, 2008, Springer
- [95] Lamecker, H.; Seebass, M.; Hege, H.-C.; Deuffhard, P.: A 3D statistical shape model of the pelvic bone for segmentation, in: *Proceedings SPIE 5370, Medical Imaging 2004: Image Processing*, 2004
- [96] Davies, R. H.; Twining, C. J.; Cootes, T. F.; Taylor, C. J.: *Building 3-D Statistical Shape Models by Direct Optimization*, *Mathematics, Medicine, Computer Science* Published in *IEEE Transactions on Medical Imaging*, 2010

- [97] Lüthi, M.; Jud, C.; Gerig, T.; Vetter, T.: *Gaussian Process Morphable Models*, Computer Vision and Pattern Recognition, 2016
- [98] Proffit, W.R.; Turvey T.A.: *Dentofacial asymmetry*. In *Surgical orthodontic treatment*; Proffit, W.R., White R.P. Jr, Eds; Mosby Inc: Missouri, United States, 1991, 483–549
- [99] Hwang, H.S.; Hwang, C.H.; Lee, K.H.; Kang, B.C.: *Maxillofacial 3-dimensional image analysis for the diagnosis of facial asymmetry*. *Am J Orthod Dentofacial Orthop*, 130, 2006, 779–785
- [100] Yañez-Vico, R.M.; Iglesias-Linares, A.; Torres-Lagares, D.; Gurierrez-Perez, J.L.; Solano-Reina, E.: *Three-dimensional evaluation of craniofacial asymmetry: an analysis using computed tomography*. *Clin Oral Investig* 2010, 15, 729-736
- [101] Tuncer, B.B.; Atac, M.S.; Yuksel, S.: *A case report comparing 3-D evaluation in the diagnosis and treatment planning of hemimandibular hyperplasia with conventional radiography*. *J. Craniomaxillofac Surg*. 2009, 37, 312-319
- [102] Baek, S.H.; Cho, I.S.; Chang, Y.I.; Piupiu, S.P.; Kim, M.J.: *Skeletodental factors affecting chin point deviation in female patients with class III malocclusion and facial asymmetry: a three-dimensional analysis using computed tomography*. *Oral Surg Oral Med Oral Pathol Oral Radiol Endod* 2007, 104, 628–39
- [103] Kwon, T.G.; Park, H.S.; Ryoo, H.M.; Lee, S.H.: *A comparison of craniofacial morphology in patients with and without facial asymmetry - A three-dimensional analysis with computed tomography*. *International Journal of Oral and Maxillofacial Surgery*, 2006, 5, 43-48
- [104] Willing, R.T.; Roumeliotis, G.; Jenkyn, T.R.; Yazdani, A.: *Development and evaluation of a semi-automatic technique for determining the bilateral symmetry plane of the facial skeleton*. *Medical Engineering and Physics*, 2013, 35, 1843-1849
- [105] Damstra, J.; Fourie, Z.; De Wit, M.; Ren, Y.: *A three-dimensional comparison of a morphometric and conventional cephalometric midsagittal planes for craniofacial asymmetry*. *Clinical Oral Investigations*, 2012, 16, 285-294
- [106] De Momi, E.; Chapuis, J.; Pappas, I.; Ferrigno, G.; Hallermann, W.; Schramm, A.; Caversaccio, M.: *Automatic extraction of the mid-facial plane for cranio-maxillofacial surgery planning*. *International Journal of Oral and Maxillofacial Surgery*, 2006, 35, 636-642
- [107] Zhang, L.; Razdan, A.; Farin, G.; Femiani, J.; Bae, M.; Lockwood, C.: *3D face authentication and recognition based on bilateral symmetry analysis*. *Visual Computer*, 2006, 22, 43-55
- [108] Gupta, A.; Kharbanda, O.P.; Balachandran, R.; Sardana, V.; Kalra, S.; Chaurasia, S.; Sardana, H.K.: *Precision of manual landmark identification between as-received and oriented volume-rendered cone-beam computed tomography images*. *American Journal of Orthodontics and Dentofacial Orthopedics*, 2017, 151, 118-131



- 
- [109] Kim, T.Y.; Baik, J.S.; Park, J.Y.; Chae H.S.; Huh K.H.; Choi, S.C.: Determination of midsagittal plane for evaluation of facial asymmetry using three-dimensional computed tomography. *Imaging Sci Dent* 2011, 41, 79–84
- [110] Green, M.N.; Bloom, J.M.; Kulbersh, R.: A simple and accurate craniofacial midsagittal plane definition. *American Journal of Orthodontics and Dentofacial Orthopedics* 2017, 152, 355-363
- [111] Cavalcanti, M.G.; Vannier, M.W.: Quantitative analysis of spiral computed tomography for craniofacial clinical applications. *Dentomaxillofacial Radiology* 1998, 27, 344-350
- [112] Gupta, A.; Kharbanda, O.P.; Sardana, V.; Balachandran, R.; Sardana, H.K.: A knowledge-based algorithm for automatic detection of cephalometric landmarks on CBCT images. (2015) *International Journal of Computer Assisted Radiology and Surgery*, 2015, 10, 1737-1752
- [113] Yoon, K.W.; Yoon, S.J.; Kang, B.C.; Kim, Y.H.; Kook, M.S.; Lee, J.S.; Palomo, J.M.: Deviation of landmarks in accordance with methods of establishing reference planes in three-dimensional facial CT evaluation. *Imaging Science in Dentistry*, 2014, 44, 207-212
- [114] Pan, G.; Wu, Z.: 3D face recognition from range data. *International Journal of Image and Graphics* 2005, 5, 1–21
- [115] Marquardt, D.: An Algorithm for Least-Squares Estimation of Nonlinear Parameters. *Journal on Applied Mathematics*, 11, 1963, 431–441
- [116] Leclerc, Y.G.: Constructing simple stable descriptions for image partitioning. *International journal of computer vision*, 3, 1989, 73-102
- [117] Kennedy, J.; Eberhart, R.C.: Particle swarm optimization, in: *Proceedings of the IEEE International Conference on Neural Networks (ICNN)*, Perth, Australia, 1995